Bose polarons and rotating gases in an ultracold Bose-Fermi gas mixture of ^{40}K and ^{87}Rb atoms

by

Ming-Guang Hu

B.S. & M.S. Theoretical Physics, Nankai University (China), 2009

A thesis submitted to the

Faculty of the Graduate School of the

University of Colorado in partial fulfillment

of the requirements for the degree of

Doctor of Philosophy

Department of Physics

2015

This thesis entitled:
Bose polarons and rotating gases in an ultracold Bose-Fermi gas mixture of ^{40}K and ^{87}Rb atoms
written by Ming-Guang Hu
has been approved for the Department of Physics

Deborah Jin

Eric Cornell

Date

The final copy of this thesis has been examined by the signatories, and we find that both the content and the form meet acceptable presentation standards of scholarly work in the above mentioned discipline.

Hu, Ming-Guang (Ph.D., Physics)

Bose polarons and rotating gases in an ultracold Bose-Fermi gas mixture of ^{40}K and ^{87}Rb atoms

Thesis directed by Dr. Deborah Jin

An ultracold Bose-Fermi gas mixture of ^{40}K and ^{87}Rb atoms has tunable interspecies interactions and therefore provides a fantastic platform for exploring not only few-body physics such as Feshbach molecule formation and Efimov trimers, but also many-body physics including Bose polarons, quantum Hall physics and so on. In this thesis, I present experimental evidence of Bose polarons in cold atoms obtained using radio-frequency spectroscopy to measure the excitation spectrum of fermionic ^{40}K impurities resonantly interacting with a BEC of ^{87}Rb atoms. These Bose polarons originate from the dressing of an impurity coupled to its environment, which is an important paradigm in quantum many-body physics. I also present initial work that launches an exciting new direction for our experiment, which is exploring rotating quantum gases. Goals for this work include studying both rotating Bose and Fermi superfluids with tunable interactions as well as working toward rapidly rotating quantum gases in the quantum Hall regime. For these goals, a new all-optical trap for rotating gases was designed, implemented, and tested using a ^{87}Rb Bose-Einstein condensate.

Dedication

I lovely dedicate this thesis to my wife Jinhua Li, who supported me each step of the way.

Acknowledgements

Before I came to CU, I was trained to be a theoretical physicist and had rare experience on experimental physics. I want to thank my advisor, Debbie, for offering me such a great opportunity to work in her group on cold atoms experiment. I also want to thank the former graduate students, Ty and Ruth, who were patient to show me how to run our cold atoms machine. It's their efforts that make my life easier. Started by Ty, two interesting science projects, Feshbach molecule association and Efimov three-body physics, were successfully finished by Ruth and me. In the fourth year of my Ph.D study (2013), Debbie and Eric planned to start a new joint project, rapidly rotating ultracold gases. At the same time, I needed to figure out what my Comps III was about. With the help of Debbie, I proposed a new apparatus for rotating gases and simulated its feasibility, which convinced Eric to explore this novel direction in my lab. For me, I am excited that Eric joined our lab and I can have more chances to talk with one of my heros.

Later, Vandy and Dhruv joined our lab. They are talented and easy to get along with. I am impressed by how good Vandy is at finding right places to buy some unusual instruments. For example, he found a good company to buy a broadband microwave amplifier with a reasonable price and nice service. Dhruv gives me an impression that he has many science ideas, some of which may be suitable to be tested by our machine in the future.

Finally, I want to thank the JILA electronics shop and instrument shop which help me a lot. In particular, I want to thank Terry Brown from the electronics shop, who taught me a lot of electronics for stabilizing lasers.

Contents

Chapter

Tables

Table

Figures

Figure

Chapter 1

Introduction

With the development of laser trapping and cooling technologies, neutral atoms can be manipulated in an unprecedent way. Many applications have been achieved so far. One of the most successful directions is to study new phases of matter, which may only exist at ultralow temperatures near absolute zero ($T \sim 10^{-6}$K). Here, the thermal de Broglie wavelength of atoms, $\lambda_{\mathrm{T}} = h/\sqrt{2\pi m k_B T}$, becomes comparable to the interparticle spacing and quantum mechanical effects start to dominate. In this regime, quantum many-body physics can be engineered by tuning the interactions between atoms. This thesis presents experiments that engineer and measure some interesting quantum many-body physics by using an ultracold Bose-Fermi gas mixture of ^{40}K and ^{87}Rb.

1.1 Many-body physics in ultracold atomic gases

Condensed matter systems consist of many particles and many of these cannot be well described by single-body physics without interactions. Beyond few-body models, theoretical calculations and discussions of a many-body system can become extremely difficult. On the other hand, some collective phenomena demonstrated by condensed matter samples, like superconductivity, ferromagnetism, and integer/fractional conductance, are intriguing for a physicist and crucial for advance of technology. Understanding these interacting quantum many-body systems requires considerations of hundreds and thousands of individual particles and particle-particle interactions, which cannot be treated exactly. As a result, new theoretical models are proposed. These theories

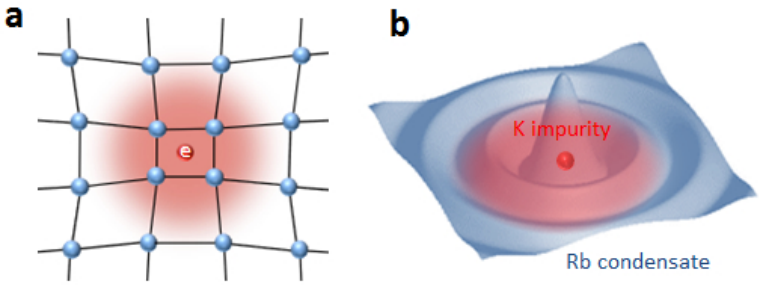

Figure 1.1: A polaron formed by an electron moving in a crystal lattice and its counterpart, a Bose polaron formed by an impurity atom immersed in a BEC.

can not only explain observed collective phenomena but also can predict novel local properties, such as a quasiparticle excitation with fractional statistics, known as an anyon. Furthermore, based on the current understanding of many-body systems, people are proposing novel materials, of which only a few have been realized in a condensed matter lab, while more of them remain unexplored. Ultracold atomic gases with tunable interactions provide a promising platform to engineer these exotic states.

The first many-body physics topic related to my research in this thesis is the Bose polaron. An electron moving in an ionic crystal lattice is dressed by coupling to lattice vibration modes (phonons), which as a result forms a quasiparticle, known as a polaron (see Fig. 1.1a). Such a mechanism is highly nontrivial and has become an important paradigm in quantum many-body physics [1]. Recently, intense theoretical discussions focused on impurities immersed in a Bose-Einstein condensate (BEC) with couplings between impurities and Bogoliubov phonon excitations of BEC [2, 3, 4, 5, 6, 7, 8]. It is suggested that impurities dressed by phonons would form novel quasiparticles, known as Bose polarons (see Fig. 1.1b), even in the strongly interacting regime [9, 10, 11, 12]. However, measurement of Bose polarons in the strongly interacting regime is challenging due to the loss of atoms through three-body recombination and effects of density inhomogeneity in trapped atomic gases. In this thesis I report experimental evidence of Bose polarons by using radio-frequency spectroscopy to measure the excitation spectrum of fermionic ^{40}K impurities resonantly interacting with a BEC of ^{87}Rb atoms. We find that the measured energy of the

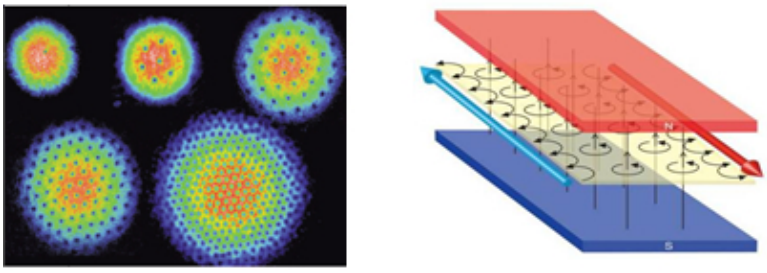

Figure 1.2: Similarity between a rotating BEC and a quantum Hall system. Left: measured density distribution of the gaseous Bose-Einstein condensate under rotation; an exotic vortex lattice forms as the rotation speed increases. (credit: JILA TOP trap.) Right: illustration of moving electrons when they are in quantum Hall states under strong magnetic field. (credit:UTokyo.)

impurites immersed in the BEC matches well with that calculated for Bose polarons for a range of interaction strengths. In particular, we confirm that the polaron state exists even across unitarity in the strongly interacting regime and approaches the weakly bound molecular state. Furthermore, for attractive interactions, we show that Rabi oscillations can be observed when exciting Bose polarons. This work is the first measurement of the Bose polaron in a three-dimensional trapped atom gas, which helps better understanding of the quantum many-body physics of Bose-Fermi mixtures.

The second many-body physics topic related to the research in this thesis is the quantum Hall effect. Quantum Hall states are exotic "topological" states of matter that were originally used to describe states of electrons moving in a two-dimensional plane in a strong magnetic field (see right panel of Fig. 1.2). Understanding these states is important and has led to the proposal of novel materials. A well-known example is the topological insulator, which is a popular research topic in condensed matter field at present [13]. Although the quantum Hall effect has been observed using specialized semiconductors [14], there are very few experimental examples of quantum Hall states. Recently it was proposed to realize quantum Hall states by rapidly rotating an ultracold atomic gas [15]. In this thesis, I will discuss the connection between quantum Hall states and rapidly rotating ultracold gases. Then I will demonstrate a new apparatus that we designed with the goal of producing rapidly rotating ultracold gases into the quantum Hall regime. Technical challenges as well as experimental progress will be shown.

In the past decade, many other examples of using ultracold atomic gases to study many-body physics were demonstrated. Topics include quantum magnetism, Harper Hamiltonian, Fermi polarons, artificial gauge fields, and so on. More interesting experiments are on the way. Ultracold atomic gases have become an indispensable test bed for exploring many-body physics.

1.2 Bose gas and Fermi gas at ultralow temperature

Many review papers and theses have comprehensive introductions on the ultracold Bose gas, the Bose-Einstein condensate and the degenerate Fermi gas. Here I won't repeat these and instead I will just introduce the necessary knowledge for understanding the relevant many-body physics that I will present in this thesis.

Table 1.1: Useful formula for a weakly interacting BEC in 3D at the Thomas-Fermi limit [15]. Here M is the boson mass, n is the atom number density, $g = 4\pi a\hbar^2/M$ is the coupling constant with a being the scattering length and M being the atomic mass of an atom.

Quantities	Formula
Oscillator length (non-interacting BEC size)	$d_0 = \sqrt{\frac{\hbar}{M\omega_0}}$
Healing length	$\xi = \frac{1}{\sqrt{8\pi an}}$
Thomas-Fermi distribution	$n(\mathbf{r}) = n_0\left(1 - \frac{x^2}{R_x^2} - \frac{y^2}{R_y^2} - \frac{z^2}{R_z^2}\right)$
Chemical potential	$\mu = \frac{5^{2/5}}{2}\left(\frac{N_0 a}{d_0}\right)^{2/5}\hbar\omega_0$
Thomas-Fermi radii	$R_{x,y,z} = \sqrt{\frac{2\mu}{M\omega_{x,y,z}^2}}$
Peak BEC density& Number†	$n_0 = \mu/g$, $N_0 = 8\pi n_0 R_0^3/15$
Column density	$\bar{n}(\mathbf{r}) = \bar{n}_0\left(1 - \frac{x^2}{R_x^2} - \frac{y^2}{R_y^2}\right)^{3/2}$
Peak BEC column density & Number	$\bar{n}_0 = (4/3)R_z n_0$, $N_0 = (2\pi/5)\bar{n}_0 R_x R_y$
Averaged BEC density	$\langle n\rangle = (4/7)n_0$
RMS width & TF radius	$\sigma_{\mathrm{RMS}} = 0.437 R_{\mathrm{TF}}$

†averaged Thomas-Fermi radius $R_0 = (R_x R_y R_z)^{1/3}$.

When a thermal ^{87}Rb atomic gas in a harmonic trap is cooled down below a critical temperature, $T_c = \hbar\omega_0[N/\zeta(3)]^{1/3}/k_B$, a phase transition occurs and a Bose-Einstein condensate is formed with a BEC fraction given by, $N_0/N = 1-(T/T_c)^3$. Here the averaged trapping frequency is defined by $\omega_0 = (\omega_x\omega_y\omega_z)^{1/3}$, the Riemann zeta function $\zeta(3) = 1.2$, k_B is the Boltzmann constant, N_0

is the number of atoms in the BEC, and N is the total atom number. When the BEC fraction is big enough, the interaction between BEC atoms, characterized by the scattering length a, needs to be considered. For our case of a weakly interacting BEC ($\xi \gg 1/n^{1/3}$) , the static BEC can be described by the time-independent Gross-Pitaevskii (GP) equation [15]

$$\left(\underbrace{-\frac{\hbar^2\nabla^2}{2M}}_{\text{kinetic}} + \underbrace{V_{\text{tr}}(\mathbf{r})}_{\text{trap}} + \underbrace{g|\Psi(\mathbf{r})|^2}_{\text{interaction}} \right) \Psi(\mathbf{r}) = \mu\Psi(\mathbf{r}), \tag{1.1}$$

where M is the mass of the atom, μ is the chemical potential, $\Psi(\mathbf{r})$ is the macroscopic condensate wave function (or "order parameter"), and g is the coupling constant $g = 4\pi a\hbar^2/M$. Here $a = 100a_0$ is the scattering length between two Rb atoms with a_0 being the Bohr radius [16]. The BEC density is given by $n(\mathbf{r}) = |\Psi(\mathbf{r})|^2$, and sometimes it is useful to write $\Psi(\mathbf{r}) = \sqrt{n(\mathbf{r})}e^{i\phi(\mathbf{r})}$ with a phase term $\phi(\mathbf{r})$. For this thesis, we are working in the Thomas-Fermi regime ($N_0a/d_0 \gg 1$ or $\mu \approx n_0 g \gg \hbar\omega_{x,y,z}$) and thus the kinetic energy term in Eq. (1.1) can be ignored. As a result, the BEC density simply follows an inverse parabola distribution (see Table 1.1). A more detailed introduction can be found in Ref. [15].

Table 1.2: Useful formula for a weakly interacting BEC in quasi 2D. Here g_2 is the reduced coupling constant in 2D.

Quantities	Formula
Thomas-Fermi distribution	$n(\mathbf{r}) = n_0\left(1 - \frac{x^2}{R_x^2} - \frac{y^2}{R_y^2}\right)e^{-z^2/l_z^2}$
Thomas-Fermi radii	$R_{x,y} = \sqrt{\frac{2\mu'_{2D}}{M\omega_{x,y}^2}}$
Chemical potential	$\mu_{2D} = \hbar\omega_z/2 + \mu'_{2D}$, $\mu'_{2D} = \frac{2N_0 g_2}{\pi R_x R_y}$
Column density&Number	$\bar{n}(\mathbf{r}) = \bar{n}_0\left(1 - \frac{x^2}{R_x^2} - \frac{y^2}{R_y^2}\right)$, $N_0 = \frac{\pi}{2}R_x R_y \bar{n}_0$,

For a rapidly rotating gas, a quasi-2D BEC is relevant in the regime of small chemical potential, where $\mu < \hbar\omega_z$. Here, the BEC stays at the lowest energy level along z while it still occupies many energy levels in the x and y directions. The wavefunction can be written as $\Psi(\mathbf{r}) = \frac{1}{\pi^{1/4}\sqrt{l_z}}e^{-z^2/2l_z^2}\Psi_2(x,y)$ with the oscillator length $l_z = \sqrt{\hbar/M\omega_z}$ and $\Psi_2(x,y)$ being the

2D condensate wavefunction. The critical temperature is $T_c^{2D} = \hbar\sqrt{\omega_x\omega_y}[N/\zeta(2)]^{1/2}/k_B$ with the Riemann zeta function $\zeta(2) = 1.64$ [17]. The GP equation is modified as [Rychtarik's thesis [18]]

$$\left(-\frac{\hbar^2\nabla_\perp^2}{2M} + V_{\rm tr}(\mathbf{r}_\perp) + g_2|\Psi_2(\mathbf{r}_\perp)|^2\right)\Psi_2(\mathbf{r}_\perp) = \mu'_{2D}\Psi_2(\mathbf{r}_\perp), \tag{1.2}$$

where the 2D spatial coordinate $\mathbf{r}_\perp = \{x, y\}$, the reduced coupling constant $g_2 = \sqrt{8\pi}\hbar^2 a/Ml_z$ and the chemical potential $\mu_{2D} = \mu'_{2D} + \hbar\omega_z/2$. Useful formula are listed in Table 1.2.

Table 1.3: Useful formula for a degenerate Fermi gas in 3D.

Quantities	Formula
Fermi energy & Fermi temperature	$E_F = k_B T_F = (6N)^{1/3}\hbar\omega_0$
Fermi-Dirac distribution*	$f(\epsilon) = \frac{1}{e^{\epsilon/k_B T}/\zeta+1}$, fugacity $\zeta = e^{\mu/k_B T}$
Number	$N = -(k_B T/\hbar\omega_0)^3 Li_3(-\zeta)$
Relationship of fugacity and T	$Li_3(-\zeta) = -\frac{1}{6(T/T_F)^3}$
Chemical potental	$\mu = k_B T \ln\zeta$

*$Li_n(x)$ is Poly-Logarithmic function of order n defined as $Li_n(x) = \sum_{k=1}^{\infty} x^k/k^n$.

For the Fermi gas of ^{40}K atoms in my system, most of the experiments in this thesis use a relatively "hot" gas at $T/T_F \sim 0.5$. However, for completeness, I will list some frequently used quantities that are important for discussing a Fermi gas. In general, the density of states in a d-dimensional harmonic potential is

$$\rho(\epsilon) = \frac{\epsilon^{d-1}}{(d-1)!\prod_{i=1}^{d}\hbar\omega_i}, \tag{1.3}$$

where ω_i is the trapping frequency along i-th direction. The density distribution of a Fermi gas trapped in a 3D harmonic trapping potential follows

$$n(\mathbf{r}) = -\frac{(k_B MT)^{3/2}}{(2\pi)^{3/2}\hbar^3} Li_{3/2}\left(-\zeta e^{-\frac{M}{2k_B T}(\omega_x^2 x^2+\omega_y^2 y^2+\omega_z^2 z^2)}\right), \tag{1.4}$$

which is reduced to the classic Maxwell-Boltzmann distribution at $T/T_F \gg 0.1$. Some basic quantities have been listed in Table 1.3 and more detailed discussions can be found in DeMarco's thesis (P.233) [19].

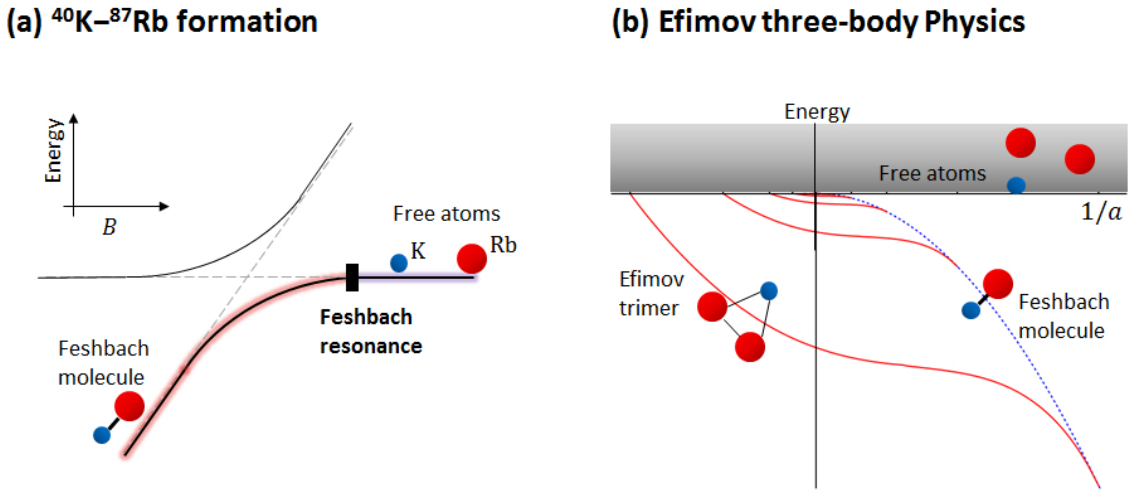

Figure 1.3: Few-body physics explored by tuning a Feshbach resonance. (a) Association of KRb Feshbach molecules by ramping the magnetic field across a Feshbach resonance [20]. (b) Tests of universal three-body physics in an ultracold Bose–Fermi mixture [21]. I was involved in previous work on these two topics done in my lab; detailed discussions are included in Cumby's thesis [22] and Bloom's thesis [23].

1.3 Feshbach resonance for tuning interactions

One of our powerful tools in ultracold gases is a Feshbach resonance that can be used to tune the atomic interactions [24]. The capability of controlling interactions is very important to study not only few-body physics but also many-body physics [25]. Examples of few-body physics include two-body Feshbach molecule association [Cumby's thesis [22]], three-body Efimov resonances [Bloom's thesis [23]], and so on (see Fig. 1.3). Examples of many-body physics include BCS-BEC crossover of a degenerate Fermi gas [Regal's thesis [26]], impurity-bath coupling [27, 28, 29, 30, 31], and so on. Simply speaking, when tuning an applied magnetic field B close to a specific value B_0, the scattering rate between particles is enhanced. For the simplest situation of isotropic s-wave scattering, interactions can be well described by a parameter known as the scattering length a. The dependence of the scattering length a on B is given by [24]

$$a(B) = a_{\mathrm{bg}}\left(1 - \frac{\Delta}{B - B_0}\right), \tag{1.5}$$

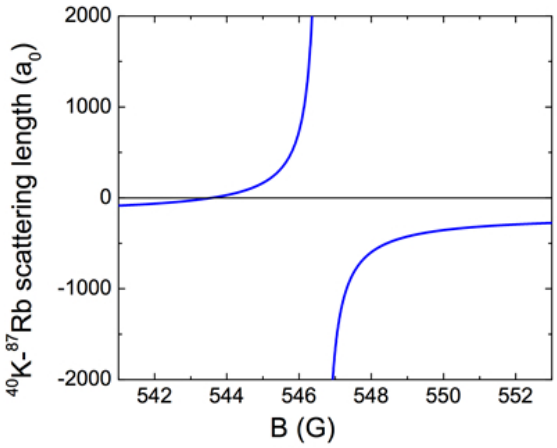

Figure 1.4: Scattering length a_{KRb} versus magnetic field B around the interspecies Feshbach resonance between ^{40}K and ^{87}Rb atoms. The interaction is short-range. It is attractive for $a_{\mathrm{KRb}} < 0$ and repulsive for $a_{\mathrm{KRb}} > 0$.

with a_{bg} being the background scattering length and Δ the resonance width. The coupling constant g is proportional to a.

For ^{87}Rb, there are no broad Feshbach resonances [16] and therefore we can simply treat it to be a gas with constant background scattering length $a_{\mathrm{BB}} = 100a_0$. Here a_0 is the Bohr radius. For describing a ^{87}Rb BEC, a weak background interaction is included in the theories leading to the Bogoliubov phonon excitations, which is relevant to the Bose polarons discussed in Ch. 3.

For ^{40}K, we work in the polarized limit in which all atoms are in a single hyperfine state $|F, m_F\rangle = |9/2, -9/2\rangle$, where F corresponds to the total atomic angular momentum and m_F is its projection. Due to the quantum statistics of fermions, fermion-fermion interactions are strongly suppressed in the ultracold gas. In my following discussions, fermion-fermion interactions are ignored.

For a mixture of ^{40}K atoms and ^{87}Rb atoms, an s-wave Feshbach resonance is used to control the interactions between bosonic ^{87}Rb atoms in the $|1, 1\rangle$ state and fermionic ^{40}K atoms in the $|9/2, -9/2\rangle$ state. The boson-fermion scattering length a_{KRb} as a function of magnetic field B (Fig. 1.4) is given by a_{KRb}=$a_{\mathrm{bg}}[1 - \Delta/(B - B_0)]$, a_{bg}=$-187\,a_0$, B_0=546.62 G, Δ=-3.04 G [32]. We use this Feshbach resonance to tune interactions between ^{40}K atoms and ^{87}Rb atoms to study

interesting many-body physics.

1.4 Overview

This thesis covers two main research topics that I was leading in the past two years. The first one is a study of Bose polarons as described in Sec. 1.1. The main tools we used are the interspecies Feshbach resonance and RF spectroscopy. This work helps elucidate the behavior of impurities in a BEC, which is a paradigmatic problem in many-body physics. The second topic is to design and construct a new apparatus for creating rotating ultracold atomic gases in the quantum Hall regime. Technical challenges are explored and experimental progress is discussed. Besides studying quantum Hall physics, such a versatile apparatus is also promising to explore other interesting physics such as the effect of dimensionality on the BEC/BKT transition, vortices in a strongly interacting BEC, etc..

The remainder of the thesis is organized as follows.

Chapter 2 presents improvements I made to the frequency stabilization of the Rb and K laser systems. A stable laser system is crucial for laser cooling and trapping atoms. It is also important to have the ability to jump the laser frequency for atom detection. By using new electronics technology, I set up a flexible beatnote locking that allows the frequency of a laser beam to be shifted easily over a GHz range.

Chapter 3 is dedicated to the Bose polaron study. I include a general introduction to the Bose polaron problem. Then I show our experimental results for the polaron energy spectrum, which is compared to theoretical models. To probe the particle nature of polarons, we also investigate Rabi oscillations when driving these states.

Chapter 4 discusses quantum Hall physics and its connection with rapidly rotating ultracold gases. I introduce quantum Hall states and why they are bizarre. Their connection with rotating gases as well as experimental challenges are discussed.

Chapter 5 introduces a new apparatus for rapidly rotating ultracold gases. A “painted” (or time-averaged) optical trapping potential is a critical part of our approach. The time-averaging or

"painting" can give us a near-perfect round trap geometry and can also reduce roughness of the trapping potential, which is critical for rotating gases very rapidly.

Chapter 6 summarize the major results of this thesis and concludes with a discussion of future experiments.

Chapter 2

Improved laser systems for cooling and trapping Rb and K atoms

A stable laser system is crucial for laser cooling and trapping atoms. In this chapter, I present the improvement I made to stabilize our rubidium and potassium laser systems. In particular, I set up a modulation transfer spectroscopy, an excellent way of stabilizing lasers developed recently, for the potassium laser system [33]. This spectroscopy is compared against the frequency-modulation (FM) spectroscopy [34, 35]. In addition, with new electronics technology, I set up a flexible phase lock of a slave laser (trap laser) to a master laser (repump laser), which allows us to shift the frequency of the slave laser over a GHz range. The spectroscopic properties of rubidium and potassium can be found in [36] and [37], respectively.

2.1 Rubidium laser stabilization (FM spectroscopy)

To get a ^{87}Rb magneto-optical trap (MOT), two lasers, the repump laser and the trap laser, are needed. The repump laser is for hyperfine pumping using the ($F = 1 \rightarrow F' = 2$) transition. Here F (F') denotes the total atomic angular momentum of the ground (excited) states. In our experiment, the repump laser is locked to the ^{87}Rb $F = 1 \rightarrow F' = 1, 2$ crossover using FM spectroscopy (see the next paragraph). Then, the frequency of the repump laser is shifted up by 78 MHz using a single-passed acouto-optical modulator (AO) (+1 order). The trap laser is for cooling and trapping using the cycling transition ($F = 2 \rightarrow F' = 3$). Since the frequency of the ^{87}Rb ($F = 2 \rightarrow F' = 3$) transition is less than that of the ^{87}Rb ($F = 1 \rightarrow F' = 1, 2$ crossover[1])

[1] The crossover frequency is equal to the average of two involved atomic transition frequencies. For example, $f_{F=1\rightarrow F'=1,2 \text{ crossover}} = (f_{F=1\rightarrow F'=1} + f_{F=1\rightarrow F'=2})/2$.

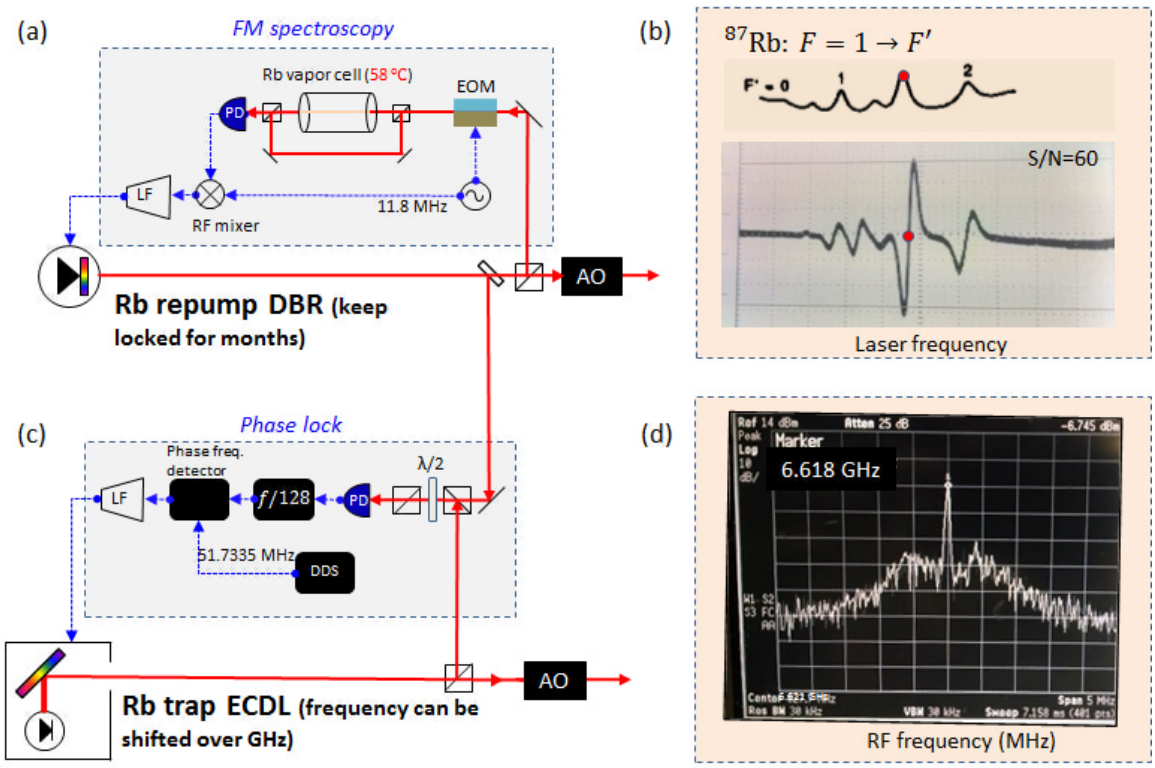

Figure 2.1: An improved rubidium laser system. (a) The FM spectroscopy setup for the repump laser. (EOM denotes an electro-optical modulator; PD is a photodetector; LF is a loop filter; AO is an acousto-optical modulator; DBR is a distributed Bragg reflector laser.) A single-passed AO is used to shift the laser frequency up by 78 MHz. (b) The error signal for locking the repump laser. The upper panel shows the absorption spectroscopy (adapted from [38]) and the lower panel is the error signal obtained using FM spectroscopy [34, 35]. The red dot indicates the reference point, where we lock our repump laser's frequency. (c) The phase-lock setup for the trap laser. DDS denotes a direct digital synthesizer (Analog devices: AD9959-eval). "$f/128$" is a frequency divider (Hittite microwave: HMC363). The phase frequency detector has the model number (Hittite microwave: HMC440). (d) The RF spectrum of the beat between the trap laser and the repump laser when the phase lock is on. The beat signal is measured by a RF spectrum analyzer. The x-axis has the center at 6.618 GHz and the span of 20 MHz. The unit of the y axis is dBm.

transition by 6.4896 GHz [36], we lock our trap laser to the repump laser using a phase-lock loop with a beat frequency of $f_b = 6.622$ GHz. Then, the frequency of the trap laser is shifted up by 133.5 MHz using a double-passed AO (+1 order).

Fig. 2.1(a) shows the schematic of FM spectroscopy setup for the repump laser. There are two overlapped counter-propagating beams passing through a Rb vapor cell. The beam probed by a photodetector (PD) is called the probe beam and the other one is called the pump beam.

When we scan the laser's frequency by ramping the laser current, the measured power of the probe beam gives a Doppler-free absorption spectroscopy as shown in the upper panel of Fig. 2.1(b). The red dot indicates the lock point, where we lock our repump laser. The lower panel of Fig. 2.1(b) shows the error signal that is input into a loop filter (LF) for stabilizing the repump laser frequency. The error signal is the derivative of the absorption signal and is obtained using FM spectroscopy [34, 35], which requires the laser beam's phase to be modulated. An electro-optical modulator (EOM) shown in Fig. 2.1(a) is used to modulate the phase of the repump laser beam with the modulation frequency, $f_m = 11.8$ MHz. Although we modulate both the probe and pump beams, only the probe beam needs to be modulated.

The error signal is crucial for stabilizing the laser's frequency. We care about its signal-to-noise ratio (S/N) that is defined here as the ratio of the peak-to-peak amplitude over the background noise amplitude. The error signal of ($F = 1 \rightarrow F'$) is about ten times weaker than that of ($F = 2 \rightarrow F'$). To increase the S/N of the error signal at the $F = 1 \rightarrow F' = 1, 2$ crossover, the vapor cell is heated to above the melting point of rubidium (38.9 °C) to increase the vapor pressure. The optimal temperature is determined by looking at the S/N and is set to be 58 °C in our experiment. Additionally, it is important to keep the light intensity of the probe beam less than the saturation intensity ($I_{\text{sat}} = 2.5$ mW/cm^2 [36]). For our case, the $1/e^2$ width of the probe beam is about $w = 1$ mm and the power is $P = 20$ μW, which gives the peak intensity of the probe beam, $I = \frac{2P}{\pi w^2} \approx 1.3$ mW/cm^2.

Fig. 2.1(c) shows a diagram of the phase-lock setup for the trap laser. A 6.622 GHz beat signal is detected by a fast PD (EOT Inc.: ET-4000) with a bandwidth of 12.5 GHz. Because the phase frequency detector (PFD) (Hittite microwave: HMC440) only has a bandwidth of 10 to 1300 MHz, we divide the beat frequency by a factor of 128 (a factor of 8 using a frequency divider (Hittite microwave: HMC363) and another factor of 16 by the PFD). By comparing against a reference RF signal of 51.7335 MHz, the PFD converts the divided beat signal into an error signal for the laser stabilization. The reference RF signal is provided by a direct digital synthesizer (DDS), which is controlled by a computer. We tune the trap laser's frequency by changing the

reference RF frequency. In this way, we can shift the trap laser's frequency over a GHz range, which is important for the phase contrast imaging discussed in Sec. 5.2.1. Fig. 2.1(d) shows the RF spectrum of the beat between the trap laser and the repump laser when the phase-lock loop is on. The delta function of the spectrum indicates a phase lock of the trap laser to the repump laser.

In the above discussion, I have focused on the spectroscopy of the Rb laser system that I changed for improving laser stabilization. The rest of the Rb laser system can be found in Chap. 4 of the previous thesis [23].

2.2 Potassium laser stabilization (modulation transfer spectroscopy)

For a ^{40}K MOT, both the repump and trap lasers are important for cooling and trapping. The repump laser is red-detuned from the $F = 7/2 \rightarrow F' = 9/2$ transition and the trap laser is red-detuned from the cycling transition, $F = 9/2 \rightarrow F' = 11/2$. Because of the small natural abundance of ^{40}K (0.0117%), the spectroscopy signal of ^{40}K from a vapor cell is too weak to use for laser stabilization. Instead we lock our repump laser to the ^{39}K $F = 2 \rightarrow F' = 3$ transition using modulation transfer spectroscopy [33] (see the next paragraph). The isotope ^{39}K has a large natural abundance of 93.3%. The frequency of the ^{40}K $F = 7/2 \rightarrow F' = 9/2$ transition is less than that of the ^{39}K $F = 2 \rightarrow F' = 3$ transition by only 431.9 MHz [37], which can be easily reached using a double-passed AO. In our experiment (see Fig. 2.2(a)), a double-passed AO (+1 order) is used to shift the frequency of the repump laser up by 424 MHz before doing the modulation transfer spectroscopy. For the trap laser, the frequency of the ^{40}K $F = 9/2 \rightarrow F' = 11/2$ transition is larger than that of the ^{39}K $F = 2 \rightarrow F' = 3$ transition by 809.8 MHz [37] and we lock our trap laser to our repump laser through a phase lock with the beat frequency 784.8 MHz.

Fig. 2.2(a) shows the schematic of the modulation transfer spectroscopy setup for the repump laser. Different from FM spectroscopy, the probe beam in the modulation transfer spectroscopy is not modulated, while the pump beam is frequency modulated by an EOM. However, to produce the error signal, the probe beam needs containing modulated sidebands [39, 33]. It turns out that the probe beam picks up the modulated sidebands from the collinear pump beam through a

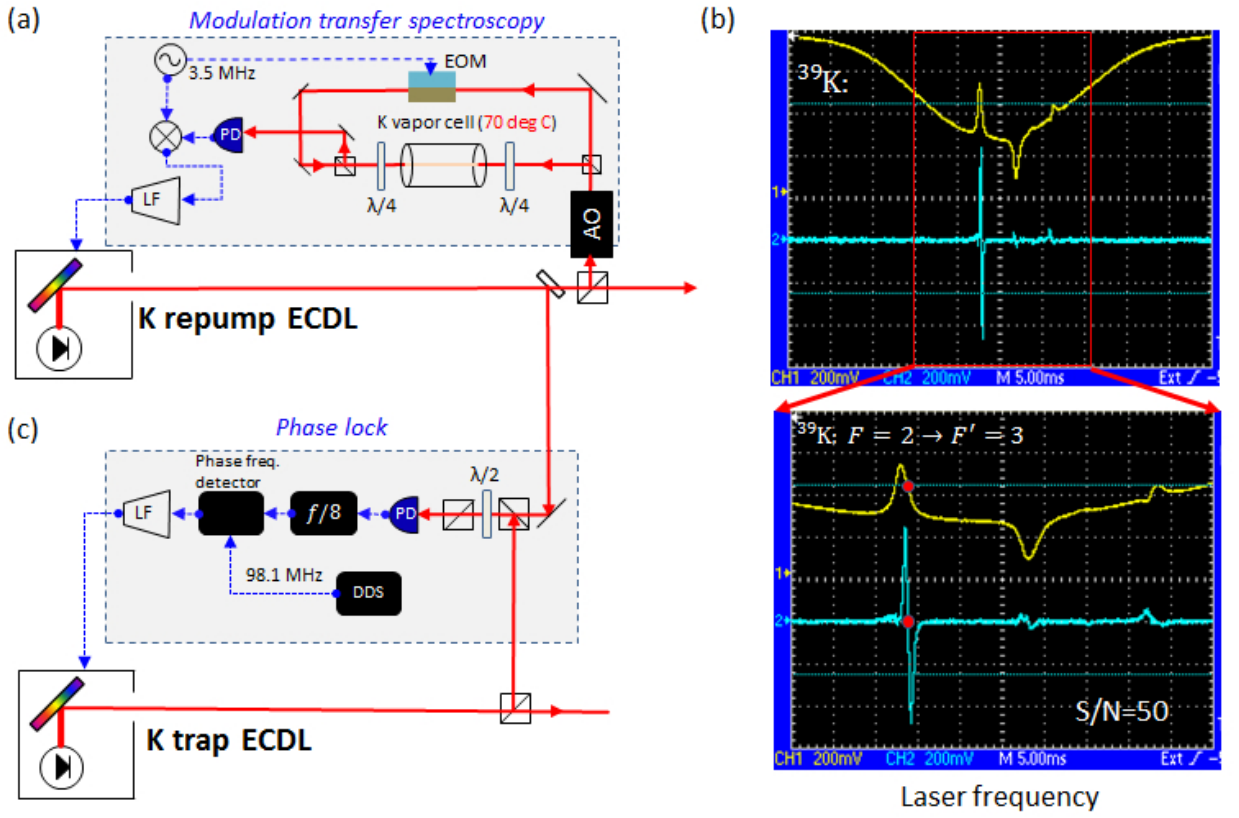

Figure 2.2: An improved potassium laser system. (a) The modulation transfer spectroscopy setup for the repump laser. A double-passed AO is used to shift the laser frequency up by 424 MHz. (b) The error signal for locking the repump laser. The yellow line shows the absorption spectroscopy and the cyan line is the error signal obtained using the modulation transfer spectroscopy [33]. The red dot indicates the reference point, where we lock our repump laser. (c) The phase-lock setup for the trap laser. The beat frequency is 784.8 MHz.

nonlinear four-wave mixing mechanism [40, 41], which is a modulation transfer process. Due to the nonlinear nature of the modulation transfer process, there are three main advantages using the modulation transfer spectroscopy [39, 33]. First, the error signal has a flat zero baseline, since the modulation transfer process only takes place at sub-Doppler resonances. Second, the zero-crossings of the error signals correspond accurately to the atomic transitions [39]. Third, the error signal for a cycling transition is largest, since the modulation transfer is strongest for cycling transitions, which allows the four-wave mixing to occur many times. In particular, as shown in [33], the error signal corresponding to a cycling transition can be further enhanced by using σ^+-σ^+ polarizations

(i.e. right-hand circular probe and left-hand circular pump). This third feature is especially useful when the spectrum contains several closely spaced transitions such as the spectrum of ^{39}K.

Fig. 2.2(b) shows the error signal (the cyan line) obtained using the modulation transfer spectroscopy as well as the Doppler-free absorption spectroscopy (the yellow line). From the absorption spectroscopy, we see three dominant features. From the left to right, the first one is a feature containing three closely spaced ^{39}K ($F = 2 \rightarrow F' = 1, 2, 3$) transitions, the second one is a feature containing two ^{39}K ground-state crossovers, and the third one is a feature containing three ^{39}K ($F = 1 \rightarrow F' = 0, 1, 2$) transitions and two ^{41}K crossovers [33, 42]. The error signal is crucial for stabilizing the laser's frequency. To enhance the error signal at the cycling transition ($F = 2 \rightarrow F' = 3$), I put two quarter-wave plates at two sides of the vapor cell to achieve σ^+-σ^+ polarizations for the probe and the pump beams shown in Fig. 2.2(a). As shown in Fig. 2.2(b), the resulting error signal at the cycling transition ($F = 2 \rightarrow F' = 3$) is particularly large, while the other non-cycling features are completely suppressed.

Additionally, to increase the S/N of the error signal, the K vapor cell is heated to above the melting point of potassium (63 °C) to increase the vapor pressure. The best value of the temperature is determined by looking at the S/N and is set to be 70 °C. The light intensity of the probe beam is kept less than the saturation intensity ($I_{\text{sat}} = 1.75$ mW/cm^2). For our case, the $1/e^2$ width of the probe beam is about 1.5 mm and the power is 60 μW, which gives the intensity of the probe beam $I = \frac{2P}{\pi w^2} \approx 1.7$ mW/cm^2.

Fig. 2.2(c) shows the diagram of the phase-lock setup for the trap laser. A 784.8 MHz beat signal is detected by a fast PD (EOT Inc.: ET-3000A) with a bandwidth of 30 kHz to 1.5 GHz. The rest of the electronics are similar to the Rb phase-lock setup and can be understood straightforwardly.

For comparison, I put the FM spectroscopy signal and the modulation transfer spectroscopy signal (without the two quarter-wave plates) together in Fig. 2.3. The FM spectroscopy is obtained by moving the EOM so that it modulates both the probe and the pump beams (similar to the setup shown in Fig. 2.1(a)). Generally, we set the frequency corresponding to the absorption peak as

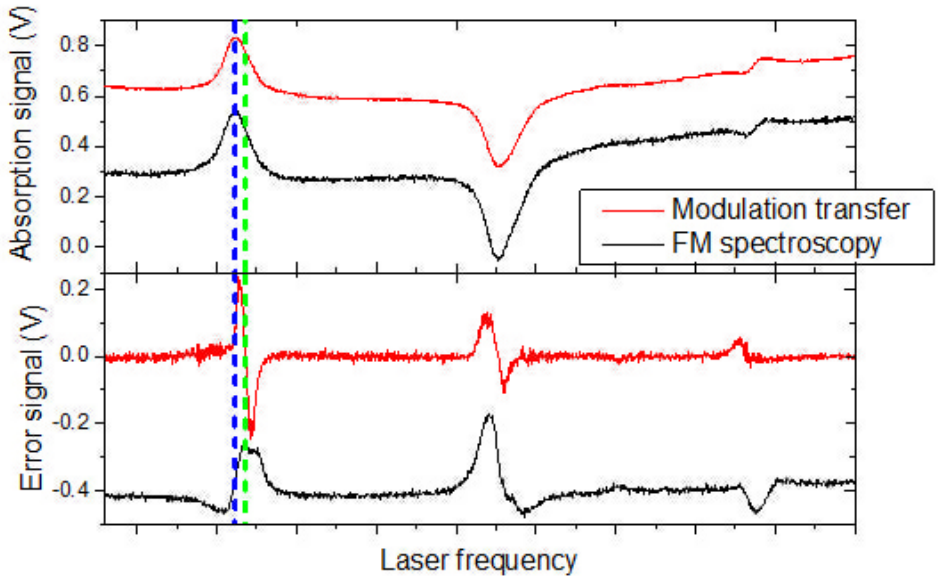

Figure 2.3: Comparison between the modulation transfer spectroscopy and FM spectroscopy for the potassium laser system. The blue dashed line corresponds the absorption peak, where we used to lock our K repump laser. The green dashed line marks the zero crossing of the error signal of the modulation transfer spectroscopy, where we lock our repump laser now. The green dashed line also indicates the location of the ($F = 2 \rightarrow F' = 3$) transition. The frequency difference between the blue line and the green line is 11 MHz.

a lock point for FM spectroscopy (blue dashed line) and set the frequency at the zero crossing of the error signal as a lock point for the modulation transfer spectroscopy (green dashed line). These two lock points are different by 11 MHz. From Fig. 2.3, we can see the three advantages of the modulation transfer spectroscopy I mentioned above: (1) flat zero baseline; (2) accurate correspondence between zero crossing and the atomic transition; (3) dominant error signal at cycling transitions. In addition, the error signal of the modulation transfer spectroscopy shows an anti-symmetric shape around the zero crossing, which is good for laser stabilization. It also shows a narrower capture range (frequency range covered by the linear slope of the error signal) than FM spectroscopy has.

In the above discussion, I have focused on the spectroscopy of the K laser system that I changed for improving laser stabilization. The rest of the K laser system can be found in Chap. 4 of the previous thesis [23].

Chapter 3

Bose polarons in the strongly interacting regime

Ultracold atomic gases provide a fantastic platform for exploring many-body physics with tunable particle-particle interactions. In this chapter, I present an experimental study of the Bose polaron, which is a quasiparticle created by a quantum many-body effect. We used RF spectroscopy to measure the energy shift of the polaron state at different interaction strengths. We find that our results match recent theoretical calculations very well. This work is the first measurement of the Bose polaron in a three-dimensional trapped atom gas and provides strong evidence of the polaronic dressing due to quantum many-body physics.

3.1 Bose polaron theory

An electron moving in an ionic crystal lattice is dressed by coupling to lattice vibration modes (phonons) and, as a result, forms a quasiparticle known as a polaron (see Fig. 1.1(a)). Such a mechanism is highly nontrivial and has become an important paradigm in quantum many-body physics [1]. Historically, such a mechanism was originally pointed out by Landau and Pekar [43, 44]. Then Fröhlich proposed an effective Hamiltonian to describe the polaron problem [45, 1]:

$$H_{\text{Fröhlich}} = \sum_{\mathbf{p},\sigma} \varepsilon_{\mathbf{p}} C^{\dagger}_{\mathbf{p},\sigma} C_{\mathbf{p},\sigma} + \omega_0 \sum_{\mathbf{q}} a^{\dagger}_{\mathbf{q}} a_{\mathbf{q}} + \sum_{\mathbf{q},\mathbf{p},\sigma} \mathcal{V}(\mathbf{q}) C^{\dagger}_{\mathbf{p}+\mathbf{q},\sigma} C_{\mathbf{p},\sigma} \left(a_{\mathbf{q}} + a^{\dagger}_{\text{-}\mathbf{q}} \right). \tag{3.1}$$

In the first term, $C_{\mathbf{p},\sigma}$ (or $C^{\dagger}_{\mathbf{p},\sigma}$) is the annihilation (or creation) operator of an electron with a momentum $\mathbf{p}$, spin σ, and the energy dispersion $\varepsilon_{\mathbf{p}} = \mathbf{p}^2/2m_e$. In the second term, $a_{\mathbf{q}}$ (or $a^{\dagger}_{\mathbf{q}}$) is the annihilation (or creation) operator of a phonon with a momentum $\mathbf{q}$ and the energy

ω_0. Here phonons are the vibration modes of the crystal lattice. The third term describes the coupling between the electrons and the phonons with the coupling strength $\mathcal{V}(\mathbf{q})$. The above Fröhlich Hamiltonian has become a standard model for describing the original polaron problem and a polaron that can be described by Eq. (3.1) is called a Fröhlich polaron. A large amount of theoretical work has been done to solve the Fröhlich Hamiltonian and references can be found in [1]. The most accurate solution came from Feynman through a variational method based on path integrals [46], although his theory is very lengthy [1].

Recently, intense theoretical discussions focused on impurities immersed in a Bose-Einstein condensate (BEC) with couplings between the impurities and Bogoliubov phonon excitations of BEC [2, 3, 4, 5, 6, 7, 8]. It was suggested that impurities dressed by phonons would form novel quasiparticles, known as Bose polarons, even in the strongly interacting regime [9, 10, 11, 12]. To see this, let's consider a system of fermionic impurities immersed in a Bose-Einstein condensate. The impurity-boson coupling can be tuned through a magnetic-field Feshbach resonance, which was introduced in Sec. 1.3. The low-energy effective Hamiltonian [9, 10] is

$$H = \sum_{\mathbf{p}} \epsilon_f(\mathbf{p}) f^\dagger_{1,\mathbf{p}} f_{1,\mathbf{p}} + \sum_{\mathbf{q}} \epsilon_b(\mathbf{q}) b^\dagger_{\mathbf{q}} b_{\mathbf{q}} + \frac{g_{bf}}{V} \sum_{\mathbf{k},\mathbf{k}',\mathbf{q}} b^\dagger_{\mathbf{k}'} f^\dagger_{1,\mathbf{q}-\mathbf{k}'} f_{1,\mathbf{q}-\mathbf{k}} b_{\mathbf{k}}, \tag{3.2}$$

where $\epsilon_{b,f}(\mathbf{k}) = k^2/2m_{b,f}$ are the kinetic energy terms for the majority bosons and the impurity fermions respectively. Here $m_{b,f}$ denote the atomic mass of a boson and fermion, respectively. In the first term, $f_{\sigma,\mathbf{p}}$ (or $f^\dagger_{\sigma,\mathbf{p}}$) is the annihilation (or creation) operator of an impurity fermion in the hyperfine state σ with a momentum $\mathbf{p}$. In the second term, $b_{\mathbf{q}}$ (or $b^\dagger_{\mathbf{q}}$) is the annihilation (or creation) operator of a majority boson with a momentum $\mathbf{q}$. The coupling constant g_{bf} is determined by the scattering length a_{bf} between bosons and fermions. For the zero-range model, the coupling term has an ultraviolet divergence, which is regularized by $\frac{1}{g_{bf}} = \frac{\mu_{bf}}{2\pi a_{bf}\hbar^2} - \frac{1}{V}\sum_{\mathbf{k}} \frac{2\mu_{bf}}{k^2}$. Here the reduced mass is $\mu_{bf} = m_b m_f/(m_b + m_f)$ and V is the volume. The mean-field approximation consists of taking the coupling constant as $g^{MF}_{bf} = 2\pi a_{bf}\hbar^2/\mu_{bf}$, which can be either attractive (negative) or repulsive (positive) depending on the sign of the scattering length.

For a weak repulsion ($n_0 a^3_{bb} \ll 1/6\pi^2$) between bosons characterized by a boson-boson scat-

tering length a_{bb}, the ground state of the BEC can be well described by Bogoliubov theory. Here n_0 is the BEC density. The elementary excitations in the condensate are the collective Bogoliubov modes, which have a dispersion of $\gamma_b(k) = \sqrt{\epsilon_b(\mathbf{k})(\epsilon_b(\mathbf{k}) + 2g_{bb}n_0)}$. Here the mean-field coupling constant given by $g_{bb} = 4\pi a_{bb}\hbar^2/m_b$ and n_0 is the BEC density. The Bogoliubov transformation is $b_{\mathbf{k}} = u_{\mathbf{k}}\alpha_{\mathbf{k}} - v_{\mathbf{k}}\alpha^\dagger_{-\mathbf{k}}$ with real and positive factors $u^2_{\mathbf{k}} = [1 + (\epsilon_b(\mathbf{k}) + g_{bb}n_0)/\gamma_b(\mathbf{k})]/2$ and $v^2_{\mathbf{k}} = [-1 + (\epsilon_b(\mathbf{k}) + g_{bb}n_0)/\gamma_b(\mathbf{k})]/2$ [10]. Using the Bogoliubov transformation, the Hamiltonian given in Eq. (3.2) becomes [10]:

$$
\begin{aligned}
H &= H_0 + H_I, \qquad (3.3)\\
H_0 &= E_g + \sum_{\mathbf{p}} \epsilon_f(\mathbf{p}) f^\dagger_{1,\mathbf{p}} f_{1,\mathbf{p}} + \sum_{\mathbf{q}} \gamma_b(\mathbf{q}) \alpha^\dagger_{\mathbf{q}} \alpha_{\mathbf{q}},\\
H_I &= \frac{g_{bf}}{V}\left(N_0 \sum_{\mathbf{k}} f^\dagger_{1,\mathbf{k}} f_{1,\mathbf{k}} + \sqrt{N_0} \sum_{\mathbf{k},\mathbf{p}} \mathcal{R}(\mathbf{p}) f^\dagger_{1,\mathbf{k}+\mathbf{p}} f_{1,\mathbf{k}} (\alpha_{\mathbf{p}} + \alpha^\dagger_{-\mathbf{p}}) + \right.\\
&\qquad \left. \sum_{\mathbf{k},\mathbf{k}',\mathbf{q}} \mathcal{D}(\mathbf{k},\mathbf{k}') f^\dagger_{1,\mathbf{q}+\mathbf{k}'-\mathbf{k}} f_{1,\mathbf{q}} \alpha^\dagger_{\mathbf{k}'} \alpha_{\mathbf{k}} \right),
\end{aligned}
$$

where $\alpha_{\mathbf{q}}$ (or $\alpha^\dagger_{\mathbf{q}}$) is the Bogoliubov phonon annihilation (or creation) operator, $\mathcal{R}_{\mathbf{p}} = u_{\mathbf{p}} - v_{\mathbf{p}}$, $\mathcal{D}(\mathbf{k},\mathbf{k}') = u_{\mathbf{k}}u_{\mathbf{k}'} + v_{\mathbf{k}}v_{\mathbf{k}'}$ and $u_{\mathbf{k}}$, $v_{\mathbf{k}}$ are the coefficients of the Bogoliubov transformation. An approximation, $N_0 = \sum_{\mathbf{k}} \langle b^\dagger_{\mathbf{k}} b_{\mathbf{k}} \rangle \approx \sum_{\mathbf{k}} b^\dagger_{\mathbf{k}} b_{\mathbf{k}}$, has been used during the above derivation and N_0 is the BEC number. E_g is a constant ground-state energy. The first term in H_I gives the conventional mean-field interaction with the mean-field energy shift $\Delta_{MF} = g_{bf}n_0$ and the BEC density $n_0 = N_0/V$. The second term in H_I is identical to the coupling term in the Fröhlich Hamiltonian Eq. (3.1). The third term is a scattering term.

To be in the Fröhlich polaron regime, it was pointed out that the condensate depletion in the vicinity of an impurity needs to be small, which gives rise to a constraint [47, 48]

$$
|g_{bf}| \ll 4\hbar c_s \xi^2 \Longrightarrow \left(\frac{m_b + m_f}{m_f}\right)^2 4\pi^3 a^2_{bf} a_{bb} n_0 \ll 1, \qquad (3.4)
$$

where the speed of sound in the BEC is $c_s = \sqrt{g_{bb}n_0/m_b}$ and the healing length of the BEC is $\xi = 1/\sqrt{8\pi a_{bb} n_0}$. Under this constraint, the third term in H_I can be ignored and Eq. (3.3) is

identical to Eq. (3.1). Further, Eq. (3.4) can be reduced to [48]

$$\epsilon \equiv 2\pi^{3/2}\left(1+\frac{m_b}{m_f}\right)|a_{bf}|\sqrt{a_{bb}n_0} \ll 1.$$

As discussed in Ref. [48][1] , when choosing $\epsilon \leq 0.3$ as the boundary for being in the Fröhlich regime, one obtains the maximum BEC density

$$n_0^{\max} = \left[\frac{\epsilon}{2\pi^{3/2}(1+m_b/m_f)}\right]^2 \frac{1}{a_{bb}a_{bf}^2},$$

below which the Bose polaron can be treated as the Fröhlich polaron. For our ^{40}K and ^{87}Rb system, Fig. 3.1(a) shows the regime where it is valid to treat the Bose polaron as the Fröhlich polaron. Another important quantity for discussing the Fröhlich polaron is the polaronic coupling constant

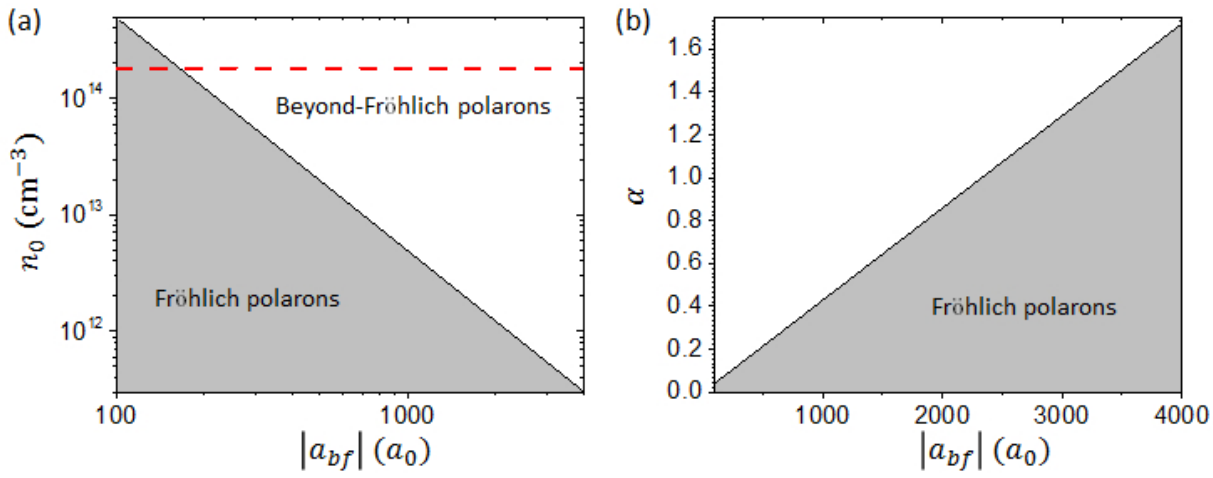

Figure 3.1: The regime where the Bose polaron behaves as a Fröhlich polaron. For our system, the boson is a ^{87}Rb atom and the fermion is a ^{40}K atom. (a)A plot that shows the valid regime for treating the Bose polaron as a Fröhlich polaron. The red dashed line indicates the typical peak BEC density in our experiment. (b)The maximum polaronic coupling constant achievable for the Fröhlich polaron.

$$\alpha \equiv 2\sqrt{2\pi}\sqrt{\frac{n_0}{a_{bb}}}a_{bf}^2.$$

According to Ref. [48], when the value of α is larger than one, the Fröhlich polaron is in an interesting intermediate coupling regime. By substituting the maximum BEC density $n_0^{\max}$ into

[1] The numerical table given in this paper about $n_0^{\max}$ and $\alpha_{\text{Rb-K}}^{\max}$ may be wrong. I suspect that they misused the Rb mass for the impurity mass, M, and the K mass for the majority mass, m.

the above equation, we get the maximum α allowed for the Fröhlich polaron as shown in Fig. 3.1(b). At a BEC density of $n_0 = 1.8 \times 10^{14}$ cm^{-3}, the corresponding critical scattering length is $a_{bf} = 170\ a_0$ and the maximal polaronic coupling constant is $\alpha_{\max} = 0.12$. Therefore, from Fig. 3.1(a), we can see that for our experimental conditions, the Bose polaron is outside the regime where the Fröhlich approximation is valid and all interaction terms in Eq. (3.3) need to be considered. From the phase boundary shown in Fig. 3.1(b), we note that reaching $\alpha > 1$ in the Fröhlich regime would require $|a_{bf}| > 2,500\ a_0$, which, as seen from the phase boundary shown in Fig. 3.1(a), corresponds to a BEC density more than two orders of magnitude smaller than in our experiment.

Bose polaron theory in the strongly interacting regime In the regime of strong impurity-boson coupling, beyond the Fröhlich approximation, one must consider Eq. (3.3). There are two published analytical methods that were used to solve for the Bose polaron in the strongly interacting regime: the T-matrix method [9] and the variational method [10]:

- The T-matrix method can be used to calculate the self-energy $\Sigma_f(\Omega, p)$ of the impurities [9]. The retarded Green's function and the spectral function of the polaron can be calculated using

$$\begin{aligned} G_f^R(\Omega, \mathbf{p}) &= \frac{1}{\hbar\Omega - \frac{\mathbf{p}^2}{2m_f} - \Sigma_f(\Omega, \mathbf{p}) + i0^+}, \\ A_I(\Omega, \mathbf{p}) &= -2\ \mathrm{Im}G_f^R(\Omega, \mathbf{p}), \end{aligned} \tag{3.5}$$

  where Ω is the energy and $\mathbf{p}$ is the momentum of the polaron. The quasiparticle dispersion relation is defined as the solution of

$$E(p) - \frac{p^2}{2m_f} - \mathrm{Re}\Sigma_f[E(p), p] = 0,$$

  where quantities depend only on the magnitude of momentum $p = |\mathbf{p}|$. The spectral weight or quasi-particle residue, which describes how much the bare atom is involved in the polaron state, is given by

$$Z(p) = \left. \frac{1}{1 - \partial_\Omega \mathrm{Re}\Sigma_f[\Omega, p]} \right|_{\Omega = E(p)/\hbar}.$$

The decay width is obtained from

$$\gamma(p) = -Z(p)\ \mathrm{Im}\Sigma_f[E(p), p].$$

At the small momentum limit of $p \sim 0$, the effective mass of the Bose polaron satisfies, $E(p) = E_0 + \frac{p^2}{2m_{\mathrm{eff}}} + \mathcal{O}(p^4)$, and can be obtained using

$$m_{\mathrm{eff}} = \left.\frac{p}{\partial_p E(p)}\right|_{p=0} = \left.\frac{m_b/Z(p)}{m_b/m_f + \frac{1}{p}\partial_p \mathrm{Re}\Sigma_f[\Omega, p]|_{E(p)}}\right|_{p=0},$$

with a simplification [9]

$$m_{\mathrm{eff}} = m_f \left(\frac{1 + m_f/m_b}{Z + m_f/m_b}\right), \tag{3.6}$$

for a noninteracting BEC.

- The variational method gives a trial wave function of polarons as [10]

$$|\Phi(\mathbf{q})\rangle \sim \left(\phi_0(\mathbf{q}) f^\dagger_{1,\mathbf{q}} + \sum_{\mathbf{k}\neq 0} \phi_{\mathbf{k}}(\mathbf{q}) f^\dagger_{1,\mathbf{q}-\mathbf{k}} \alpha^\dagger_{\mathbf{k}}\right) |\mathrm{BEC}\rangle, \tag{3.7}$$

which has a total momentum $\mathbf{q}$. The first term corresponds to bare impurity atom involved in the polaron state and its coefficient has a connection with the quasi-particle residue through $|\phi_0(\mathbf{q})|^2 = Z(\mathbf{q})$. The second term describes a phonon excitation of the condensate with wavevector $\mathbf{k}$.

In our experiment, we use ^{40}K atoms as impurities in a ^{87}Rb BEC. To approach the impurity/polaron limit, we tune the populations of the two species so that the number ratio $N_{\mathrm{K}}/N_{\mathrm{BEC}} \approx$ 0.1 and estimated ratio of the peak densities is $n_{\mathrm{K}}/n_{\mathrm{BEC}} < 0.04$. The fermionic impurity atoms have $T/T_F > 0.6$ and therefore we expect that their quantum statistics is not important [49]. For our weakly interacting BEC, the boson-boson scattering length is $a_{\mathrm{BB}} = 100a_0$ [50]. Following other papers [9, 10], we define energy and momentum scales respectively by

$$E_{\mathrm{n}} = \hbar^2(6\pi^2 n_{\mathrm{BEC}})^{2/3}/2m_{\mathrm{Rb}}, \qquad k_{\mathrm{n}} = (6\pi^2 n_{\mathrm{BEC}})^{1/3}. \tag{3.8}$$

Here a_0 is the Bohr radius, $\hbar = h/2\pi$ with h being the Planck constant and m_{Rb} is the mass of a Rb atom. An s-wave Feshbach resonance is used to control the interactions through the impurity-boson

scattering length $a_{\rm IB}$ for ^{87}Rb atoms in the $|f, m_f\rangle$=$|1, 1\rangle$ state and fermionic ^{40}K atoms in the $|9/2, -9/2\rangle$ state (see Sec. 1.3), where f corresponds to the atomic angular momentum and m_f is its projection.

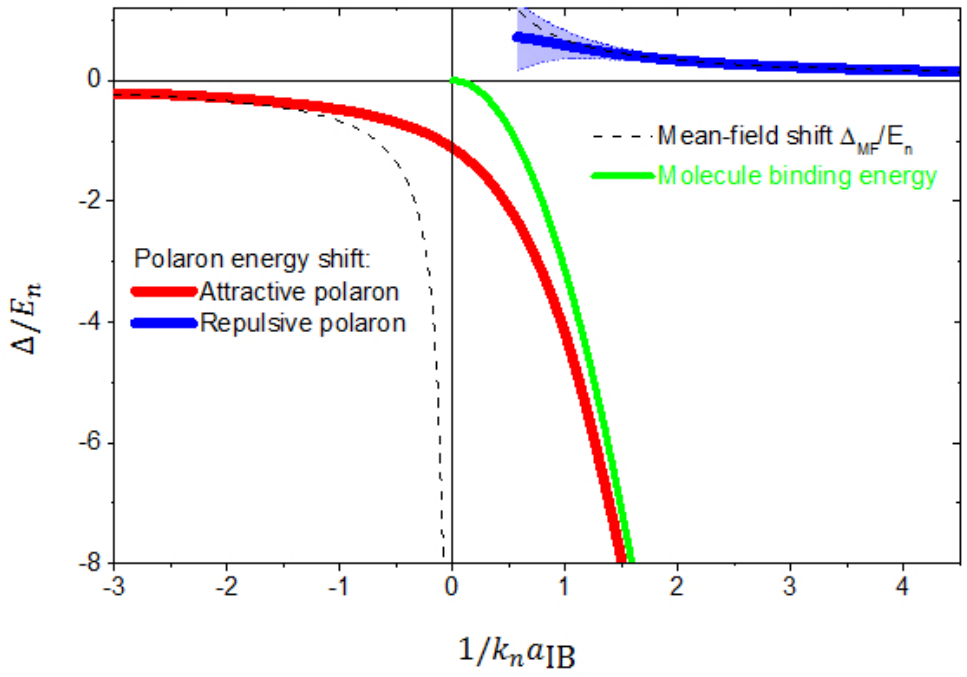

Figure 3.2: Predicted energy spectrum of an impurity immersed in a Bose-Einstein condensate with tunable impurity-boson interactions. The red and blue lines represent two polaronic branches that are called attractive polarons and repulsive polarons, respectively. For comparison, the green line shows the two-body molecular bound state energy, $-E_b/E_n = -m_{\rm Rb}/\mu_{\rm KRb}/(k_{\rm n}a_{\rm IB})^2$, with $\mu_{\rm KRb}$ being the reduced mass of a Rb atom and a K atom. For comparison, we also plot energy shifts based on the mean-field calculation (dashed lines) with $\Delta_{\rm MF}/E_n = (2m_{\rm Rb}/3\pi\mu_{\rm KRb})(k_{\rm n}a_{\rm IB})$.

In Fig. 3.2, we show the calculated energies of Bose polaron states as function of the interaction strength in the zero-temperature and zero-momentum limit. The theoretical lines are based on a T-matrix approach presented in Ref. [9] and similar results have been obtained with a variational approach in Ref. [10]. The spectrum has two quasiparticle branches: the attractive branch (red line) and the repulsive branch (blue line). The energies in the two branches shift in opposite directions from the non-interacting case ($\Delta = 0$ axis). In the weakly interacting limit, the energy shift approaches the mean-field shift (dashed lines), $\Delta_{\rm MF}/E_n = (2m_{\rm Rb}/3\pi\mu_{\rm KRb})(k_{\rm n}a_{\rm IB})$.

The two branches have different properties. For the repulsive branch, the polaron is a well-defined particle state only in the weakly interacting regime or the large $1/(k_{\rm n}a_{\rm IB})$ regime, where the lifetime is long and therefore the spectroscopic width of the polaron is narrow. In the strongly interacting regime, or the small $1/(k_{\rm n}a_{\rm IB})$ regime, the polaron lifetime becomes short and the energy level is broadened as indicated by the shaded regime. For the attractive branch, the polaron state is the ground state of the Hamiltonian and is well-defined in both the weakly interacting regime and the strongly interacting regime. In particular, the attractive polaron state exists at unitarity ($a_{\rm IB} \to \infty$) and is predicted to approch a weakly bound molecular state (green line) on the $a_{\rm IB} > 0$ side of the Feshbach resonance.

Fig. 3.3 shows the corresponding residue Z and effective mass $m_{\rm eff}$ at different interaction strengths. When there is no impurity-boson coupling, $Z = 1$ and $m_{\rm eff} = m_{\rm K}$. For the attractive branch, as the interaction strength $1/k_n a_{\rm IB}$ increases towards the positive $a_{\rm IB}$ side of the Feshbach resonance, $Z \to 0$ and $m_{\rm eff} \to (m_K + m_{\rm Rb})$, as the polaron approaches a two-body bound state or molecule [9].

Three-body recombination In the Bose polaron theory presented thus far, three-body recombination has been ignored. However, this process, in which three atoms collide inelastically and form a diatomic molecule, and typically release enough energy to eject all three atoms from the trap, exists in all Bose gases and Bose-Fermi gas mixtures. Moreover, with tunable interactions, the three-body recombination rate has an a^4 dependence that results in a dramatic increase of atom loss rates near a Feshbach resonance. Three-body recombination will limit the lifetime of Bose polarons. For our system, the three-body recombination happens between two Rb atoms and one K atom and can be described by [51]

$$\frac{d}{dt}n_K = -\frac{1}{2!}\alpha n_K n_{\rm BEC}^2,$$

where n_K ($n_{\rm BEC}$) is the K density (BEC density) and the factor of 1/2! is included for a BEC compared to a noncondensed ultracold gas of bosons. Here α is the three-body recombination rate coefficient for uncondensed bosons, which scales as $a_{\rm IB}^4$ (ignore Efimov structure). For a large

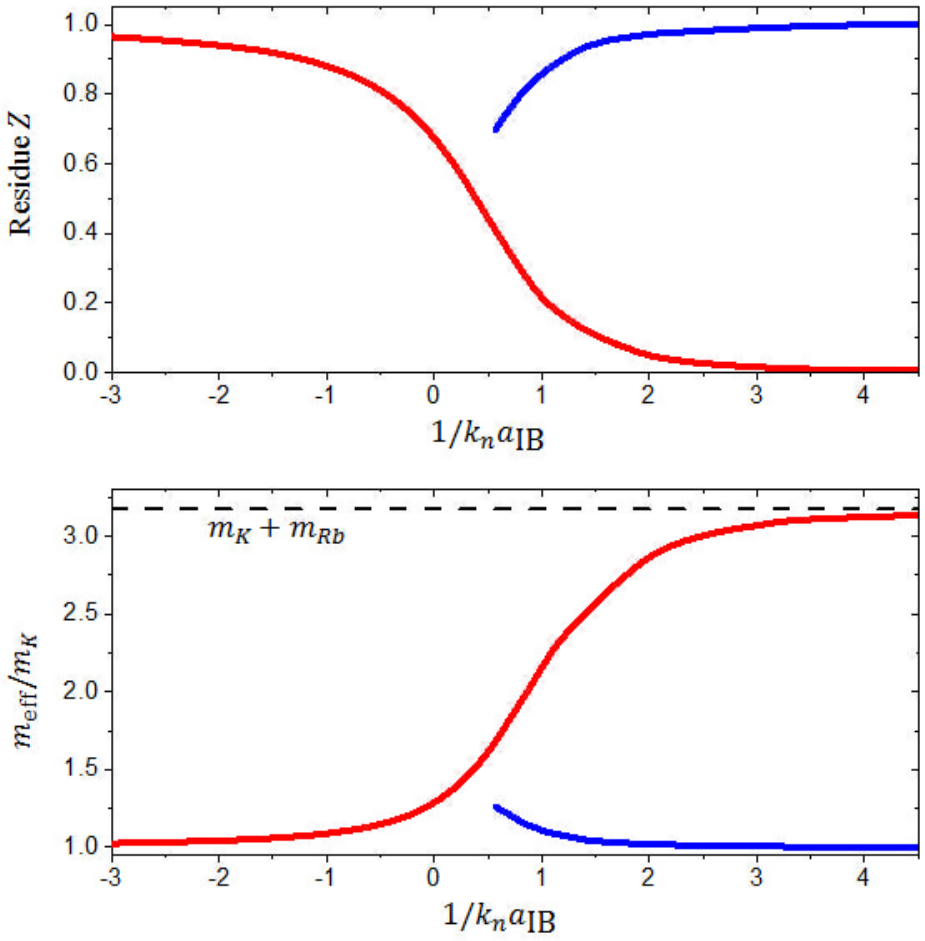

Figure 3.3: Residue and effective mass calculated from the T-matrix method. (a) Residue Z at different interaction strengths. (b) Effective mass $m_{\rm eff}/m_{\rm K}$ from Eq. (3.6) at different interaction strengths. The red line shows the attractive polaron branch, while the blue line shows the repulsive polaron branch.

population imbalance, the above equation can be simplified to

$$\frac{d}{dt}N_K = -\frac{1}{2!}\alpha n_{\rm BEC}^2 N_K,$$

which has the solution $N_K(t) = N_K(0)\exp(-\Gamma_3 t)$ with the loss rate $\Gamma_3 = \frac{1}{2}\alpha n_{\rm BEC}^2$. To continue our discussion, let me rewrite α as $\alpha = A_3 a_{\rm IB}^4$ [52] with A_3 being a constant. The values of α have been measured at different values of $a_{\rm IB}$ in our previous work [21]. We find $A_3 = 1.1 \times 10^{-8}$ m^2/s for $a_{\rm IB} < 0$ and $A_3 = 3.3 \times 10^{-8}$ m^2/s for $a_{\rm IB} > 0$ by fitting our data to $\alpha = A_3 a_{\rm IB}^4$. To compare

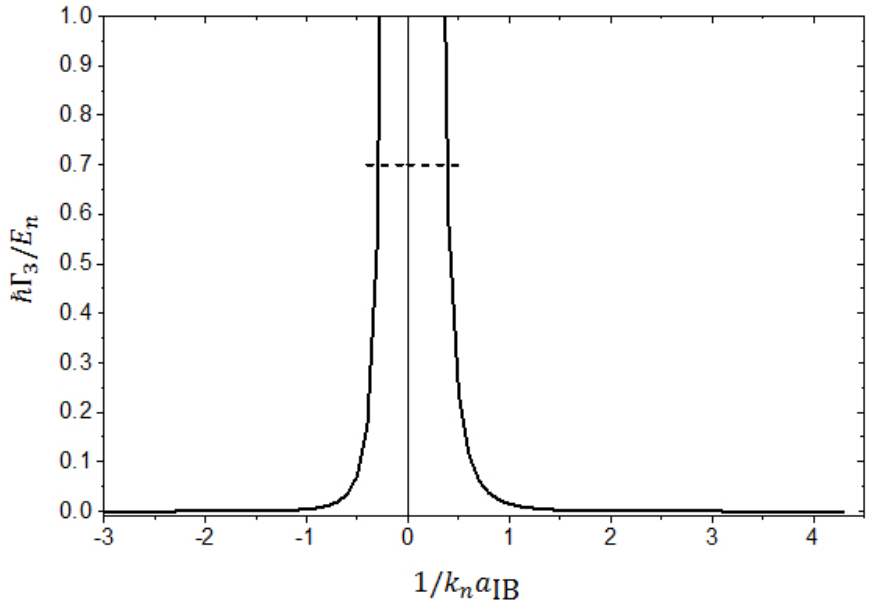

Figure 3.4: Three-body recombination loss rate. It is obtained using Eq. (3.9), which breaks down at small $|1/k_n a_{\mathrm{IB}}|$. As a consequence, Γ_3 will saturate at small $|1/k_n a_{\mathrm{IB}}|$. The dashed line is used to illustrate this saturation behavior, although the saturation value is uncertain yet.

with the energy shifts of Bose polarons, we can express the loss rate Γ_3 in terms of E_n and $1/k_n a_{\mathrm{IB}}$:

$$\hbar\Gamma_3/E_n = \kappa_3 (k_n a_{\mathrm{IB}})^4, \tag{3.9}$$

where $\kappa_3 = \frac{A_3 m_{\mathrm{Rb}}}{(6\pi^2)^2\hbar}$ is a dimensionless quantity. We calculate $\kappa_3 = 0.004$ for $a_{\mathrm{IB}} < 0$ and $\kappa_3 = 0.015$ for $a_{\mathrm{IB}} > 0$.

Fig. 3.4 shows this three-body recombination loss rate of the impurity atoms based on Eq. (3.9). However, a limitation of Eq. (3.9) is the assumption that α scales as a_{IB}^4, which breaks down in the regime where $|1/k_n a_{\mathrm{IB}}|$ is small. In this regime, α will saturate and a dashed line in Fig. 3.4 is used to illustrate this saturation behavior, although the saturation value is uncertain yet. From Fig. 3.2 and 3.4, we can see that the three-body recombination rate becomes comparable with the predicted energy shifts around $|1/k_n a_{\mathrm{IB}}| \sim 0.5$. Thus, a challenge for detecting Bose polarons in the strongly interacting regime will be the finite lifetime due to three-body collisional loss.

Efimov effect Ref. [12] theoretically considers the effect of Efimov trimers on the Bose

polaron. The authors consider an Efimov resonance at $a_- = -50\ a_{bb}$ and predict that close to $1/k_n a_-$, both the energy and residue of the Bose polaron would deviate from that calculated without considering the Efimov effect. However, for our system, the location of the Efimov resonance is predicted to be $a_- < -30,000 a_0$ [53], which is consistent with a measurement by our group [21]. The Efimov effect on the Bose polaron at such large scattering length would only affect an extremely narrow regime in $1/k_n a_{\mathrm{IB}}$ and we do not expect to resolve this.

3.2 RF spectroscopy of the Bose polaron

As discussed in the previous section, the Bose polaron is a rich quantum many-body effect that is an important paradigm in condensed matter physics. Ultracold atoms, with their interactions tunable with a Feshbach resonance, provide a unique opportunity to experimentally explore the Bose polaron. In particular, we can go to regimes where the interparticle interactions are very strong and where the physics goes beyond the often considered Fröhlich polaron. The regime of strong impurity-boson interactions has recently been treated theoretically; however, there are thus far no experimental results probing the Bose polaron in a strongly interacting regime.

In contrast, impurities in a Fermi gas of atoms have been studied experimentally using RF spectroscopy [27, 29, 30, 31]. Our experiment will employ similar techniques as these Fermi polaron measurements. However, there are some important differences between the Bose polaron and the Fermi polaron. First, the Bose polaron problem is arguably richer because there are two relevant interaction parameters: a_{BB} and a_{IB}, whereas there is no equivalent of a_{BB} in a spin-polarized Fermi gas. Second, on the experimental side, we will see that three-body inelastic loss and the relatively small spatial extent of a BEC (compared to an impurity gas) both create challenges to polaron measurements.

To measure the energy spectrum of the impurities immersed in a BEC, we perform radio-frequency (RF) spectroscopy on ^{40}K impurty atoms. The impurity atoms are initially prepared in a weakly interacting state, $|0\rangle = |9/2, -7/2\rangle$ and then, are driven into the strongly interacting $|1\rangle = |9/2, -9/2\rangle$ state by a RF pulse at frequency ν (see Fig. 3.5(a)). The RF power is typically

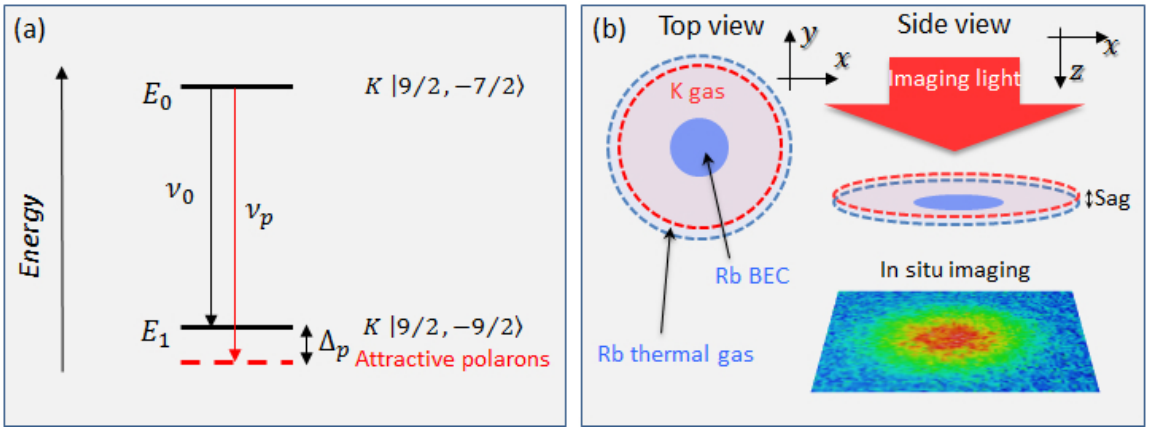

Figure 3.5: RF spectroscopy of the Bose polaron. (a) Energy diagram for the RF spectroscopy. (b) The spatial distribution of the trapped gases along with the imaging axis.

set to give a π-pulse for the bare atom transition. Impurity atoms in the $|1\rangle$ state are imaged immediately after the RF pulse. This spectroscopy of RF injection into the strongly interacting state minimizes the three-body losses. We denote the transition frequency of bare ^{40}K atoms by ν_0. The RF pulse has a gaussian envelop with the Fourier transformed RF lineshape being $\mathcal{R}(\nu) \propto \exp(-2\nu^2/\delta\nu^2)$ (see appendix A). The Fourier limited linewidth $\delta\nu$ is inversely proportional to the pulse duration, $\delta\nu = 1/(\pi\Delta t)$, with Δt being the $1/e^2$ width of the gaussian pulse envelop for the RF power. The RF pulse is applied from $t = -2\Delta t$ to $t = 2\Delta t$.

An experimental challenge arises from the very different cloud sizes for the impurity gas and the BEC as shown in Fig. 3.5(b). In our system, the measured trapping frequencies for K atoms are $\omega_\rho^K = 2\pi \times 50$ Hz and $\omega_z^K = 2\pi \times 281$ Hz and the trapping frequencies for Rb atoms are $\omega_\rho^{Rb} = 2\pi \times 39$ Hz and $\omega_z^{Rb} = 2\pi \times 183$ Hz. The two clouds also separate along the vertical direction due to differential gravitational sag which is given by $sag = g[1/(\omega_z^{Rb})^2 - 1/(\omega_z^K)^2] = 4$ μm. The cloud size of the impurity gas is about twice that of the BEC. As a result, only about 15% of the ^{40}K atoms overlap the BEC. By imaging the spin-flipped ^{40}K atoms in situ with a probe beam propagating along z and with a resolution well below the BEC size, we can select out signal that comes from ^{40}K atoms near the center of the BEC in the transverse direction.

However, the imaging integrates through the cloud in z and therefore the issue of signal from ^{40}K atoms outside the BEC, as well as from regions of lower BEC density, remains. We deal with this remaining density inhomogeneity issue by (1) using the transverse size of the imaged atoms to know when the signal is dominated by ^{40}K atoms that overlap with the BEC, and (2) performing an inverse Abel transform of this data to extract the central density. The inverse Abel transform allows one to find the central density where one assumes a symmetry between an imaged direction (transverse) and the integration direction (z). Differential gravitational sag breaks this symmetry, however, because of attractive mean-field interactions in the initial gas, this density profile of the ^{40}K atoms has approximate symmetry about the BEC center. We have modeled the effect of density inhomogeneity and sag on RF spectroscopy in the mean-field regime and found that the inverse Abel transform returns the correct central density of the cloud of spin-flipped ^{40}K atoms (see Sec. 3.5.2).

In Fig. 3.6(a-c), I show typical RF spectroscopy data at a weak interaction strength with $1/k_n a_{\mathrm{IB}} = -2.3$. The center optical depth (OD) and root-mean-square (RMS) width of the impurity atom cloud are obtained here by fitting the image to a 2D gaussian distribution. To distinguish signal that is dominated by ^{40}K atoms overlapping with the BEC, we use the cloud size. Open circles are used to denote the bare atom signal, while the Bose polaron signal is represented by red dots. Red dots are selected based on when the imaged cloud size is smaller than or equal to the measured BEC size (see Fig. 3.6(c)). Fig. 3.6(d) shows the number of spin-flipped atoms averaged over a circular annulus with the radius $\rho = 28$ μm. At this radius, the ^{40}K atom do not overlap the Rb BEC and we obtain the RF spectra for the bare atom transition. The frequency ν_0 is obtained by fitting this data to a gaussian lineshape $\mathcal{R}(\nu - \nu_0)$ (see Eq. (A.6) in appendix A). The fit result is indicated by the black line. Fig. 3.6(e) shows the peak density (normalized) obtained using an inverse Abel transform. We only show the data where the signal is dominated by ^{40}K atoms overlapping with the BEC (red dots). We normalize the measured peak density of the spin-flipped atom cloud to the calculated peak density of the impurity atoms. This calculation uses the measured ^{40}K atom number & BEC number, as well as the gas temperature measured

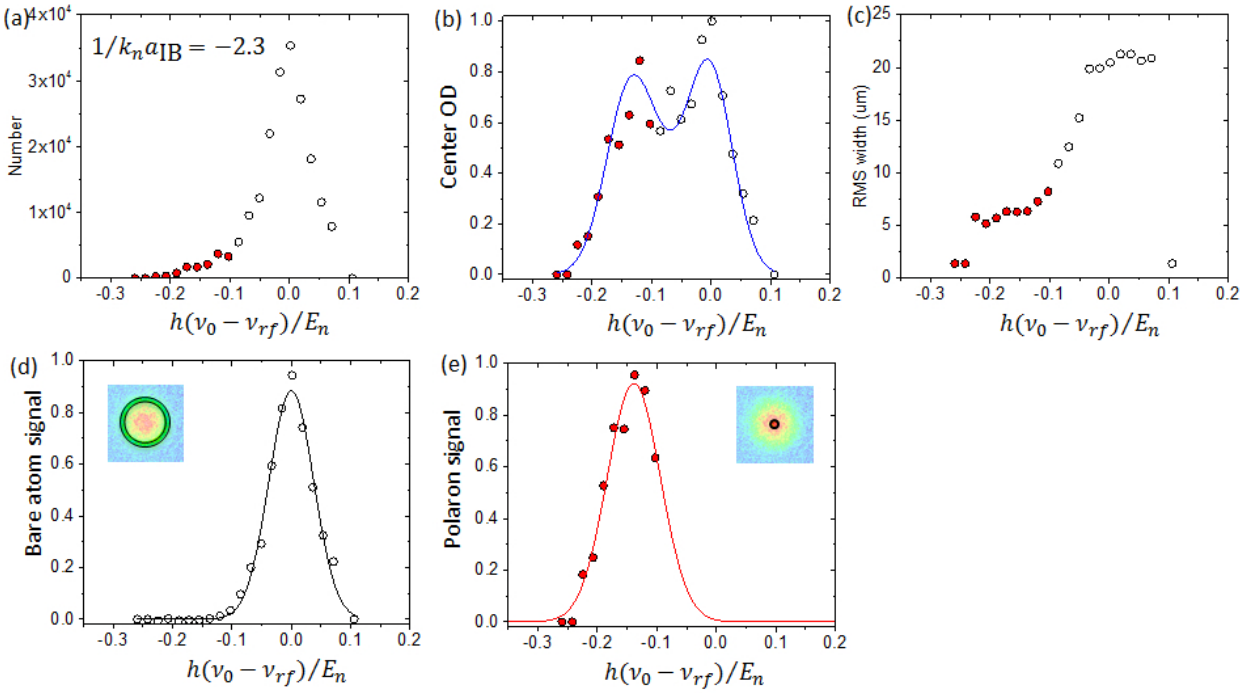

Figure 3.6: RF spectroscopy of the Bose polaron. (a-c) Typical RF spectroscopy data at a weak interaction strength of $1/k_n a_{\mathrm{IB}} = -2.3$. Red dots mark data where the imaged cloud size is less than or equal to the BEC size. (b) Here the center OD data are normalized to its highest value. The blue line is a fit to a mean-field model described by Eq. (3.20). (d) RF spectroscopy on the bare atom transition. Here the bare atom signal is obtained by averaging over a circular annulus with the radius $\rho = 28$ μm (inset) and is normalized to its highest value. The line is a fit to the spectral function, $\mathcal{R}(\nu - \nu_0)$, from which we get the bare atom transition, ν_0. (e) RF spectroscopy showing the signal from atoms located at the center of the BEC. We only use data where the imaged cloud has a width smaller than or equal to the BEC size. A gaussian function, Eq. (3.10), is used to fit our data (red line) with the fitting result of $x_0 = 0.139$ and $w = 0.045$ (the Fourier width $h\delta\nu/E_n$ should be compared to $2w$).

from the tail of the initial ^{40}K cloud.

Comparing Fig. 3.6(a) and 3.6(d), one can see that when just looking at the number of spin-flipped atoms, most of the signal comes from the large fraction (85%) of ^{40}K atoms that do not overlap the BEC. The width of the main feature here, which corresponds the bare atom transition, comes from the Fourier width of the RF pulse. The duration of the gaussian RF pulse for this data is $4\Delta t = 0.52$ ms, which gives a Fourier width of $\delta\nu = 1/(\pi\Delta t) = 2.4$ kHz and $h\delta\nu/E_n = 0.09$. Here, E_n (and k_n) are calculated from the measured peak BEC density of ^{87}Rb atoms in trap using

Eq. (3.8).

Looking at the central optical depth of the imaged (spin-flipped) atoms (Fig. 3.6(b)), we see roughly equal contributions from atoms that overlap with the BEC (red dots) and atoms that outside the BEC in the vertical imaging direction. Finding the central 3D density of the imaged atoms, by applying an inverse Abel transform to the images, allows us to extract an RF spectrum from only impurity atoms that are located within the BEC (Fig. 3.6(e)). Here, we can fit to a gaussian lineshape

$$y(x) = A\exp[-(x-x_0)^2/(2w^2)], \tag{3.10}$$

to extract the center $x_0 = 0.139$ and the RMS width $w = 0.045$ (red line). Note that here our Fourier limited width $h\delta\nu/E_n$ should be compared to $2w$ from the fit.

3.3 Energy spectrum of the Bose polaron

Fig. 3.7 shows selected RF spectra at different interaction strengths obtained using an inverse Abel transform to extract the signal from the center of the BEC. For cyan dots, we set the pulse duration to be $4\Delta t = 0.52$ ms except for $1/k_n a_{\mathrm{IB}} = -2.9$ and 4.4, where we set the pulse duration to be $4\Delta t = 0.9$ ms so that the Fourier width is $\delta\nu = 1$ kHz (or $h\delta\nu/E_n = 0.035$). The RF power is set to give a π-pulse for the bare atom transition. The yellow dot corresponds to data taken with a $4\Delta t = 0.52$ ms RF 5π-pulse. Black dots show data taken with a $4\Delta t = 0.1$ ms RF π-pulse (Fourier width $\delta\nu = 13$ kHz and $h\delta\nu/E_n = 0.5$). For each RF spectrum shown in Fig. 3.7, we observe a peak structure with a spectral width that broadens for larger interaction strengths. Using a gaussian fit described by Eq. (3.10), we extract the energy shift, the peak height, and the spectral width, which are shown in Fig. 3.8.

From Fig. 3.8, we see that the spectral width broadens for larger interaction strengths and the peak height becomes correspondingly smaller. One thing that can cause a broadened spectral width is the lifetime or the width of the energy level. The three-body recombination can cause inelastic collision and therefore affect the lifetime of the energy level (see Fig. 3.4). In addition, the

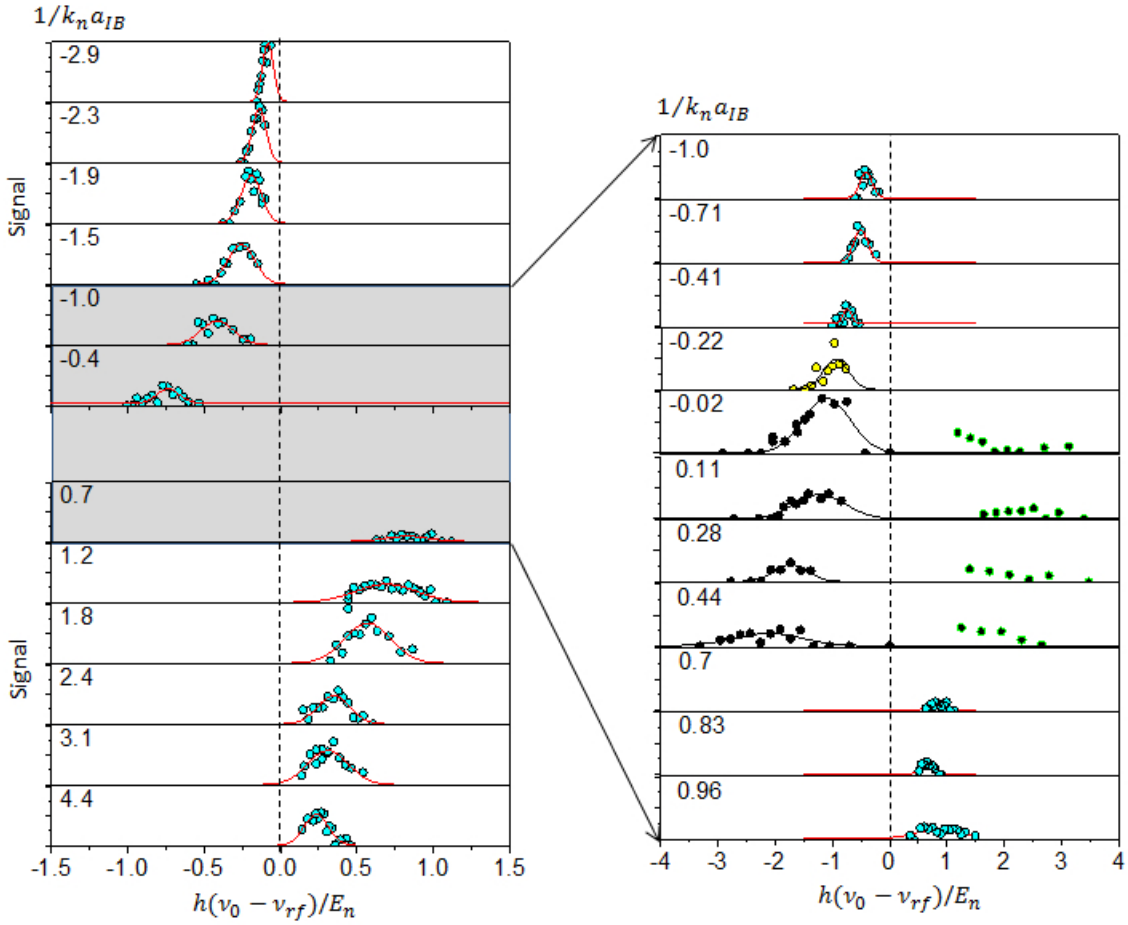

Figure 3.7: RF spectra of Bose polarons. Use data where the imaged cloud has a width smaller than or equal to the BEC size. We use an inverse Abel transform to obtain the signal from impurity atom within the BEC. For cyan dots, we set the pulse duration to be $4\Delta t = 0.52$ ms except for $1/k_n a_{\rm IB} = -2.9$ and 4.4, where we set the pulse duration to be $4\Delta t = 0.9$ ms. The RF power is set to give a π-pulse for the bare atom transition. The yellow dot corresponds to data taken with a $4\Delta t = 0.52$ ms RF 5π-pulse. Black dots show data taken with a $4\Delta t = 0.1$ ms RF π-pulse. The green circles represent data that may come from incoherent excitations (see Sec. 3.5.3), which do not contribute to polaron signals.

repulsive polaron state can decay to the attractive polaron state, which broadens the energy width of the repulsive polaron state. From the cyan dots as shown in Fig. 3.8, we see that the spectral widths on the $a > 0$ side are broadened more than these on the $a < 0$ side. Although the density inhomogeneity can cause a broadened spectral width, its effect is relatively small.

To extract the polaron energy shift from the RF spectra, we need to account for the mean-

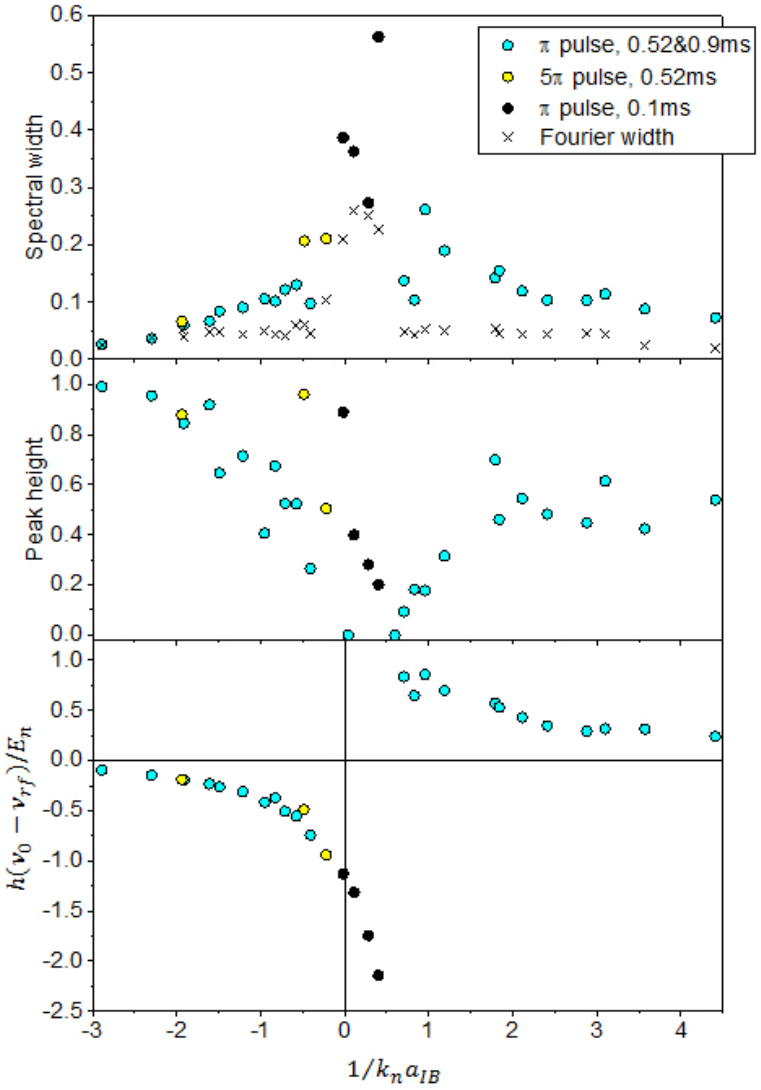

Figure 3.8: Summary of the RF spectra. The bottom panel shows the energy shifts. The middle panel shows the corresponding peak height. The top panel shows the spectral width.

field shift in the initial gas. The initial $|0\rangle$ state of the impurity atoms has a weak background interaction with the BEC atoms described by the background scattering length $a_{bg} = -187\ a_0$ [32]. This gives a mean-field energy shift of $E_{bg} = g_{bg} n_{\mathrm{BEC}}$, where $g_{bg} = 2\pi a_{bg}\hbar^2/\mu_{\mathrm{KRb}}$. The energy shift of the Bose polaron is thus

$$\Delta = h(\nu_0 - \nu_{rf}) + E_{bg}. \tag{3.11}$$

For our case of averaged peak BEC density, $n_{\mathrm{BEC}} = 1.8 \times 10^{14}$ cm^{-3}, $E_n/h = 28.4$ kHz and $E_{bg} =$

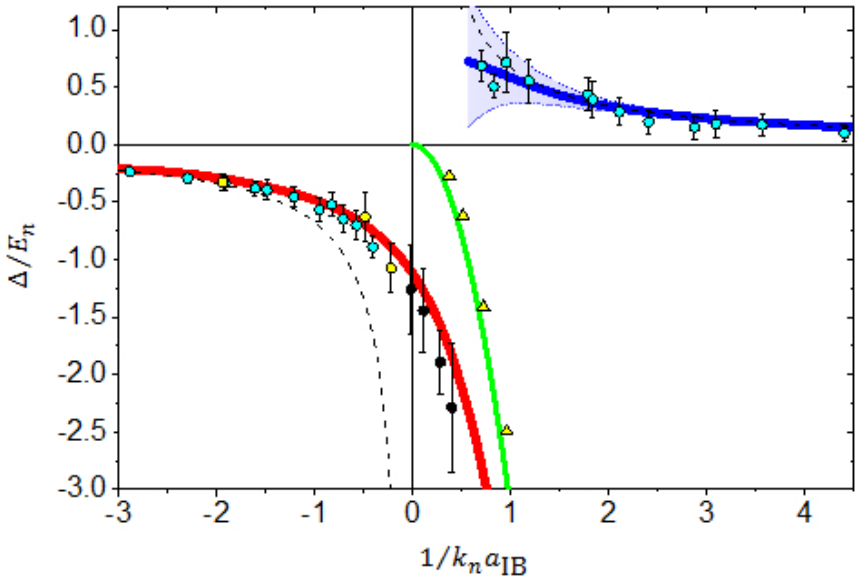

Figure 3.9: Measured energy shift of the Bose polaron (circles) and weakly bound molecules (triangles). The error bar of the energy shift corresponds to the RMS width of a gaussian fit, Eq. (3.10), to the RF spectra (see Fig. 3.7). Yellow triangles show data for K-Rb Feshbach molecules. The binding energy of K-Rb Feshbach molecules is extracted by fitting our K-Rb RF association data to a well-established model [32].

$-0.14E_n$. Fig. 3.9 shows the measured energy shift, Δ, as a function of the interaction strength. Cyan dots denote the data shown in Fig. 3.7. We also include measurements of the binding energy of weakly bound molecules using RF association as shown by the yellow triangles. These molecule data come from K atoms that do not overlap with the BEC, and spectra corresponding to the data are presented in Sec. 3.5.4.

From Fig. 3.9, we can see that our measured energy shift of the impurities immersed in the BEC matches well with that predicted recently for the Bose polaron (red and blue lines) in the regime of strong impurity-boson interactions. In particular, our data are consistent with a polaron state (red line) that exists across unitarity ($1/k_n a_{\mathrm{IB}} \to 0$) with an energy that approaches that of a weakly bound molecular state (green line) on the $a_{\mathrm{IB}} > 0$ side of the Feshbach resonance. Note that the theory line for the molecular state comes from a two-body theory.

Ideally, RF spectroscopy of polarons can be used to extract the residue, Z, of the polaron

by integrating the spectrum over the whole frequency range. This has been used experimentally to extract the residue of the Fermi polaron [27], which is a quasiparticle formed by an impurity interacting with a Fermi gas. However, extracting Z in this way requires that the data is taken in the linear regime, where the signal is proportional to the product of RF power and pulse duration. As discussed in the next section, our data is not always taken in this linear regime. In addition, losses could affect our data. While atom loss in a Fermi gas is suppressed due to the Pauli exclusion principle, for our Bose-Fermi gas mixture, three-body recombination can cause significant atom loss in the strongly interacting regime. This could result in a reduced signal strength in the RF spectroscopy.

3.4 Coherent Rabi oscillation and damping of the Bose polaron

Another important property of Bose polarons is the quasiparticle's residue Z, which describes how much the excitation or quasiparticle looks like a non-interacting particle. This can be seen in the trail variational wavefunction given in Eq. (3.7), where $Z(\mathbf{q}) = |\phi_0(\mathbf{q})|^2$. For our experiment, the temperature $T \approx 150$ nK, which corresponds to a momentum of the impurity atom $p_T = \sqrt{m_K k_B T} = 0.16\ \hbar k_n$. The kinetic energy of $k_B T \approx 0.12 E_n$ is small compared to the measured energy shift (see Fig. 3.8) so that the momentum of the impurity atom approximates to zero. When performing a Rabi oscillation between the polaron state, $|\Phi(\mathbf{p})\rangle$, and the non-interacting bare atom state, $|0\rangle$, with zero momentum, the residue Z is related to the Rabi frequency Ω through $\sqrt{Z} = \Omega/\Omega_0$ [29]. Here Ω_0 is the Rabi frequency for non-interacting atoms. To understand this relation and further extend it to a useful form for discussing our measurement, let me start with the RF Hamiltonian in the Shrödinger picture described by (see Eq. (A.3))

$$\hat{\mathcal{H}}_{rf}(\Omega_0) = \hbar\frac{\Omega_0}{2}\sum_{\mathbf{k}}\left(f_{1,\mathbf{k}}^{\dagger} f_{0,\mathbf{k}} + H.c.\right),$$

with the basis $\{|0\rangle|\mathrm{BEC}\rangle, |\Phi(0)\rangle\}$ for the Rabi oscillation between the polaron state and the non-interacting bare atom state. Here we only consider the zero-momentum polaron state, $|\Phi(0)\rangle$, due to the momentum conservation of the RF process. In the following discussion, I denote $|0\rangle|\mathrm{BEC}\rangle$

simply by $|0\rangle$. The time-dependent wavefunction, $|\psi(t)\rangle = C_0(t)|0\rangle + C_1(t)|\Phi(0)\rangle$, can be expressed as a vector, $|\psi(t)\rangle = (C_0(t), C_1(t))^T$ (T denotes the transpose operation). The Schrödinger equation is thus written as

$$\begin{aligned} i\hbar\partial_t \begin{pmatrix} C_0(t) \\ C_1(t) \end{pmatrix} &= \begin{pmatrix} \langle 0|\hat{\mathcal{H}}_{rf}(\Omega_0)|0\rangle & \langle 0|\hat{\mathcal{H}}_{rf}(\Omega_0)|\Phi(0)\rangle \\ \langle \Phi(0)|\hat{\mathcal{H}}_{rf}(\Omega_0)|0\rangle & \langle \Phi(0)|\hat{\mathcal{H}}_{rf}(\Omega_0)|\Phi(0)\rangle \end{pmatrix} \begin{pmatrix} C_0(t) \\ C_1(t) \end{pmatrix} \\ &= \begin{pmatrix} 0 & \hbar\frac{\Omega_0}{2}\phi_0 \\ \hbar\frac{\Omega_0}{2}\phi_0^* & 0 \end{pmatrix} \begin{pmatrix} C_0(t) \\ C_1(t) \end{pmatrix}, \end{aligned} \tag{3.12}$$

with an initial condition of $C_0(0) = 1$ and $C_1(0) = 0$. To obtain Eq. (3.12), Eq. (3.7) has been used and $\phi_0 = \phi_0(\mathbf{q} = 0)$. Solving the above equation, we get the population of impurity atoms in the polaron state as

$$|C_1(t)|^2 = \sin^2\left(\frac{dE_0}{2}|\phi_0|t\right), \tag{3.13}$$

where d is the induced electrical dipole moment of atoms and E_0 is the electric field amplitude of the RF pulse.

If we fix E_0 and vary t, Eq. (3.13) describes a Rabi oscillation in time with

$$|C_1(t)|^2 = \sin^2\left(\frac{\Omega}{2}t\right),$$

where $\Omega = dE_0|\phi_0|$ is the Rabi frequency of polarons. The Rabi frequency of non-interacting impurty atoms is $\Omega_0 = dE_0$. The residue Z can be obtained using the relation of $(\Omega/\Omega_0)^2 = |\phi_0|^2 = Z$. This relation has been used in Ref. [29] to measure the residue of the Fermi polaron.

Equivalently, if we fix t and vary E_0, Eq. (3.13) describes a Rabi oscillation in E_0 with

$$|C_1(E_0)|^2 = \sin^2\left(\frac{\tilde{\Omega}}{2}E_0\right), \tag{3.14}$$

where $\tilde{\Omega} = d|\phi_0|t$ is an equivalent Rabi frequency. The equivalent Rabi frequency for non-interacting impurity atoms is $\tilde{\Omega}_0 = dt$. The quasiparticle's residue Z can be obtained using

$$Z = |\phi_0|^2 = (\tilde{\Omega}/\tilde{\Omega}_0)^2. \tag{3.15}$$

This relation is particularly useful for measuring the Bose polaron's residue using the Rabi oscillation described by Eq. (3.14), because the three-body recombination loss of impurity atoms

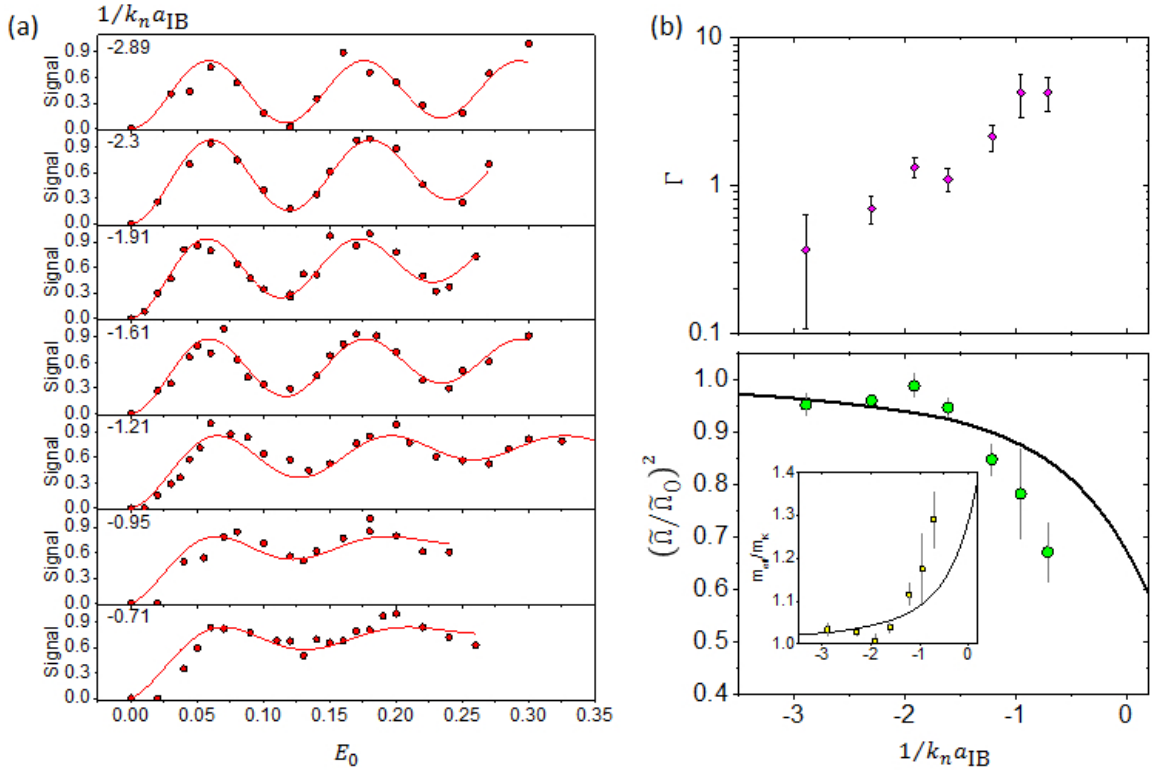

Figure 3.10: Coherent Rabi oscillation for the Bose polaron. (a) Rabi oscillation of Bose polarons at different interaction strengths. The signal is from the center OD and normalized to the highest value in each data set. Red lines are fits to Eq. (3.16). (b) The damping rate Γ and residue $Z = (\tilde{\Omega}/\tilde{\Omega}_0)^2$ from the Rabi oscillation. The inset shows the effective mass of the Bose polaron obtained by using Eq. (3.6). Lines are the calculated values based on the T-matrix method.

exponentially depends on t and is independent of E_0. By fixing t and varying E_0, the effect of the three-body loss on the Rabi oscillation frequency is minimized, which helps accurately measuring Z.

In our experiment, we perform the Rabi oscillation between the polaron state and the weakly interacting initial state $|0\rangle$. Two period of oscillation is achieved by varying the RF power, while fixing the pulse duration to $4\Delta t = 0.4$ ms and RF frequency at ν_p. The Rabi oscillation in a function of the electric field amplitude, E_0, of the RF pulse has a form as shown in Eq. (3.14) and we plot our Rabi signal versus E_0 in Fig. 3.10(a).

The Rabi oscillation gets slower as expected at higher interaction strength. In addition, it

also shows a damping on the oscillation amplitude as well as a growing incoherent signal added to the oscillation offset. Such decoherence behavior was also observed in Fermi polaron experiments [29, 30], in which it was explained due to two-body collisions. As indicated by the red lines in Fig. 3.10(a), we fit our data to an empirical model described by

$$y(x) = A\left[e^{-2\Gamma x}\sin^2\left(\frac{\tilde{\Omega}}{2}x\right) + \left(1 - e^{-2\Gamma x}\right)\right], \tag{3.16}$$

where x is E_0 and $\tilde{\Omega}$ is the equivalent Rabi frequency. The first term is the coherent part with the damping rate Γ and the second term is the incoherent part. The Rabi frequency, $\tilde{\Omega}_0$, of bare K atoms is obtained by performing the same RF pulse on K atoms in the absence of Rb atoms. When the interaction strength gets larger, the damping rate becomes higher and eventually it washes out the oscillation pattern as $1/k_n a_{\mathrm{IB}} > -0.7$ in our experiment. For the repulsive polaron, the damping is so fast that we cannot see any oscillation pattern until the interaction strength is lowered to $1/k_n a_{\mathrm{IB}} \geq 3.57$. This difference from the attractive case may be a comprehensive result of the finite lifetime and the incoherent RF excitation (see Sec. 3.5.3) of the repulsive polaron.

In Fig. 3.10(b), the damping rate as well as the fractional Rabi frequency at different interaction strengths are shown. From the upper panel of Fig. 3.10(b), we see that the damping rate Γ increases as the interaction strength $1/k_n a_{\mathrm{IB}}$ increases and saturates at $1/k_n a_{\mathrm{IB}} \geq -1$, where the measured values of $(\tilde{\Omega}/\tilde{\Omega}_0)^2$ deviate from the theoretical prediction (black line). When $1/k_n a_{\mathrm{IB}} < -1$, the measured values of $(\tilde{\Omega}/\tilde{\Omega}_0)^2$ agree with the theoretical prediction pretty well as shown in the lower panel of Fig. 3.10(b). The inset shows the effective mass of the polaron obtained using $m_{\mathrm{eff}}/m_{\mathrm{K}} = (1 + m_{\mathrm{K}}/m_{\mathrm{Rb}})/(Z + m_{\mathrm{K}}/m_{\mathrm{Rb}})$ (see Eq. (3.6)). We can see that the effective mass of the impurity atom becomes heavier at larger $1/k_n a_{\mathrm{IB}}$, which is due to the stronger polaronic coupling between the impurity and the BEC.

3.5 Data analysis in detail

3.5.1 A mean-field model of density inhomogeneity

An experimental challenge arises from the very different cloud sizes for the impurity gas and the BEC. This can be seen from the initial density distributions of the Rb BEC and K atoms in $|0\rangle$ state before a RF pulse

$$\begin{aligned} n_{\mathrm{BEC}}(\rho,z) &= n_0\left(1-\frac{\rho^2}{R_\rho^2}-\frac{z^2}{R_z^2}\right), \\ n_{K,0}(\rho,z) &= n_{\mathrm{pk}}\exp\left[-\frac{\rho^2}{2W_\rho^2}-\frac{(z-sag)^2}{2W_z^2}-g_{bg}n_{\mathrm{BEC}}(\rho,z)/k_BT\right], \end{aligned} \tag{3.17}$$

where the size of the BEC is charaterized by the Thomas-Fermi radius $\{R_\rho,\ R_z\}$ and that of the K cloud by the RMS width $\{W_\rho,\ W_z\}$. Here we assume thermal equilibrium and ignore the quantum statistics of the fermionic ^{40}K atom. The RMS width is related to the temperature T through $W_{\rho,z} = \sqrt{k_BT/m_{\mathrm{K}}}/\omega^K_{\rho,z}$. The gravitational sag between Rb and K cloud is given by $sag = g[1/(\omega_z^{Rb})^2 - 1/(\omega_z^K)^2]$ with g being the gravitational constant. Here, $\omega^K_{\rho,z}$ are the trapping frequencies of K atoms and $\omega^{Rb}_{\rho,z}$ the trapping frequencies of Rb atoms. The last term in n_K comes from the mean-field potential due to the Rb BEC with the coupling constant $g_{bg} = 2\pi a_{bg}\hbar^2/\mu_{\mathrm{KRb}}$ and $a_{bg} = -187a_0$ [32].

Fig. 3.11 shows the calculated density distributions of the initial impurity cloud and the BEC along z. The gravitational sag shifts the centers of the K and Rb clouds apart, which breaks the ellipsoidal symmetry of the system along z. On the other hand, the background impurity-boson interaction leads to an attractive mean-field potential for the impurity and thus results in an enhanced impurity density near the center of BEC, which tends to restore the ellipsoidal symmetry near the center of the BEC. In addition, to look at the symmetry of the impurity-boson system, it is instructive to write down the energy density functional [54]:

$$\begin{aligned} \mathcal{E}[n_{\mathrm{BEC}},n_{K,0}] &= g_{bb}n_{\mathrm{BEC}}(\rho,z)^2+\frac{3(6\pi^2)^{2/3}\hbar^2}{10m_{\mathrm{K}}}n_{K,0}(\rho,z)^{5/3}+g_{bf}n_{\mathrm{BEC}}(\rho,z)n_{K,0}(\rho,z), \\ &\quad +U_{\mathrm{BEC}}(\rho,z)n_{\mathrm{BEC}}(\rho,z)+U_{\mathrm{K}}(\rho,z)n_{K,0}(\rho,z), \end{aligned}$$

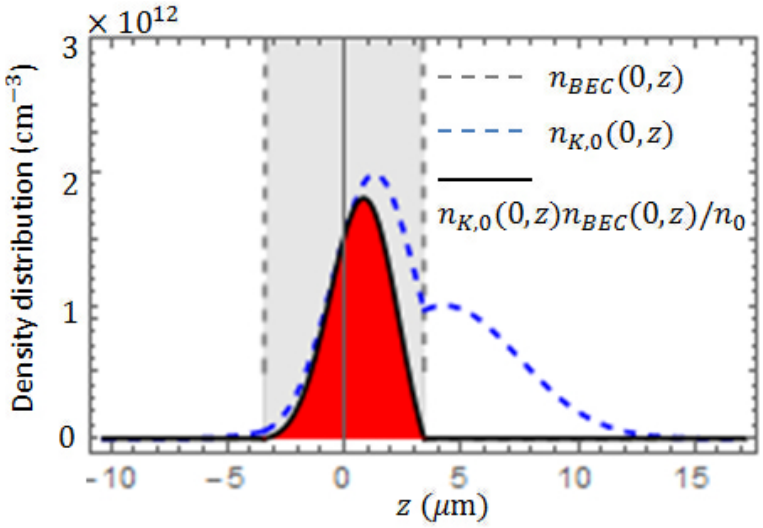

Figure 3.11: Density profile of the initial impurity cloud and the BEC based on Eq. (3.17). The BEC density $n_0 = 1.8 \times 10^{14}$ cm^{-3}, $R_z = 3.4$ μm, $W_z = 3.2$ μm, $sag = 4.3$ μm and $T = 153$ μK. The gray region represents the BEC density. The red regime denotes the weighted impurity density, $n_{K,0}(0,z)n_{\rm BEC}(0,z)/n_0$ (see Eq (3.18)).

where $U_{\rm BEC}(\rho,z)$ and $U_{\rm K}(\rho,z)$ are the external trapping potentials of the BEC and the K atoms respectively. In the limit of $n_{\rm BEC} \gg n_{K,0}$ near the BEC center, the energy density functional is simplified to

$$\mathcal{E}[n_{\rm BEC}, n_{K,0}] \;=\; g_{bb} n_{\rm BEC}(\rho,z)^2 + g_{bf} n_{\rm BEC}(\rho,z) n_{K,0}(\rho,z) + U_{\rm BEC}(\rho,z) n_{\rm BEC}(\rho,z), \quad (3.18)$$

where the first and third terms have ellipsoidal symmetry, and the second term has approximate ellipsoidal symmetry as shown by the red regime in Fig. 3.11. Thus the region near the center of the BEC has approximate ellipsoidal symmetry, which is important for us to use the inverse Abel transform discussed in Sec. 3.5.2.

After the RF pulse, the number of spin-flipped K atoms in $|1\rangle$ state near the cloud center ($\rho < \rho_0$) is modeled, based on Eq. (A.6), as

$$N_{K,1}(\nu, \rho \le \rho_0) = A \int_0^{\rho_0} \rho d\rho \int_{-\infty}^{\infty} dz \; n_{K,0}(\rho,z) \mathcal{R}(\nu - \nu_p \; n_{\rm BEC}(\rho,z)/n_0), \quad (3.19)$$

in which A is a constant and ν_p is the mean-field energy shift at the center of the BEC. The effect of a non-uniform BEC density is modeled using mean-field energy shift in $R(\nu - \nu_p \; n_{\rm BEC}(\rho,z)/n_0)$

[55]. The effect of finite imaging resolution can be modeled by convolving the above equation with a point spread function, for which we choose a gaussian function, $\exp\left(-\frac{\rho^2}{2\sigma_{res}^2}\right)$, with σ_{res} being the resolution. Thus Eq. (3.19) is modified as

$$\begin{aligned} N_{K,1}(\nu, \rho \leq \rho_0) &= A\int_0^{\rho_0} \rho d\rho \int_0^{\infty} \tilde{\rho} d\tilde{\rho} \exp\left[-\frac{(\tilde{\rho}-\rho)^2}{2\sigma_{res}^2}\right] \times \\ &\int_{-\infty}^{\infty} dz\; n_{K,0}(\tilde{\rho}, z)\mathcal{R}(\nu - \nu_p\; n_{\mathrm{BEC}}\,(\tilde{\rho}, z)/n_0)\,, \end{aligned} \tag{3.20}$$

which is a model that we use to understand the measured RF lineshape (see Fig. 3.6(b)) in the weak interaction or mean-field regime.

Fig. 3.12 shows different calculated RF lineshapes that illustrate the effects of the initial background mean-field potential, the size of the integrated area, the temperature, and the imaging resolution. There are two main features for the RF lineshape. The first one is the height of the polaron signal relative to the bare atom signal. From Fig. 3.12, we see that this height is sensitive to the initial background mean-field potential and the temperature. A deeper mean-field potential or lower temperature generates a higher height of the polaron signal. The second feature is the double-peak structure consisting of a bare atom peak and a polaron peak. The polaron peak structure turns out to be sensitive to the initial background mean-field potential as well as the resolution as shown in Fig. 3.12. A shallower mean-field potential or a bad imaging resolution (large σ_{res}) tends to flatten the polaron peak.

We fit our data shown in Fig. 3.6(b) to Eq. (3.20) with floating parameters $\{A, \nu_p\}$ and all other relevant quantities are obtained from the experimental measurements. The imaging resolution is measured by imaging a tiny BEC as point source and we get $\sigma_{res} = 3.4$ μm. The fitting result is shown in Fig. 3.6(b) as a blue line, which overlaps with our data very well at the negative a_{IB} side. The fit also gives the polaron energy shift ν_p at the BEC center.

Eq. (3.20) is the model that we used for understanding our RF lineshapes at the relatively weak interaction or mean-field regime with $1/k_n|a_{\mathrm{IB}}| > 1.5$. Once the interaction is strong enough, the above model is inadequate because the mean-field model breaks down. One needs to consider the quasiparticle residue Z as well as the three-body recombination collision into Eq. (3.20), which

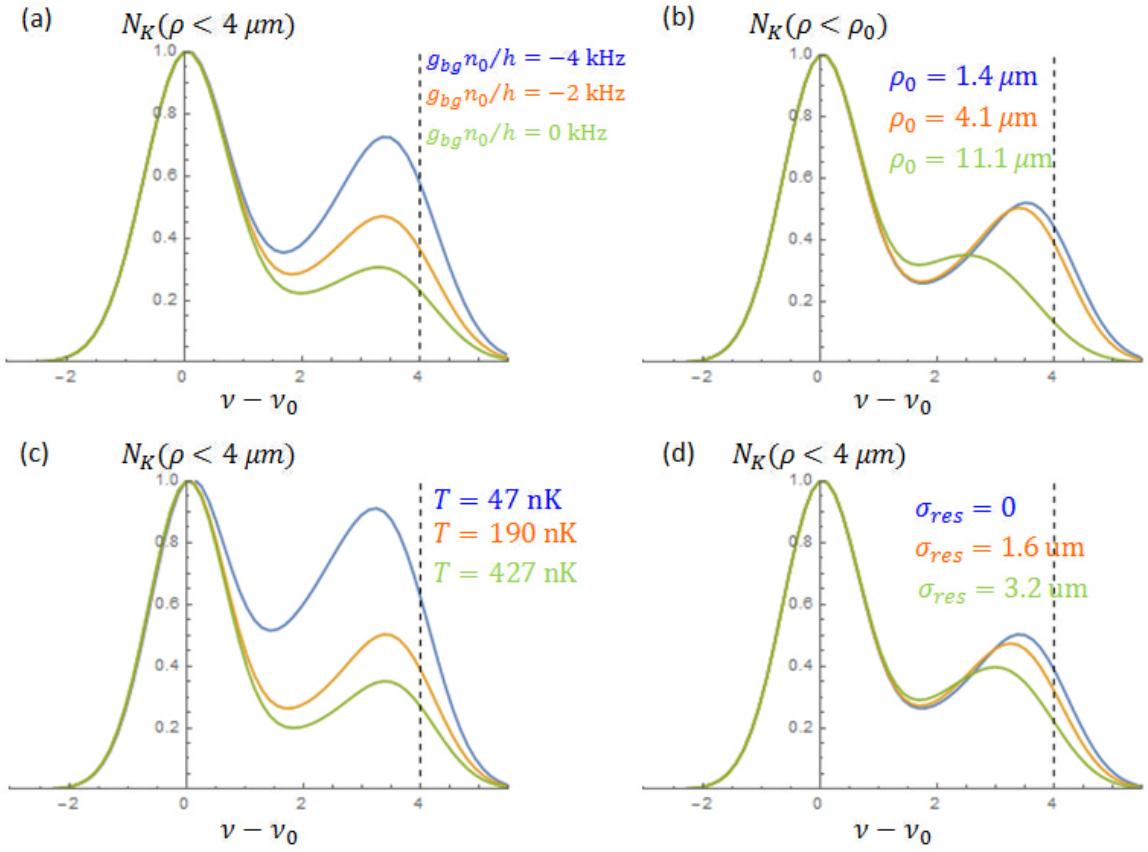

Figure 3.12: Calculated RF lineshapes based on Eq. (3.20). (a) RF lineshapes at different strengths of the initial background mean-field potential, $g_{bg}n_0$. Here $T = 190$ nK and $\sigma_{res} = 0$ μm. The actual $g_{bg}n_0/h = -4$ kHz. (b) RF lineshapes for different sizes of the integrated area. The radial size of the BEC is chosen to be $R_\rho = 15.2$ μm. Here $T = 190$ nK, $\sigma_{res} = 0$ μm and $g_{bg}n_0/h = -2$ kHz. The actual radius of the integrated area is 2.76 μm. (c) RF linesahpes at different temperatures. $T = 150$ nK in our experiment. (d) RF lineshapes for different imaging resolutions. Here $T = 190$ nK and $g_{bg}n_0/h = -2$ kHz. $\delta\nu$ is set to be 1.4 kHz. The measured resolution is $\sigma_{res} = 3.4$ μm. The dashed lines indicate the locations of ν_p.

is difficult.

3.5.2 Justification for inverse Abel transform

The inverse Abel transform can be used to calculate the three-dimensional density distribution from an two-dimensional absorption image. When the system has the spherical symmetry, cylindrical symmetry, or ellipsoidal symmetry. In the following, I focus on a system with the ellipsoidal

symmetry. In this case, we can define a "radius", $r = \sqrt{x^2 + b^2y^2 + c^2z^2}$, for the three-dimensional space and $\rho = \sqrt{x^2 + b^2y^2}$, for the two-dimensional space. The two-dimensional absorption image is denoted by $F(\rho)$ and the three-dimensional density distribution $f(r)$ is obtained using

$$f(r) = -\frac{1}{\pi}\int_r^\infty \frac{dF(\rho)}{d\rho}\frac{d\rho}{\sqrt{\rho^2 - r^2}}. \tag{3.21}$$

With the inverse Abel transform, we can potentially solve the non-uniform density issue in our Bose polaron study. However, the gravitational sag between the K cloud and Rb BEC breaks the ellipsoidal symmetry of our mixture system. In the following, we use a numerical simulation to show that the inverse Abel transform nevertheless works well for us to extract the RF spectrum of Bose polarons at the BEC core. This is because the region near the center of the BEC, which contains the signal we wish to extract, has approximate ellipsoidal symmetry. We calculate the inverse Abel transform using a matrix approach that was adapted from Eric Mueller and that is appropriate for an image with discrete points.

In our system, the measured trapping frequencies for K atoms are $\omega_\rho^K = 2\pi \times 50$ Hz and $\omega_z^K = 2\pi \times 281$ Hz and the measured trapping frequencies for Rb atoms are $\omega_\rho^{Rb} = 2\pi \times 39$ Hz and $\omega_z^{Rb} = 2\pi \times 183$ Hz. We estimate the gravitational sag using $sag = g[1/(\omega_z^{Rb})^2 - 1/(\omega_z^K)^2] = 4$ μm. In our simulation, we start from the density distributions given by Eq. (3.17). The radius $r = \sqrt{x^2 + y^2 + (\omega_z^K/\omega_r^K)^2 z^2}$ and $\rho = \sqrt{x^2 + y^2}$. The RF spectroscopy is modeled based on the mean-field theory and similar to Eq. (3.19), we use

$$n_{K,1}(r, \nu) = n_{K,0}(\rho, z)\mathcal{R}(\nu - \nu_p\, n_{\rm BEC}(\rho, z)/n_0), \tag{3.22}$$

to test how well the inverse Abel transform works for the purpose of extracting the RF spectroscopy signal of Bose polarons at the BEC center. From Eq. (3.22), we can also obtain a calculated absorption signal (column density)

$$\bar{n}_{K,1}(\rho, \nu) = \int_{-\infty}^{\infty} dz\; n_{K,0}(\rho, z)\mathcal{R}(\nu - \nu_p\, n_{\rm BEC}(\rho, z)/n_0),$$

for a RF frequency ν. By performing the inverse Abel transform on the 2D column density $\bar{n}_{K,0}$,

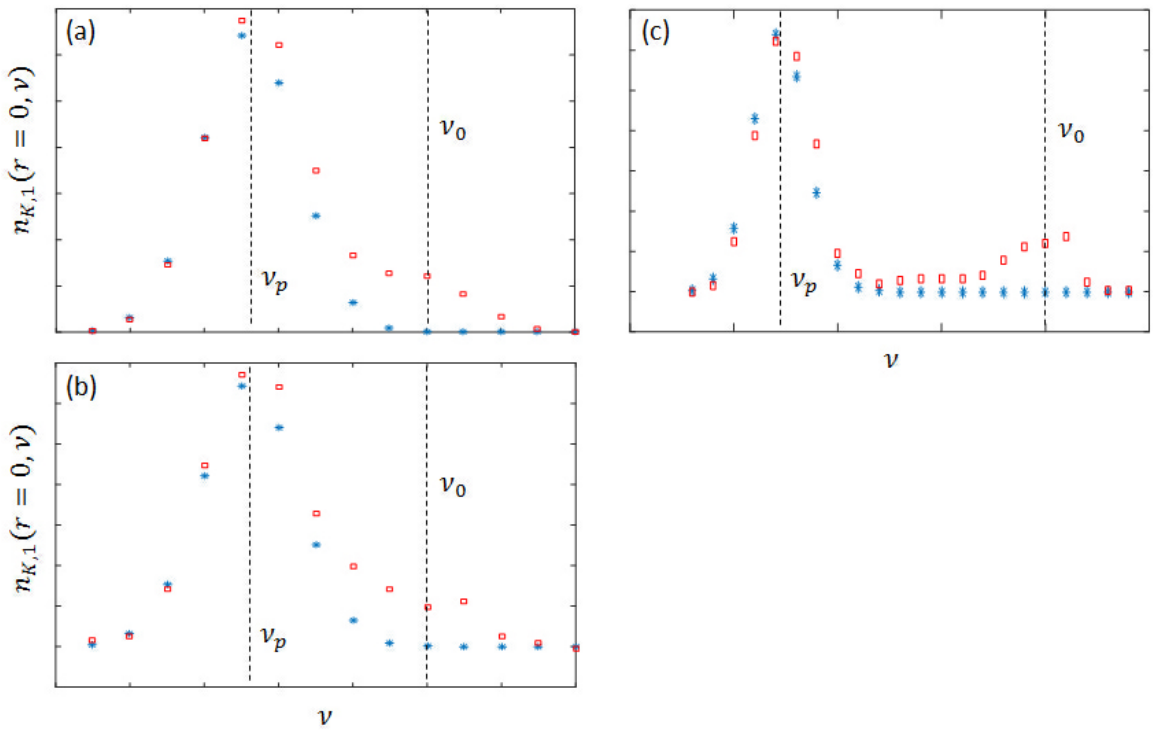

Figure 3.13: Simulated data for testing the inverse Abel transform for extracting the Bose polaron signal at the BEC center. The blue stars represent the expected RF spectrum, $n_{K,1}(r=0,\nu)$, based on Eq. (3.22). The red squares are the RF spectrum, $n_{K,1}^{Inv.Abel}(r=0,\nu)$, extracted from the inverse Abel transform based on Eq. (3.23). (a) RF spectrum with sag. (b) RF spectrum with noise added to the fake column density $\bar{n}_{K,1}(\rho,\nu)$ (10% multiplicative noise and 0.05 additive noise; both numbers are Gaussian standard deviations). (c) RF spectrum at a larger interaction strength.

we get

$$n_{K,1}^{Inv.Abel}(r,\nu) = \text{Inverse Abel transformation}\{\bar{n}_{K,1}(\rho,\nu)\}, \tag{3.23}$$

which is the three-dimensional density distribution of the spin-flipped K atoms by the RF pulse. Now we can compare $n_{K,1}^{Inv.Abel}(r=0,\nu)$ against $n_{K,1}(r=0,\nu)$ (Eq. (3.22)) at the BEC center.

Fig. 3.13 shows the simulation results. Around ν_p, the RF spectrum of Bose polarons overlaps with the expected very well, although it overestimates the signal around the bare atom transition ν_0. In Fig. 3.13(b), we add some noise to the fake column density $\bar{n}_{K,1}(\rho,\nu)$ to test the robustness of the inverse Abel method, and we find that noise does not change the results. In Fig. 3.13(c), we test the RF spectrum at a larger interaction strength and it works likewise.

3.5.3 Coherent and incoherent excitation spectrum

As observed in Fermi polaron experiments [27, 29], a spectrally broad incoherent signal along with the narrow coherent signal are excited when performing a RF spectroscopy on the Fermi polaron (a quasiparticle formed by an impurity interacting with a Fermi gas). This broad incoherent signal would affect the extracted value of the polaron energy if it wasn't treated correctly. The main contribution to this incoherent signal stems from the molecule-hole continuum (MHC) existing in the Fermi gas [29]. In contrast, for a Bose-Fermi gas mixture with the majority of bosons, this MHC is not important. Instead, other decoherence mechanism may exist leading to an incoherent signal [9, 56].

Based on the time evolution of impurities under the RF pulse, a generic feature of the RF response is given in Sec. IV.A of Ref. [56] and is adapted for our system as

$$I(\omega) = I_{\mathrm{coh}}(\omega) + I_{\mathrm{incoh}}(\omega), \tag{3.24}$$

$$I_{\mathrm{coh}}(\omega) = Z\delta(\omega - 2\pi\nu_p), \tag{3.25}$$

$$I_{\mathrm{incoh}}(\omega \ll 2\pi\nu_0) \propto C(2\pi\nu_0 - \omega)^{-3/2}, \tag{3.26}$$

where I is the RF response, Z is the quasiparticle residue, and C is the Tan's contact [57, 58]. The RF spectrum $I(\omega)$ consists of two parts, the coherent part I_{coh} and the incoherent part I_{incoh}. The incoherent part is due to dephasing and exists only when $\omega < 2\pi\nu_0$. Here a uniform BEC density is assumed and the RF fourier limited lineshape $\mathcal{R}(\nu)$ is not included. For the non-interacting case, $I_{\mathrm{coh}}(\omega) = \delta(\omega - 2\pi\nu_0)$ and $I_{\mathrm{incoh}} = 0$. By considering the RF fourier limited lineshape $\mathcal{R}(\nu)$, Eq. (3.24) becomes

$$\begin{aligned}\tilde{I}(\omega) &= \int_{-\infty}^{\infty} d\tilde{\omega}\mathcal{R}[(\tilde{\omega} - \omega)/2\pi]I(\tilde{\omega}) \\ &= Z\mathcal{R}(\nu_p - \omega/2\pi) + \int_{-\infty}^{\infty} d\tilde{\omega}\mathcal{R}[(\tilde{\omega} - \omega)/2\pi]I_{\mathrm{incoh}}(\tilde{\omega})\end{aligned} \tag{3.27}$$

where I set $\mathcal{R}(\nu) = \sqrt{\frac{2}{\pi}}\frac{1}{\delta\nu}\exp(-2\nu^2/\delta\nu^2)$. In particular, $\tilde{I}(\omega \ll 2\pi\nu_0) \propto C(2\pi\nu_0 - \omega)^{-3/2}$.

Fig. 3.14 shows the observation of the Tan's contact at both positive and negative interactions. As discussed above, the Tan's contact as a $\omega^{-3/2}$ tail shows up only at the $\nu < \nu_0$ side (green

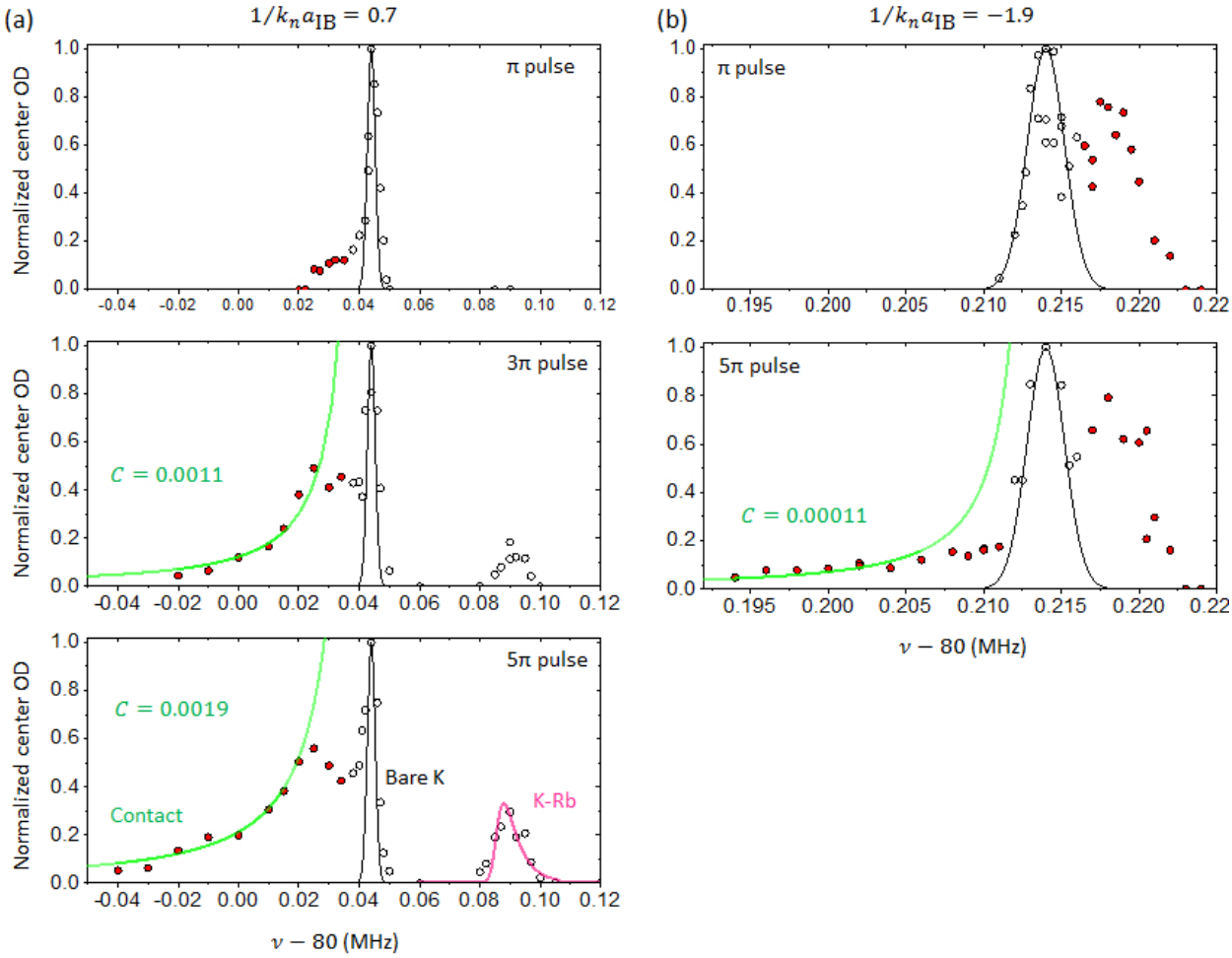

Figure 3.14: Tan's contact shown as a $\omega^{-3/2}$ tail in our RF spectroscopy data. Black lines indicate the bare atom transition. Red dots denote the data with the cloud size smaller than or equal to the BEC size. (a) RF spectroscopy at $1/k_n a_{\mathrm{IB}} = 0.7$. The RF pulse duration is fixed at $4\Delta t = 0.52$ ms. From the top to bottom, the RF power is increased to give a π pulse, 3π pulse, and 5π pulse. Green lines indicate the Tan's contact and come from fits of the RF tail to $C(2\pi\nu_0 - \omega)^{-3/2}$. Additionally, K-Rb Feshbach molecules are formed from the Rb thermal cloud as shown on the right corner and the pink line is a fit to a RF association model [32]. (b) RF spectroscopy at $1/k_n a_{\mathrm{IB}} = -1.9$. The RF pulse duration is fixed at $4\Delta t = 0.52$ ms. From the top to bottom, the RF power is increased to give a π pulse and 5π pulse. The red dots on the left indicate the Tan's contact tail, while the red dots on the right represent the attractive polaron signal.

lines). The fact that the cloud size of the contact signal is smaller than the BEC size (as indicated by the red color) means that the contact signal is from the ^{40}K atoms overlapping with the BEC. At relatively small RF power (e.g., π pulse), the contact signal is too small to be observable, which

is good for measuring the energy shifts of Bose polarons.

In conclusion, for the attractive polaron spectroscopy, the incoherent signal and the polaron signal are well separated in frequency and are on the opposite sides of the bare atom transition. For the repulsive polaron spectroscopy, although the incoherent signal and the polaron signal may overlap with each other, the polaron signal can still be selected out by choosing a RF pulse with relatively small RF power. Unfortunately, when performing a Rabi oscillation in terms of RF power, this incoherent signal will wash out the oscillation pattern immediately for the repulsive polaron.

3.5.4 RF association and dissociation of K-Rb Feshbach molecules

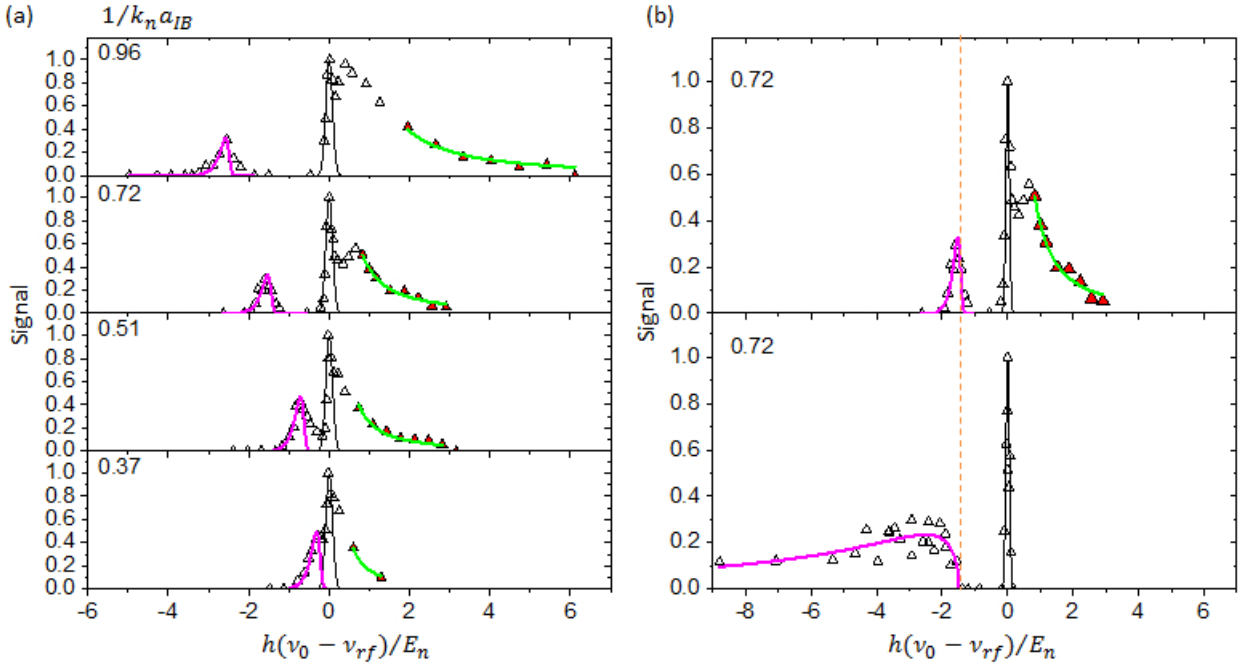

Figure 3.15: RF association and dissociation of K-Rb Feshbach molecules. (a) RF association of K-Rb Feshbach molecules at $1/k_n a_{\mathrm{IB}} = 0.96, 0.72, 0.51, 0.37$. The magenta line is obtained by fitting the molecule data to a well-established model [32]. The black line indicate the bare atom transition. The green line is the contact tail as discussed in the previous section. (b) RF dissociation of K-Rb Feshbach molecules at $1/k_n a_{\mathrm{IB}} = 0.72$ (bottom panel). The magenta line is a fit to a well-established model [59]. As a reference, the association data is shown in the upper panel. The dashed line indicates the location of the binding energy of molecules.

RF association of K-Rb Feshbach molecules has been well studied in [51] and [32]. Here

we measure the binding energy of K-Rb Feshbach molecules in the strongly interacting regime, where the binding energy follows a universal relation, $E_b/E_n = m_{\mathrm{Rb}}/\mu_{\mathrm{KRb}}/(k_n a_{\mathrm{IB}})^2$. Fig. 3.15(a) shows the data of RF associating K-Rb molecules. The binding energy is extracted by fitting the molecule data to a well-established model [32], which is indicated by the magenta line. The binding energy of K-Rb molecules is shown in Fig. 3.9 as yellow triangles, which match the universal theory line (green) very well. The RF pulse we used for associating K-Rb Feshbach molecules has a pulse duration $4\Delta t = 0.52$ ms and the RF power is set to give a 7π pulse. In addition, we also measured the binding energy by RF dissociating K-Rb molecules as shown in Fig. 3.15(b), which is in agreement with that measured by RF association. Here the K-Rb molecules were created by magneto-association described in our previous paper [20]. The dissociated K atoms are in $|9/2, -7/2\rangle$ state, which is directly imaged by using the non-cycling transition of $|9/2, -7/2\rangle \rightarrow |11/2, -9/2\rangle$ with the measured imaging efficiency of 80%.

3.6 Summary

I report experimental data probing Bose polarons using radio-frequency spectroscopy. We measure the excitation spectrum of fermionic ^{40}K impurities strongly interacting with a BEC of ^{87}Rb atoms. We find that the measured energy of the impurites immersed in the BEC matches well with that recently predicted for Bose polarons [9, 10] in the regime of strong impurity-boson interactions. In particular, our data are consistent with a polaron state that exists across unitarity ($a_{\mathrm{IB}} \rightarrow \infty$) with an energy that approaches that of a weakly bound molecular state on the $a_{\mathrm{IB}} > 0$ side of the Feshbach resonance. Furthermore, for attractive interactions, we observe Rabi oscillations when exciting Bose polarons. This work is the first measurement of the Bose polaron in a three-dimensional trapped atom gas and provides a starting point for understanding the quantum many-body physics of Bose-Fermi mixtures.

Chapter 4

Quantum Hall physics: bizarre and interesting

Ever since Edwin Hall discovered the Hall effect in 1879, measuring electrical conduction in a magnetic field has become one of the standard ways to characterize conductive materials. In 1980, Klaus von Klitzing discovered the integer quantum Hall (IQH) effect when he was measuring the Hall conductivity of a 2D semiconductor sample in a strong magnetic field ($B \sim$Tesla) (the 1985 Nobel prize in physics). What he found is that the Hall conductivity was exactly quantized at integer values of e^2/h. Here e is the charge of an electron and h is the Planck constant. Later the fractional quantum Hall (FQH) effect was discovered by Horst Störmer and Daniel Tsui and was partially explained by Robert Laughlin (the 1998 Nobel prize in physics). What they found is that the Hall conductance of a 2D electron gas shows precisely quantized plateaus at fractional values of e^2/h. FQH states represent new states of matter that contain a completely new kind of order—topological order, which cannot be described by the conventional theories. Thus they greatly enrich our understanding of quantum many-body physics and quantum phase transitions. However, there have been few experimental ways to locally detect these exotic states so far. Recently, ultracold atomic gases have been proposed as systems where experiment would be able to simulate the quantum Hall states and furthermore be able to detect the local properties of these states [15].

4.1 Classical Hall effect

The classical Hall effect is introduced and some important quantities are described here. Considering a 2D conductor exposed to an external magnetic field B along z, one can measure the

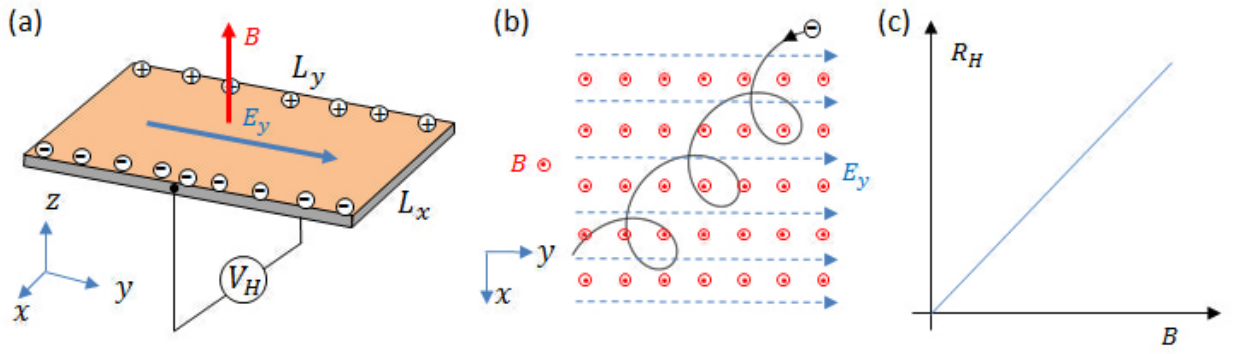

Figure 4.1: Classical Hall effect. (a) Measuring Hall conductance of a sample. An external electrical field E_y is along y and an external magnetic field B is along z. Hall voltage V_H as well as the normal current I along y are measured. (b) The helical motion of an electron moving on the x-y plane due to the Lorentz force based on Eq. (4.1). (c) The dependence of Hall resistance, R_H, on B based on Eq. (4.2).

conductance by applying an electric field E_y (or a voltage potential V) across the sample along y (see Fig. 4.1 (a)). Due to the Lorenz force, electrons are doing helical motion inside the sample and eventually reach the transverse edge (see Fig. 4.1 (b)). Thus, the transverse Hall voltage is produced by the accumulated electrons on the edge. In experiment, the electric current I along y and Hall voltage V_H along x are recorded. The normal resistance can be obtained using $R = V/I$, while the Hall resistance is $R_H = V_H/I$.

In the classical case, the Lorentz force felt by electrons is $\mathbf{F} = -e(\mathbf{E} + \mathbf{v} \times \mathbf{B})$. Here the electric field $\mathbf{E} = E_x\hat{\mathbf{x}} + E_y\hat{\mathbf{y}}$ with $E_y = V/L_y$ and $E_x = V_H/L_x$. L_x and L_y are the lengths of the sample along x and y, respectively. The constant magnetic field $\mathbf{B} = B\hat{\mathbf{z}}$. Combined with the Newton's equation, $\mathbf{F} = m_e\frac{d\mathbf{v}}{dt}$, we can get the velocity of an electron as

$$\mathbf{v}(t) = v_0\left[\cos(\omega_c t)\hat{\mathbf{x}} + \sin(\omega_c t)\hat{\mathbf{y}}\right] + \left(\frac{eE_y}{m_e\omega_c}\hat{\mathbf{x}} - \frac{eE_x}{m_e\omega_c}\hat{\mathbf{y}}\right), \tag{4.1}$$

where cyclotron frequency $\omega_c = eB/m_e$ and v_0 is the initial velocity. The first term in the above equation describes the cyclotron orbit and the second term represents a drift motion with the drift velocity $\mathbf{v}_d = \frac{eE_y}{m_e\omega_c}\hat{\mathbf{x}} - \frac{eE_x}{m_e\omega_c}\hat{\mathbf{y}}$. The electric current density is defined by $\mathbf{j} = -ne\mathbf{v}_d$ with n being the electron density. Thus we have $\mathbf{j} = -(ne/B)E_y\hat{\mathbf{x}} + (ne/B)E_x\hat{\mathbf{y}}$. According to the Ohm's law,

$\mathbf{j} = \sigma \cdot \mathbf{E}$ [1] , we have the conductivity, $\sigma_{xx} = \sigma_{yy} = 0$ and $\sigma_{xy} = -\sigma_{yx} = -ne/B$. The resistivity, as the inverse of the conductivity[2] , is $\rho_{xx} = \rho_{yy} = 0$ and $\rho_{xy} = -\rho_{yx} = 1/\sigma_{xy} = -B/ne$. Here the off-diagonal conductivity elements $\{\sigma_{xy}, \sigma_{yx}\}$ are called Hall conductivities. The Hall resistance (Hall conductance) turns out to be the same as the Hall resistivity (Hall conductivity). This can be seen from $R_H = V_H/I = E_x L_x/j_y L_x = E_x/j_y = 1/\sigma_{yx} = \rho_{yx}$. The value of the Hall resistance follows

$$R_H = \rho_{yx} = \frac{B}{ne}. \tag{4.2}$$

which depends linearly on B (see Fig. 4.1 (c)). Based on Eq. (4.2), the Hall effect has become an important way to measure the charge carrier density n.

All above discussions made use of classical mechanics, which should be valid when the magnetic field is small enough that no energy gap is opened up. Next, I will discuss the case of strong magnetic field, where the quantum mechanics is used.

4.2 Landau levels

Landau levels are a quantum mechanical effect of a magnetic field on the motion of charged particles moving in a 2D plane. In the presence of a uniform magnetic field perpendicular to the 2D plane, charged particles move along quantized orbits according to quantum mechanics and therefore the energy of these particles are quantized into a series of equally spacing energy levels, called Landau levels. For the case of a many-particle system, each of these Landau levels can be occupied by multiple particles due to the degeneracy, which depends on both the strength of the magnetic field and the size of the system. What surprising is that L. D. Landau discussed this physical system in 1930 [60], 50 years before people discovered the integer quantum Hall effect.

Consider electrons moving in the 2D x-y plane, which has an area $A = L_x L_y$ (see Fig. 4.1(a)).

---

[1] Here the Ohm's law is a two-dimensional formula: $\begin{pmatrix} j_x \\ j_y \end{pmatrix} = \begin{pmatrix} \sigma_{xx} & \sigma_{xy} \\ \sigma_{yx} & \sigma_{yy} \end{pmatrix} \begin{pmatrix} E_x \\ E_y \end{pmatrix}$.

[2] The resistivity $\rho = \sigma^{-1}$, which means $\rho_{xx} = \sigma_{yy}/(\sigma_{xx}\sigma_{yy} - \sigma_{xy}\sigma_{yx})$, $\rho_{yy} = \sigma_{xx}/(\sigma_{xx}\sigma_{yy} - \sigma_{xy}\sigma_{yx})$, $\rho_{xy} = -\sigma_{yx}/(\sigma_{xx}\sigma_{yy} - \sigma_{xy}\sigma_{yx})$, $\rho_{yx} = -\sigma_{xy}/(\sigma_{xx}\sigma_{yy} - \sigma_{xy}\sigma_{yx})$.

Applying an uniform magnetic field along z, it is well described by a single-body Hamiltonian [60]

$$\begin{aligned} H &= \frac{1}{2m_e}\left[\hat{\mathbf{p}}_\perp + \frac{e}{c}\mathbf{A}_\perp(x,y)\right]^2 \\ &= \frac{\hat{p}_x^2}{2m_e} + \frac{1}{2}m_e\omega_c^2\left(x - \frac{\hbar k_y}{m_e\omega_c}\right)^2 \qquad (4.3) \\ &= \frac{\hat{\mathbf{p}}_\perp^2}{2m_e} + \frac{1}{2}m_e(\omega_c/2)^2\rho^2 + (\omega_c/2)\hat{L}_z \qquad (4.4) \end{aligned}$$

where ω_c is the cyclotron frequency with $\omega_c = eB/m_e c$ (c is the speed of light). Here $\mathbf{A}(x,y)$ is the vector potential of the magnetic field with $\mathbf{A}_\perp = \{A_x, A_y\}$, the momentum operator $\hat{\mathbf{p}}_\perp = \{\hat{p}_x, \hat{p}_y\}$, and the radius $\rho^2 = x^2 + y^2$. $\hat{L}_z = x\hat{p}_y - y\hat{p}_x$ is the orbital angular momentum operator along z. Eq. (4.3) is obtained by using the Landau gauge, $\mathbf{A} = \{0, Bx, 0\}$ and Eq. (4.4) is gotten by using the symmetric gauge, $\mathbf{A} = \frac{1}{2}\{-By, Bx, 0\}$, both of which are identical with each other and satisfy $\nabla \times \mathbf{A} = B\hat{\mathbf{z}}$. Their eigenenergy is

$$E = (n + 1/2)\hbar\omega_c, \qquad (4.5)$$

where n is an integer taking values of $0, 1, 2\cdots$. Different values of n here represent different Landau levels. The wavefunctions for different gauges are different from each other. Both situations are useful for our discussions. The former is useful for explaining transport measurements and edge states, while the latter is useful for discussing the connection with a rotating gas.

For Eq. (4.3) associated with the Landau gauge, the eigenfunction is [60]

$$\psi_{n,k_y}(x,y) = e^{ik_y y}\phi_n(x - x_0), \qquad (4.6)$$

where n and k_y are quantum numbers, ϕ_n is the well-known wavefunction of an harmonic oscillator. The location of the harmonic oscillator is

$$x_0 = \frac{\hbar k_y}{m\omega_c}, \qquad (4.7)$$

where k_y is quantized due to the boundary condition and takes values $k_y = 2\pi n_y/L_y$ ($n_y = 0, 1, 2, \cdots, N_y$). Due to the constraint of $0 \le x_0 \le L_x$, we get $N_y = \mathrm{Int}(\Phi/\Phi_0)$ (Int means integer part) with $\Phi = BL_xL_y$ being the magnetic flux and $\Phi_0 = hc/e$ being the fundamental quantum of

flux. The degeneracy or the maximum number of particles per Landau levels is

$$D = (2s+1)\frac{\Phi}{\Phi_0}, \tag{4.8}$$

where s is the spin of an electron with $s = 1/2$. One important feature for Landau levels is the quantization of the cyclotron orbits. This can be seen by using a semi-classical picture: $E = (n+1/2)\hbar\omega_c = \frac{1}{2}m\omega_c^2 R_c^2$, which gives the quantized cyclotron orbits

$$R_c^2 = (2n+1)\frac{\hbar c}{eB}. \tag{4.9}$$

For Eq. (4.4) associated with the symmetric gauge, the eigenfunction is [61, 62]

$$\psi_{n,m}(x,y) = \frac{e^{|w|^2/2}\partial_+^m \partial_-^n e^{-|w|^2}}{\sqrt{\pi a_\perp^2 n! m!}}, \tag{4.10}$$

where n is the index of Landau levels, m is an "angular momentum" index with $\hat{L}_z|\psi_{nm}\rangle = \hbar(m-n)|\psi_{nm}\rangle$, $w = (x+iy)/a_\perp$, $a_\perp = \sqrt{2\hbar/m_e\omega_c}$, and $\partial_\pm = (a_\perp/2)(\partial_x \pm i\partial_y)$. Note that $a_\perp = \sqrt{2}l_B$ with the magnetic length $l_B = \sqrt{\hbar/m_e\omega_c}$. The degeneracy of each Landau level also follows Eq. (4.8).

For the lowest Landau level $n = 0$, the wavefunction is, $\psi_{0,m}(\rho,\phi) = e^{im\phi}e^{-\rho^2/2a_\perp^2}(\rho/a_\perp)^m/\sqrt{m!\pi}$, which carries angular momentum $m\hbar$. These states have a ring shape and the position of the maximum of $|\psi_{0,m}(\rho,\phi)|$ is at $\rho_{pk} = \sqrt{m}a_\perp$ (Fig. 4.2). The ring of the mth state has an area of $m\pi a_\perp^2$, with an enclosed magnetic flux $m\pi a_\perp^2 B = m\Phi_0$. Hence there is one flux quanta per state and the number of states in the lowest Landau level corresponds to the number of flux quanta. The many-body wavefunction for the lowest Landau level ($n = 0$) state has the form [63]

$$\begin{aligned}
\Psi_1(z_1,\cdots,z_N) &= \mathcal{A}[(z_1)^0(z_2)^1(z_3)^2\cdots]e^{-\sum_k^N z_k^2/4l_B^2} \\
&= \det\begin{vmatrix} 1 & 1 & \cdots \\ z_1 & z_2 & \cdots \\ (z_1)^2 & (z_2)^2 & \cdots \\ \vdots & \vdots & \vdots \end{vmatrix} e^{-\sum_k^N z_k^2/4l_B^2} \\
&= \prod_{i<j}^{N}(z_i - z_j)\; e^{-\sum_k^N z_k^2/4l_B^2},
\end{aligned} \tag{4.11}$$

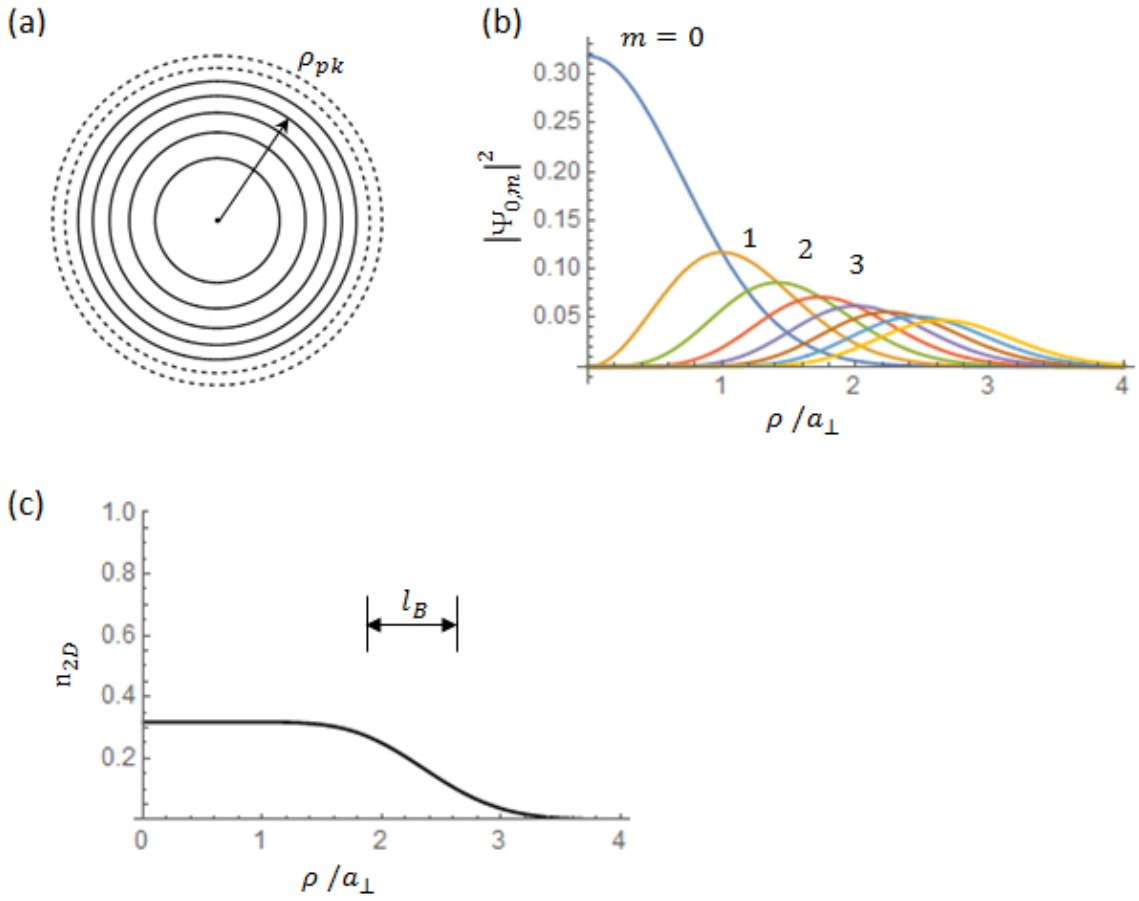

Figure 4.2: Degenerate states of the lowest Landau level. (a) Circular and quantized orbits of the states in the lowest Landau level. The mth state in the lowest Landau level has a ring shape with the peak position at $\rho_{pk} = \sqrt{m}a_\perp$. Solid lines represent the occupied states while the dashed lines represent the empty states. (b) Amplitude squared of the wavefunctions of the states in the lowest Landau levels. Each state has a single peak structure that spatially overlaps with neighboring states. The $1/e^2$ width of each peak is about l_B. (c) Density profile of the partially filled lowest Landau level with $n_{2D} = \sum_m |\psi_{0,m}|^2$. It is uniform near the center.

where $\mathcal{A}$ is the anti-symmetrization operator, N is the total number of electrons, and $z_j = x_j + iy_j = \rho_j e^{i\phi_j}$ is the complex coordinate in 2D for the jth electron.

The Landau levels are the foundation of the quantum Hall states. They have been used successfully for explaining the integer quantum Hall effect. However, to understand the fractional quantum Hall effect, the picture of Landau levels is inadequate and one needs to include the particle-particle interactions.

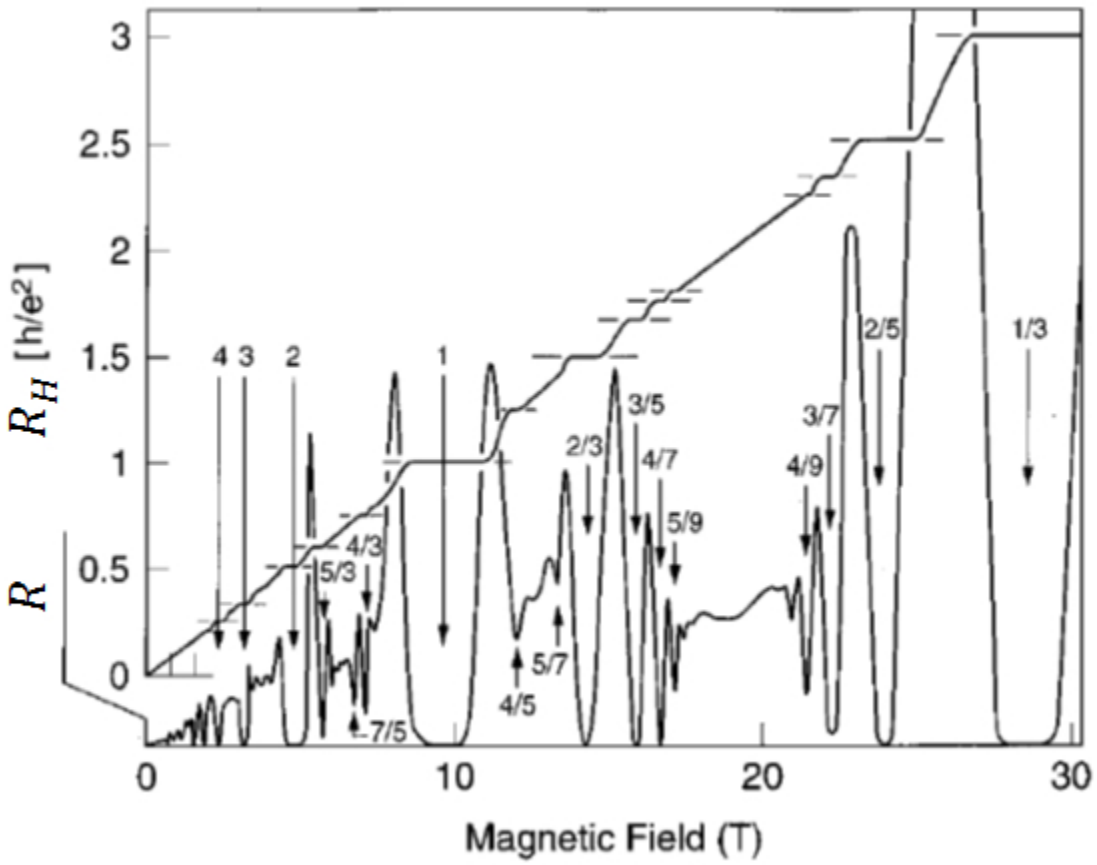

Figure 4.3: Integer and fractional quantum Hall effects (reproduced from [14]). The hallmark of these effects is the quantized Hall resistance, $R_H = \frac{h}{\nu e^2}$. The index $\nu = 1, 2, 3, \cdots$ (IQH effect) and $\nu = \frac{1}{3}, \frac{2}{5}, \frac{3}{7}, \cdots$ (FQH effect).

4.3 Integer and fractional quantum Hall effects

Quantum Hall effects are the manifestation of quantum Hall states through electron transport. To observe these effects, one needs a nearly ideal 2D electron system, which can be realized by confining charge carriers in a narrow potential well. Such a system was originally realized by using GaAs/AlGaAs heterostructures [14]. The carriers in such structures are free to move in a 2D plane, but their motion perpendicular to the plane is frozen by cooling the sample ($T \sim 1$mK) to the lowest energy level along this direction. As a consequence, a quasi-2D metal emerges with the carrier density ($n \sim 0.2 - 4 \times 10^{11}\text{cm}^{-2}$) [14]. Quantum Hall effects have also been observed in

other materials, for example, graphene [64].

Figure 4.3 shows the results of the measured normal resistance R and Hall resistance R_H for both the Integer quantum Hall (IQH) effect and the fractional quantum Hall (FQH) effect. The hallmark of these effects is the quantized Hall resistance,

$$R_H = \frac{h}{\nu e^2}, \tag{4.12}$$

where the index $\nu = 1, 2, 3, \cdots$ (IQH effect) and $\nu = \frac{1}{3}, \frac{2}{5}, \frac{3}{7}, \cdots$ (FQH effect). At each plateau of R_H, the normal resistance R vanishes. According to

$$R = \frac{V}{I} = \frac{E_y L_y}{j_y L_x} = \rho_{yy}(L_y/L_x) = \frac{\sigma_{xx}}{\sigma_{xx}\sigma_{yy} - \sigma_{xy}\sigma_{yx}} \frac{L_y}{L_x},$$

the conductivity $\sigma_{xx} = 0$, which means an insulator. On the other hand, the transverse conductivity $\sigma_{xy} \neq 0$, which means a conductor. It turns out that the insulating behavior comes from the bulk property of the material, while the conduction is due to edge states. Such kind of bizarre materials are called the topological insulators [13].

The IQH effect can be understood by considering the filling of Landau levels (see Fig. 4.4). For an electron gas trapped in a 2D uniform potential well, the density of states is homogenous in energy (see Fig. 4.4(b)). At zero temperature, the energy states below the Fermi energy E_F are occupied by electrons. When $B = 0$, there are no Landau levels. Thus the system is a normal conductor. As the magnetic field B is increased from zero, the system first shows the Hall effect. As the value of B increases, the energy spacing $\hbar\omega_c = \hbar eB/m_e c$ between Landau levels increases. As a result, energy gaps are opened at large values of B and Hall plateaus start to show up. At the same time, the density of states or the degeneracy of Landau levels, given by Eq. (4.8) increases linearly with respect to B. Therefore, fewer and fewer Landau levels are filled. The number of filled Landau levels corresponds to the index ν of the IQH effect and ν is called the filling factor. At each plateau, the Fermi energy lays in the energy gap, which means the system is an insulator based on the traditional classification. What exotic is that this traditional insulator can conduct electric current by edge states (Fig. 4.4(c)).

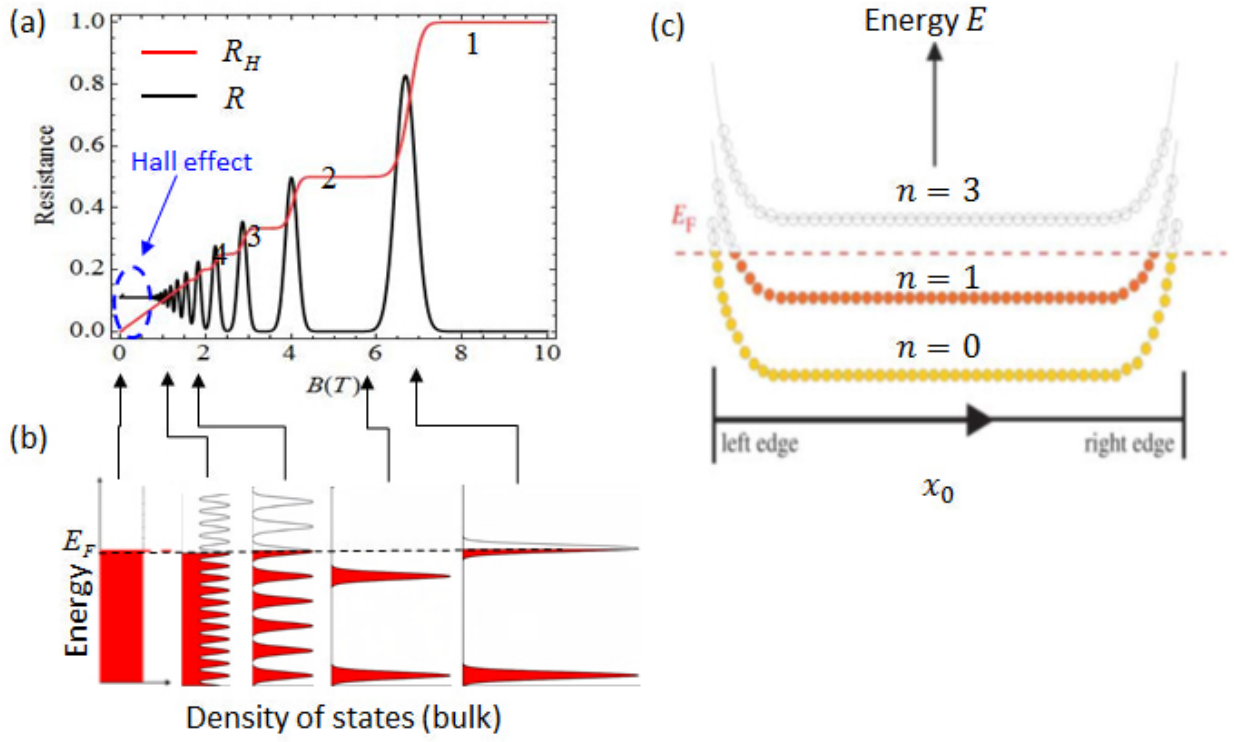

Figure 4.4: Understanding the IQH effect by filling Landau levels. (a) The integer quantum Hall effect at different values of B. (b) The correspondent picture of filling Landau levels. (a) & (b) are adapted from (http://en.wikipedia.org/wiki/Quantum_Hall_effect). Red shaded regime means occupied states below the Fermi energy (dashed line). The energy band is gapless at small values of B, where the classical Hall effect dominates. Once B is large enough, energy gaps are opened and Hall plateaus start to show up. Since the density of states or the degeneracy of Landau levels scales linearly with B, fewer and fewer Landau levels are occupied at higher B. (c) Ideal Landau levels for a device with boundaries (adapted from [65]). From Eq. (4.7), the location x_0 is quantized as represented by dots. The bulk states are insulating states, while the edge states contribute to the conduction.

The FQH effect has much richer physics than the IQH effect. The picture of filling Landau levels is not sufficient for describing the FQH effect and particle-particle interactions need to be considered. At fractional values of ν, the system has a partially filled Landau level. Furthermore, the plateau structure of R_H at the fractional ν means that an extra energy gap has opened in a Landau level, which is not predicted by the single-body physics and is due to the particle-particle interactions. The most exotic implication of the FQH effect is the existence of quasiparticles with fractional statistics and fractional charges. These composite quasiparticles are formed by attaching

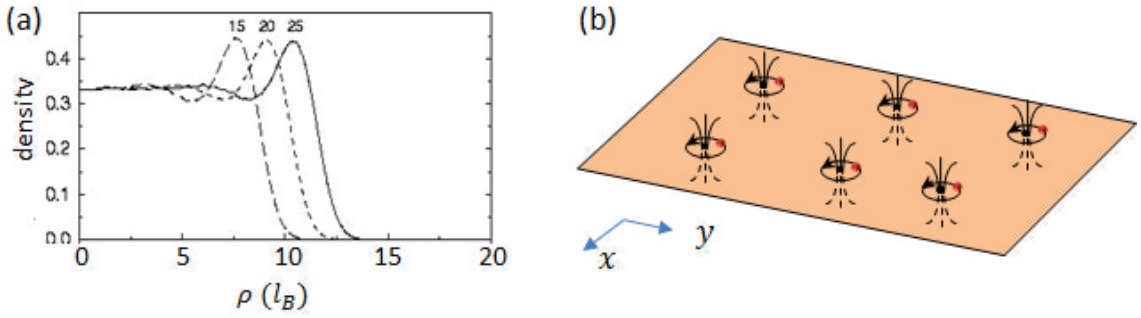

Figure 4.5: Understanding the FQH effect by the Laughlin's wavefunction. (a) Densities for 15, 20 and 25 particles in the $\nu = 1/3$ quantum Hall regime (adapted from [66]). The densities are obtained by classic Monte-Carlo calculations. Here ρ is the radius and l_B is the magnetic length. (b) A cartoon picture of the composite quasiparticles (reproduced from [67]). The electrons (red dots) are moving along cyclotron orbits around the magnetic flux $\Phi = 3\Phi_0$ (lines) at the orbital center.

magnetic fluxes to electrons and have become the underlying principle to describe the many-body states of the FQH effect.

In 1983, Laughlin proposed a many-body wave function for $\nu = 1/3$ that is known as Laughlin's wavefunction [61]

$$\Psi_{1/3} = \prod_{i<j}^{N}(z_i - z_j)^3 \exp\left(-\sum_{k}^{N}|z_k|^2/4l_B^2\right). \tag{4.13}$$

This wavefunction is similar to Eq. (4.11) except that it has a third-order zero $(z_i - z_j)^3$ for any pair of electrons. In addition, $\Psi_{1/3}$ describes a circular droplet of uniform density (see Fig. 4.5(a)). The exponent 3 in each factor expresses the attachment of three flux quanta to the position of each electron. It describes a composite quasiparticle that includes three flux quanta and one electron (see Fig. 4.5(b)). More generally, the exponent can be changed from 3 to q for the $\nu = 1/q$ ($q = odd$) state and it then characterizes an electron dressed by q flux quanta. Only odd q are allowed, since only they guarantee antisymmetry of this electron wave function. Based on the Laughlin's wavefuntion [61], it shows that an energy gap exists for the fractional quantum Hall state, which explains the plateau structure of R_H at the fractional values of ν.

4.4 Rapidly rotating atomic gases to quantum Hall regime: ideal cases

Electricallly neutral atoms in a magnetic field $\vec{B}$ do not feel any Lorentz force (for an electron, $F = -e\vec{v} \times \vec{B}$). But if we put atoms in a rotating frame, they feel the Coriolis force, $F = 2M\vec{v} \times \vec{\Omega}$, due to a rotating field $\vec{\Omega}$. The identical structure between the Lorenz force and Coriolis force indicates that we may be able to realize quantum Hall states by rotating ultracold gases of neutral atoms. In this section, I will discuss the connection between a rotating gas and quantum Hall states. Some experimental challenges will be reviewed in the next section.

4.4.1 Fermion case

Let me first discuss the case of rotating an ultracold Fermi gas. For a Fermi gas, the atoms follow Fermi statistics and thus they naturally form an incompressible fluid due to Pauli blocking. It requires that each quantum state can only be occupied by a single particle. This incompressibility is important for observing the plateaus of quantum Hall effects, because it allows electrons to be able to fill many Landau levels. To get the incompressibility for a bosonic gas, the repulsive particle-particle interactions are in need.

Considering a 2D rotating Fermi gas in a harmonic potential, the single-body Hamiltonian without interactions in the rotating frame is [62]

$$H + \Omega \hat{L}_z = \frac{\hat{\mathbf{p}}_\perp^2}{2M} + \frac{1}{2} M\omega_\perp^2 \rho^2 + \Omega \hat{L}_z, \tag{4.14}$$

where M is the atomic mass of an atom and $\omega_\perp$ is the trapping frequency of the harmonic potential. Assuming $\Omega = \omega_\perp$, Eq. (4.14) would have exactly the same form as Eq. (4.4). The eigenfunctions and eigenvalues of Eq. (4.14) are [62]

$$u_{n,m}(x,y) = \frac{e^{|w|^2/2} \partial_+^m \partial_-^n e^{-|w|^2}}{\sqrt{\pi a_\perp^2 n! m!}}, \tag{4.15}$$

$$\epsilon_{n,m} = \hbar(\omega_\perp + \Omega)n + \hbar(\omega_\perp - \Omega)m + \hbar\omega_\perp, \tag{4.16}$$

where the quantum number $n, m = 0, 1, 2 \cdots$ with $\hat{L}_z |u_{n,m}\rangle = \hbar(m-n)|u_{n,m}\rangle$, $w = (x+iy)/a_\perp$, $a_\perp = \sqrt{\hbar/M\omega_\perp}$, and $\partial_\pm = (a_\perp/2)(\partial_x \pm i\partial_y)$. $u_{n,m}$ is basically the same as $\psi_{n,m}$ in Eq. (4.10) but

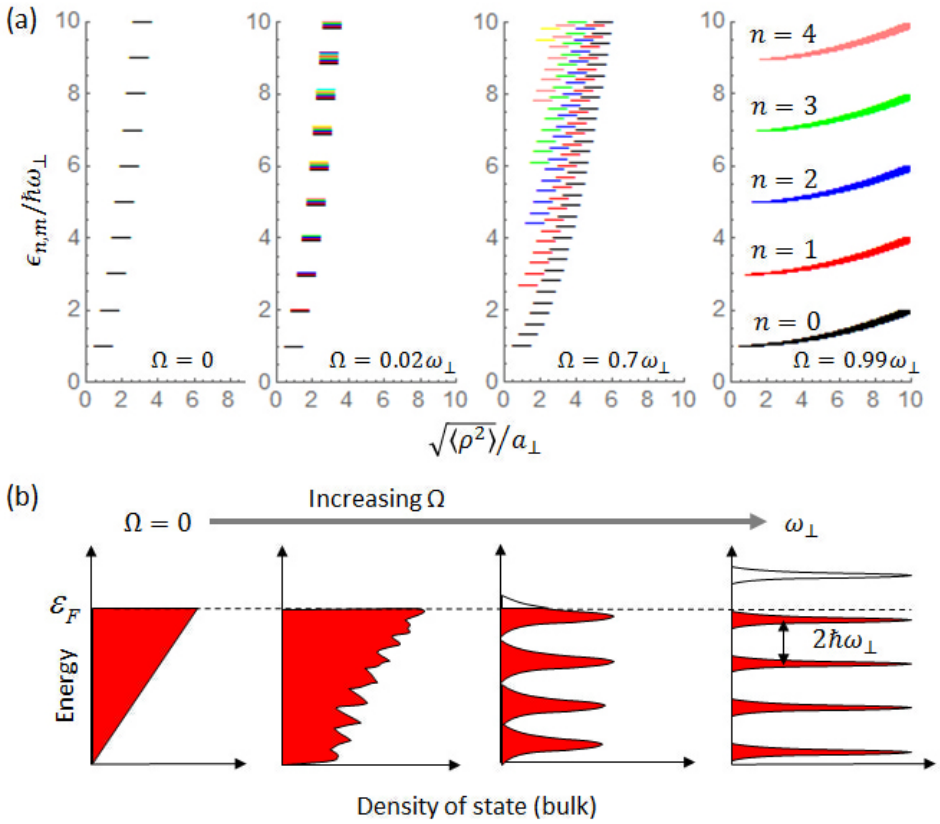

Figure 4.6: Realizing the IQH states by rapidly rotating a Fermi gas. (a) Shift of energy spectrum due to the rotation based on Eq. (4.16) and (4.17). When Ω approaches $\omega_\perp$, the Landau levels are formed and the size of the $u_{n,m}$ state is enlarged. (b)The gaps of energy bands are opened by rotating a gas. The density of states for a static gas is $\rho(\epsilon) = \epsilon/\hbar^2\omega_\perp^2$ (see Eq. (1.3)). Red shaded regime means occupied states below the Fermi energy (dashed line). The energy band is gapless at small values of Ω. Once Ω is large enough, energy gaps are opened. Different from the 2D electron system, the energy gap for a rotating gas is basically constant, independent of Ω. The number of occupied Landau levels can be tuned by varying the total number N of atoms (or ε_F).

with different $a_\perp$. The quantized orbit for the $u_{n,m}$ state can be seen by

$$\langle\rho^2\rangle_{n,m} = \langle u_{n,m}|\rho^2|u_{n,m}\rangle = (n+m+1)a_\perp^2, \tag{4.17}$$

which gives a good estimate of the area covered by the $u_{n,m}$ state. Here ρ is the radius. At the limit of $\Omega \to \omega_\perp$, Eq. (4.16) reduces to the Landau levels

$$E_n = (n+1/2)\hbar(2\omega_\perp), \tag{4.18}$$

with the energy spacing $2\hbar\omega_\perp$. Note that the rotating rate Ω cannot be bigger than the radial

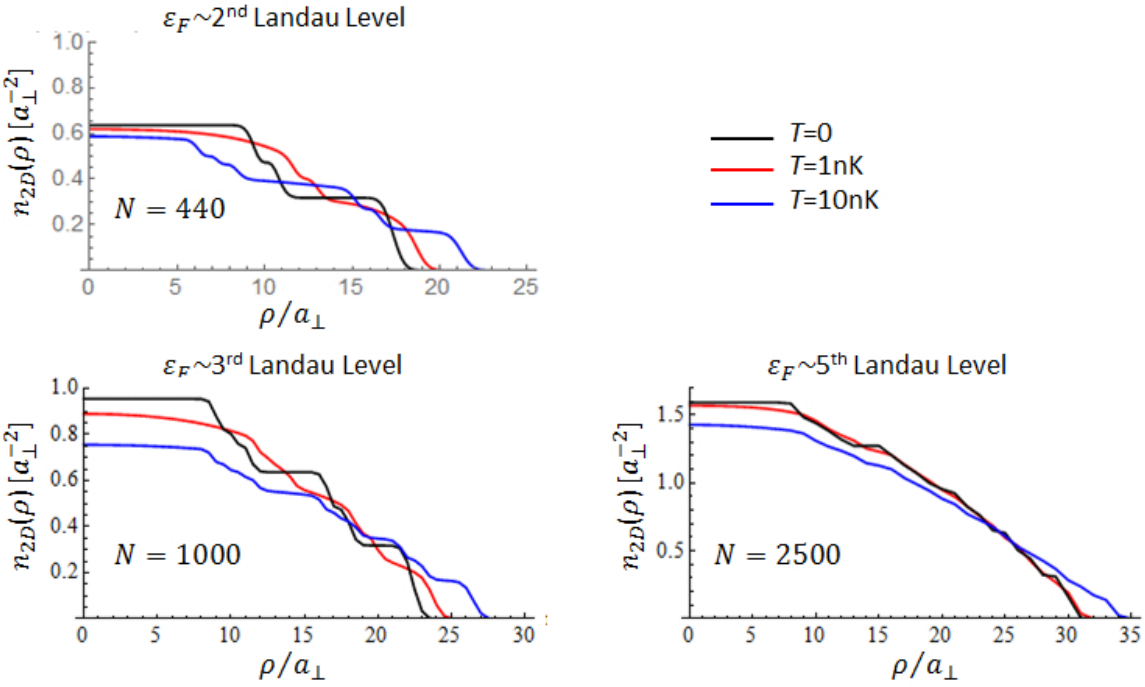

Figure 4.7: Density distribution of a rotating Fermi gas in the quantum Hall regime based on Eq. (4.19). Lower ε_F and lower T give more clear wedding cake structure. The oscillator length $a_\perp = \sqrt{\hbar/M\omega_\perp} = 2.5$ μm for a $2\pi \times 40$ Hz trap (M is the atomic mass of a ^{40}K atom) and $\Omega = 0.99\omega_\perp$.

trapping frequency $\omega_\perp$, because the centrifugal force gives effectively an anti-trapping potential.

For $\Omega < \omega_\perp$, the density of atoms at zero temperature is $n_{2D}(\rho) = \sum_{n,m} |u_{n,m}(\rho)|^2 \Theta(\varepsilon_F - \epsilon_{n,m})$ with $\Theta(x)$ being the step function and ε_F the Fermi energy. The total number $N = \sum_{n,m}(\varepsilon_F - \epsilon_{n,m})$. At finite temperature T, the density of atoms becomes

$$n_{2D}(\rho) = \sum_{n,m} |u_{n,m}(\rho)|^2 f(\epsilon_{n,m}), \tag{4.19}$$

with the Fermi-Dirac distribution function $f(\epsilon) = 1/(e^{(\epsilon-\varepsilon_F)/k_BT} + 1)$. Correspondingly, the total number is $N = \sum_{n,m} f(\epsilon_{n,m})$.

From Eq. (4.18), we can see that the integer quantum Hall states can be realized by rapidly rotating an ultracold Fermi gas (Fig. 4.6). The degeneracy of the Landau levels at the limit of $\Omega \to \omega_\perp$ is

$$D = \frac{2\omega_\perp}{\omega_\perp - \Omega}. \tag{4.20}$$

For the special case of $\Omega = \omega_\perp$, the atoms move in free space and there is no quantized energy levels. To detect the Landau levels or the integer quantum Hall states, one way is to look at the density distribution [62]. In the quantum Hall regime, the density distribution will show a "wedding cake" structure (see Fig. 4.7), which looks similar to the plateau structure of the IQH effect. For the given ε_F, the size of the nth Landau level can be estimated by $\rho_n = a_\perp\sqrt{n + m_n^* + 1}$ with the highest angular momentum state in the nth Landau level, $m_n^* = \mathrm{Int}[\frac{\varepsilon_F/\hbar - \omega_\perp - (\omega_\perp + \Omega)n}{\omega_\perp - \Omega}]$. When $\Omega \to \omega_\perp$, we have the size of the nth Landau level as

$$\rho_n = a_\perp\sqrt{\frac{\varepsilon_F/\hbar - (2n+1)\Omega}{\omega_\perp - \Omega}}, \tag{4.21}$$

with the oscillator length $a_\perp = \sqrt{\hbar/M\omega_\perp} = 2.5$um for a $2\pi \times 40$ Hz trap (M is the atomic mass of a ^{40}K atom).

4.4.2 Boson case

The Eqs. (4.15) and (4.16) also work for a bosonic gas. The only difference from the fermionic case is the compressibility of a bosonic gas. Due to the Bose-Einstein statistics, a single state can be occupied by infinite number of bosonic atoms, which makes it hard to get a small filling factor ν. In the past, the TOP trap experiment at JILA rotated a ^{87}Rb BEC into the lowest Landau level, but the filling factor was about 100. That is, there were 100 atoms occupying each $u_{0,m}$ state. Assuming we have a Feshbach resonance (see Sec. 1.3), we can tune the particle-particle interaction to be repulsive. In this case, the atoms would repel each other and eventually form an incompressible fluid. By tuning the interaction strength, one can tune the number of occupied Landau levels. Interactions of bosons potentially make them to be a fermion-like liquid [68, 69, 70].

4.5 Technical challenges

In the last decade, the technique of rotating ultracold gases has been developed for the original goal of studying the superfluid property of a BEC [15]. However, due to technical challenges, none of the existing schemes have been sufficient for observing quantum Hall states. In the following,

I discuss these challenges and in the next chapter I present an new apparatus for potentially overcoming these challenges.

4.5.1 An extremely smooth and harmonic optical trap

An ultracold atom experiment generally uses a harmonic trapping potential to confine the gas. To get fast rotation, the trap geometry needs to be as round as possible in the rotating plane, which is relatively easy to achieve with careful design. Secondly, higher order anharmonic terms of the trapping potential could limit the rotation rate. This can be seen from the following potential (see Sec. 5.3)

$$U(x, y) = U_0 + A_2(x^2 + y^2) + A_3 y^3.$$

The y^3 terms can break the circular symmetry and slow down rotation. Thirdly, the smoothness of the potential is very important for a long-lived rotating gas. In particular, once the rotation rate is close to the trapping frequency $\omega_\perp$, any small roughness will have a big effect in damping rotation. In order to get fast rotation, e.g. $\Omega \sim 0.99\omega_\perp$, the roughness need to be reduced below 1%.

The harmonic trapping potential could be achieved with a magnetic trap or with an optical trap. With a magnetic trap, it is easier to satisfy the conditions of smoothness and harmonicity. However, a magnetic trap makes it very difficult to use a magnetic Feshbach resonance to tune the particle-particle interactions, which is very important for reaching the quantum Hall regime. In comparison, an optical trap is an ideal option for accessing a magnetic Feshbach resonance, but is difficult to get as smooth and harmonic as a magnetic trap.

4.5.2 Rapid rotation close to 0.99 of trapping frequency

There are two main ways of rapidly rotating ultracold gases that have been demonstrated. The first way is to use a blue-detuned laser beam to stir the trapped gas. This way has been used by the MIT group for rotating a ^{23}Na BEC [71] and a ^{6}Li degenerate Fermi gas [72], and by the Paris group for rotating a ^{87}Rb BEC [73]. However, because the center-of-mass motion of the harmonically trapped atom cloud is dynamically unstable as $\Omega \to \omega_\perp$ [74], the stirring method is

not fully appropriate for approaching the rapidly-rotating regime. The instability of center-of-mass motion limits how close to $\omega_\perp$ the rotating rate Ω can be. The second way of rapidly rotating ultracold gases is to use a deformable trap. The gas is stirred by deforming the trap to an elliptical shape, then jumping the major axis by 45 degree to impart angular momentum to the atoms, and then restoring the trap geometry to be round. After this stirring process, the rotation rate of gas is generally up to about $0.4\omega_\perp$. To further speed up rotation, a special evaporation process, called spin-up evaporation, is used. The basic idea is to evaporate away atoms with lower angular momentum so that the averaged angular momentum per atom is increased. As a result, the rotation rate of the atom cloud is increased according to $L_z = m\Omega^2\rho$. This way works great as demonstrated by the JILA TOP trap experiment [75]. They also demonstrated a ^{87}Rb BEC that was rotated so fast that all Rb atoms were in the lowest Landau level [76]. In the next chapter, we present our scheme, which uses a similar spin-up evaporation technique to speed up the rotation of a gas.

4.5.3 Detecting local density by a quantum gas microscope

The wedding cake structure is an important feature of quantum Hall states. The plateau size is about $a_\perp = 2.5$ μm. The atom number per unit area of $\pi a_\perp^2$ is only a few atoms. To detect such a small feature, one needs a quantum gas microscope [77, 78, 79, 80, 81, 82, 83].

4.6 Other proposals

Beyond rotating gases, there are other proposals for simulating quantum Hall states using ultracold atoms. These proposals include (i) rotating gases trapped in an optical lattice [84]; (ii) synthetic fields created by Raman beam coupling [85, 86, 87]; and (iii) laser assisted tunneling in a tilted optical lattice [88, 89].

Chapter 5

A novel all-optical trap for rapidly rotating gases

In this chapter, a new apparatus for rotating ultracold gases is introduced, and its optimization procedures are described. Some important features of this new apparatus include an all-optical trapping potential, a controllable potential geometry, and a good imaging system. To characterize the apparatus, we used a ^{87}Rb BEC as a sensor to round out the trapping potential and further to measure the roughness of potential. Ultimately, the apparatus was tested by rotating the ^{87}Rb BEC and quantized vortices were detected. By counting vortices, we can estimate how fast the atomic gas is rotated. In particular, we used the rotating Rb BEC to test a spin-up evaporation technique, which is a crucial part of our strategy for achieving rapid rotation.

5.1 A new apparatus for rotating gases

Fig. 5.1 shows the schematics of the new apparatus. It consists of two independent laser beams that form an optical trapping potential. The first beam is a horizontally propagating sheet beam that is designed to provide only vertical confinement for the atoms. The second beam is a vertically propagating round beam, which confines the atoms horizontally. Both beams have the same wavelength (1090nm) and generate a far red-detuned optical dipole trap. The linewidth of the lasers is 1 nm, which reduces the interference of the laser beams. An important feature of the apparatus is that the pointing direction of the vertical beam is controlled by a dual-axis acousto-optic modulator (AOM). By using the AOM, we can change the position of the vertical beam, which makes it possible to create a time-averaged or painted trapping potential.

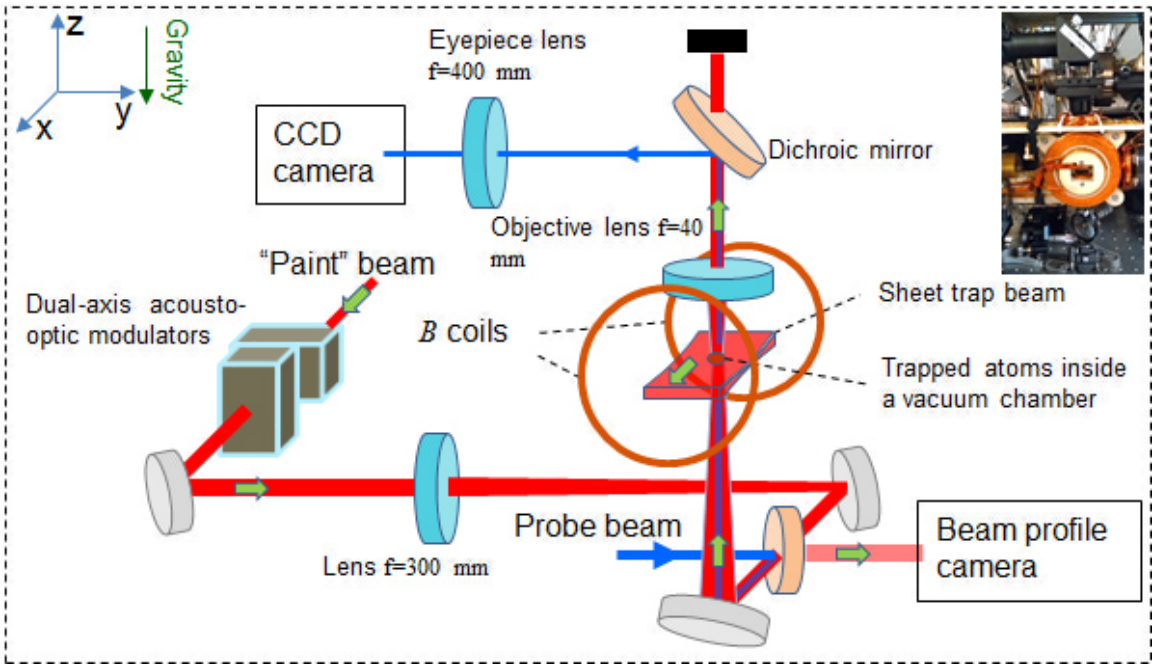

Figure 5.1: A new apparatus for rotating ultracold gases. It consists of two main laser beams. The first beam is a horizontally propagating sheet beam with $1/e^2$ beam waist of 1 mm$\times$30 μm, which is designed to provide only vertical confinement for the atoms. The second beam is a vertically propagating round beam, which confines the atoms horizontally. The B coils are used for accessing a Feshbach resonance. An imaging setup is indicated by the blue line.

An AOM device can change the steering of a laser beam by imparting a phonon momentum $\vec{k}$ to a photon that passes through the AOM [90]. Here phonons refer to the acoustic vibration mode of the AOM crystal driven by an external RF signal with frequency ν. Photons come from a laser beam that passes through the AOM. Denoting the initial momentum of the photon by $\vec{p}$, we get the final momentum of the photon as $\vec{p}+\vec{k}$. Since the initial momentum $\vec{p}$ is generally perpendicular to the phonon momentum $\vec{k}$, the laser beam deviates from its initial direction after passing through the AOM. The deviation amplitude depends on the angle between $\vec{p}$ and $\vec{p}+\vec{k}$ and the magnitude of $\vec{k}$ is related to ν as, $|\vec{k}| = h\nu/c_s$ (h is the Planck's constant and c_s is the speed of sound). Therefore we can change the propagating direction of a laser beam by changing the phonon frequency ν. In the experiment, we use AOMs that use a longitudinal acoustic mode, which gives a rise time of 150 ns/mm(beam diameter). The AOMs we used are from Gooch & Housego with

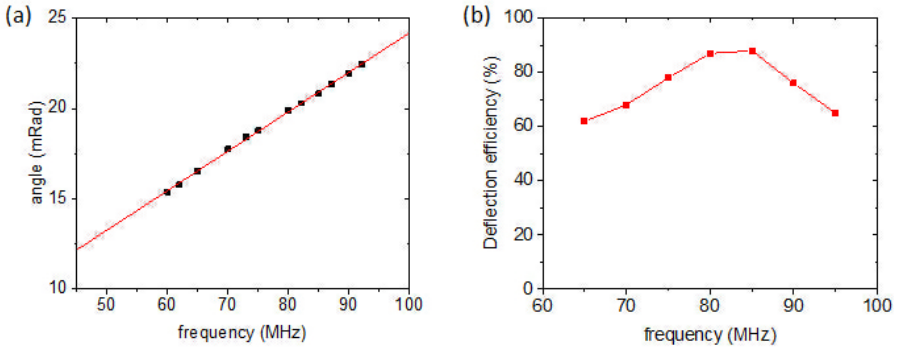

Figure 5.2: Control of laser beam pointing using an AOM. (a) Deflection angle versus RF frequncy. The central frequency of the AOM is 80MHz. The deflection angle is linearly proportional to the RF frequency. The line shows a linear fit with the slope of 0.213 mRad/MHz. (b) The deflection efficiency of the AOM vs. the RF frequency, using 33 dBm of RF power into the AOM.

the model number (46080-2-1.06-LTD). The AOMs have an aperture diameter of 2 mm and an operating RF frequency ν tunable from 65 to 95 MHz. The dependence of the deflection angle on the driving RF frequency is shown in Fig. 5.2(a). Fig. 5.2(b) shows the corresponding variations of the deflection efficiency on the RF frequency. The deflection angle is determined by measuring the transverse separation of the deflected and undeflected beams at a distance of 30 cm from the AOM. The deflection efficiency is the measured power in the deflected beam divided by the input beam power.

5.1.1 A painted trapping potential

To make a painted trapping potential in the x-y plane, we use two AOMs oriented to give perpendicular deflections to change the trap position in the x-y plane. The driving electronics for the AOMs are controlled by a computer, which allows us to program an arbitrary trajectory of the beam position within a period $\mathcal{T}$. Because the period $\mathcal{T}$ is very short compared to the time-averaged trapping period, the atoms feel a time-averaged trapping potential rather than the instantaneous potential. For a static optical dipole trap, the trapping potential is described by $U(x,y) = U_0 \exp\{-2[(x-x_0)^2 + (y-y_0)^2]/w_0^2\}$ with the center position at (x_0, y_0). After turning

on the painting, we can express the time-averaged trapping potential generally as

$$U_{\text{paint}}(x,y) = \frac{U_0}{\mathcal{T}} \int_0^{\mathcal{T}} dt \exp\left[-2\frac{(x-x_c(t))^2 + (y-y_c(t))^2}{w_0^2}\right], \tag{5.1}$$

with a time-dependent center position $(x_c(t), y_c(t))$.

We want our time-averaged trapping potential to be axially symmetric around the z axis. In the following discussions, it is convenient to work with the polar coordinates $\{x,y\} \to \{\rho,\phi\}$. Thus we denote the center position of the instantaneous trapping potential by $\{\rho_c(t), \phi_c(t)\}$. To simplify the mathematical derivation, we assign two different time scales, $\mathcal{T}$ and $\mathcal{T}_1$, for $\rho_c(t)$ and $\phi_c(t)$ respectively with the condition of $\mathcal{T} \gg \mathcal{T}_1$. We then treat ρ_c as fixed when we discuss $\phi_c(t)$ at the fast time scale. This is a reminiscent of a similar treatment that is often used in the description of the motion of atomic nulei and electrons, known as Born-Oppenheimer approximation. To maintain the axial symmetry, the trajectory of the polar angle $\phi_c(t)$ needs to follow a circle, i.e., $\phi_c(t) = 2\pi t/\mathcal{T}_1$. We then have $x_c(t) = \rho_c \cos(2\pi t/\mathcal{T}_1)$ and $y_c(t) = \rho_c \sin(2\pi t/\mathcal{T}_1)$. By integrating the fast time scale over the period of $\mathcal{T}_1$, we get the time-averaged trapping potential based on Eq. (5.1) as

$$U_{\text{paint}}(\rho) = \frac{U_0}{\mathcal{T}} e^{-2\rho^2/w_0^2} \int_0^{\mathcal{T}} dt_s e^{-2\rho_c^2(t_s)/w_0^2} J_0\left(i\frac{4\rho\rho_c(t_s)}{w_0^2}\right), \tag{5.2}$$

where the only time-dependent quantity left is $\rho_c(t_s)$ and J_0 is the zeroth order of Bessel's function $J_0(x) = J_0(-x) = \frac{1}{\pi}\int_0^\pi e^{ix\cos\theta} d\theta = \sum_{k=0}^{\infty} (-1)^k (x^2/4)^k/(k!)^2$. The above equation is ϕ-independent, as expected for axial symmetry. The geometry of the time-averaged trapping potential is then determined by the specific function form of $\rho_c(t_s)$. In the following, I give functional forms of $\rho_c(t_s)$ for a ring trap, a homogeneous trap, and a harmonic trap.

A ring trap The simplest functional form of $\rho_c(t_s) = C$, where C is a constant, gives a ring trap with the time-averaged trapping potential given by

$$U_{\text{paint}}(\rho) = U_0 e^{-2(\rho^2+C^2)/w_0^2} J_0\left(i\frac{4\rho\cdot C}{w_0^2}\right).$$

The resultant trapping potential is shown in Fig. 5.3(a).

A uniform trap It is impossible to get a uniform trapping potential over all space by painting. Instead I focus on getting a uniform trapping potential around the center regime as

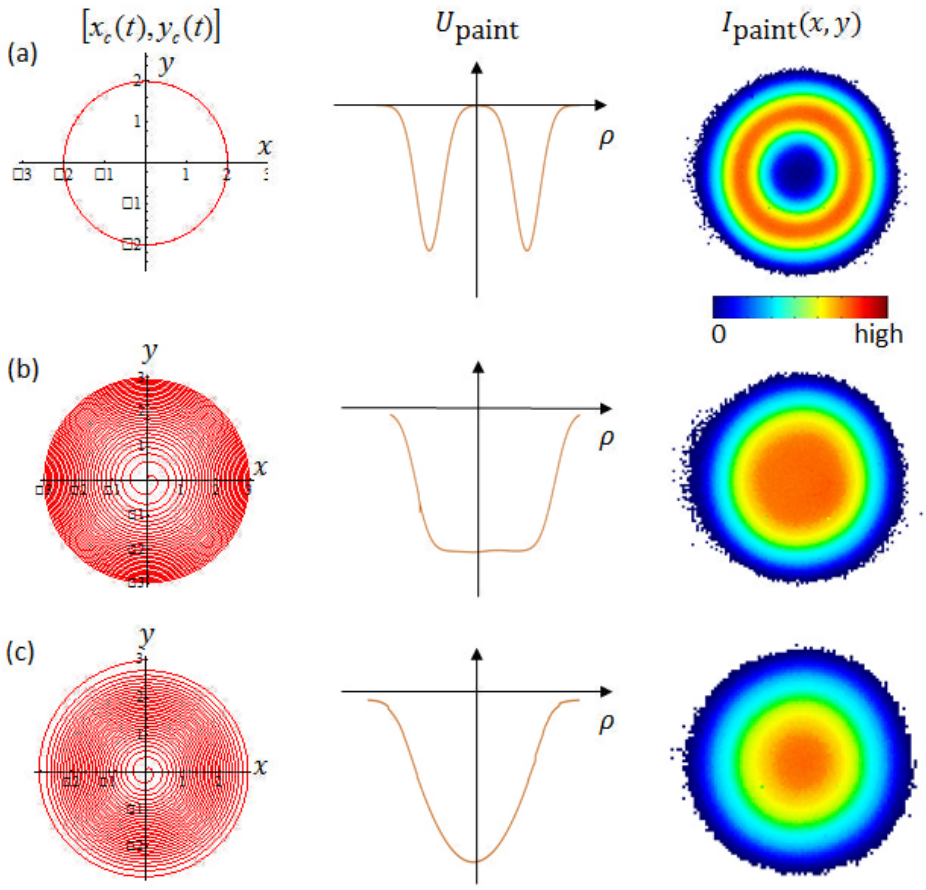

Figure 5.3: Time-averaged trapping potentials. The left is the trajectory of the trap center. The middle is the calculated potential profile. The right is the measured time-averaged laser intensity. (a) A ring trap. The functional form for the painted beam is $\rho_c(t) = 2w_0$. (b) A uniform trap. Here, $\rho_c^{\max}$ is set to be $3w_0$. At the center regime with $\rho < \rho_c^{\max}$, there is a uniform trapping potential. (c) A harmonic trap. b is set to be 1 and $\rho_c^{\max}$ is set to be $3w_0$. The center regime with $\rho < \rho_c^{\max}$ shows a harmonic trapping potential.

shown in Fig. 5.3(b). For this goal, $\rho_c(t_s) = \rho_c^{\max}\sqrt{t_s/\mathcal{T}}$, which gives

$$U_{\text{paint}}(\rho) = \frac{1}{2}U_0\left(\frac{w_0}{\rho_c^{\max}}\right)^2,$$

for $\rho < \rho_c^{\max}$ and $\rho_c^{\max} \geq 3w_0$. The analytical derivation of the above equation can be found in Append. B. From the above equation, we see that the bigger the painted size $\rho_c^{\max}$ is, the smaller the trap depth is.

A harmonic trap For a harmonic trap, I found that

$$\rho_c(t_s) = \rho_c^{\max} \cdot \sqrt{\frac{b+1-\sqrt{(b+1)^2-4bt_s/\mathcal{T}}}{2b}}, \tag{5.3}$$

with the dimensionless parameter $0 \leq b \leq 1$. This function satisfies $\rho_c(t_s = 0) = 0$ and $\rho_c(t_s = \mathcal{T}) = \rho_c^{\max}$. Eq. (5.3) is equivalent to

$$t_s = \mathcal{T} \cdot \left[(b+1) \cdot \left(\frac{\rho_c}{\rho_c^{\max}} \right)^2 - b \cdot \left(\frac{\rho_c}{\rho_c^{\max}} \right)^4 \right].$$

Taking them into Eq. (5.2), we have

$$\begin{aligned} U_{\text{paint}}(\rho) &= \frac{U_0 w_0^2}{2(\rho_c^{\max})^2} \left[b+1-b\left(\frac{w_0}{\rho_c^{\max}} \right)^2 \right] - \frac{U_0 w_0^2 b}{(\rho_c^{\max})^4} \rho^2, \\ &= \frac{U_0 w_0^2}{2(\rho_c^{\max})^2} - \frac{1}{4} m\omega_\rho^2 \left[(\rho_c^{\max})^2 - \omega_\rho^2 \right] + \frac{1}{2} m\omega_\rho^2 \rho^2, \end{aligned}$$

for $\rho < \rho_c^{\max}$ and $\rho_c^{\max} \geq 3w_0$. Here the trapping frequency ω_ρ depends on the b with a relation of $\frac{1}{2} m\omega_\rho^2 = -U_0 w_0^2 b/(\rho_c^{\max})^4$. The analytical derivation of the above equation can be found in Append. B. The time-averaged trap depth is given by

$$U_{\text{depth}} = \frac{U_0 w_0^2}{2(\rho_c^{\max})^2} \left[b+1-b\left(\frac{w_0}{\rho_c^{\max}} \right)^2 \right].$$

Both the time-averaged trapping frequency and trap depth depend on not only $\rho_c^{\max}$ but also b. Fig. 5.3(c) shows a time-averaged harmonic trapping potential.

To perform the painting trajectories discussed above in experiment, we use the electronics shown in Fig. 5.4 to drive two AOMs. Two AOMs are oriented 90 degree from each other so that they can independently control the x and y positions of a laser beam. Each AOM is driven directly by a voltage-controlled oscillator (VCO), whose output frequency is determined by an externally controlled voltage. We can change this external control voltage to change the position of the laser beam. For getting a ring trap, I used a sine wave signal and a cosine wave signal for the external control voltages to drive the two VCOs. The two control voltages are obtained from a direct digital synthesizer (DDS) and share the same time-independent amplitude, which is controlled by two variable gain amplifiers (VGAs). Based on the ring trap, a uniform trapping potential or a

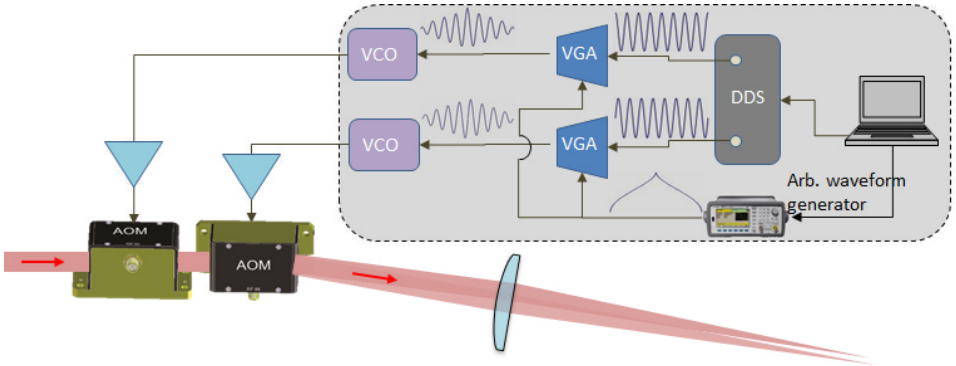

Figure 5.4: Electronics for driving AOMs. A dual-axis AOM consists of two AOMs, whose orientations are perpendicular to each other. The driving frequency of the AOMs is centered at 80 MHz and is provided by two voltage-controlled oscillators (VCOs). A two-channel direct digital synthesizer (DDS, AD9959-eval) combined with two variable gain amplifiers (VGAs, AD8330-eval) are used to control VCOs. In addition, the VGAs are controlled by an arbitrary-wave function generator for painting $\rho_c(t_s)$ from Eq. (5.3).

harmonic trapping potential can be obtained by setting a time-dependent amplitude for the sine and cosine wave signals. This time-dependent amplitude needs to follow the corresponding functional form of $\rho_c(t_s)$ discussed above.

5.1.2 A good imaging setup

To optimize our apparatus, we need an imaging system to be capable of resolving our BEC in trap and resolving vortices after expansion. As shown in Fig. 5.5, I used a 1/2 inch diameter objective lens with a numerical aperature ($N.A.$) of 0.12. Due to our limited optical access, it is challenging to increase the $N.A.$ of this lens. Our objective lens has a diffraction-limited resolution of $D = 0.61\lambda/N.A. = 3.9$ μm (Rayleigh criterion). The depth of field is $DOF = \lambda/N.A.^2 = 54$ μm. To focus the imaging system, we fixed the position of camera about 400 mm away from a second, "eyepiece" lens with a focal length of $f = 400$ mm and moved the objective lens closer to or farther from the atoms using a translation stage. The optimal position of the objective lens was found by using the lensing effect.

A good introduction to the lensing effect can be found in Matthews' thesis [91]. A trapped

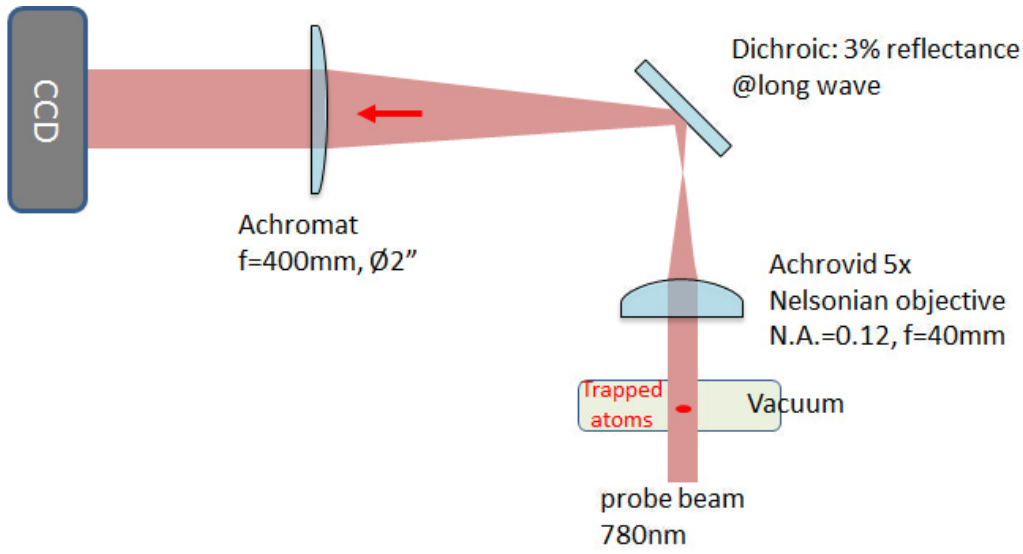

Figure 5.5: A good imaging setup. Due to our limited optical access, I chose an 1/2” diameter objective lens with N.A.=0.12. The objective lens has a diffraction-limited resolution of $D = 0.61\lambda/N.A. = 3.9$ μm (Rayleigh criterion). The depth of field is $DOF = \lambda/N.A.^2 = 54$ μm.

atomic gas is basically an optical medium and behaves like a lens when a laser beam passes through it. The index of refraction of such an optical material depends on the frequency detuning of the laser beam from the atomic resonance. For blue-detuned light, the index is smaller than 1 and thus the trapped atomic gas with higher optical thickness in the center behaves as a concave lens. For red-detuned light, the index is bigger than 1 and thus the trapped atomic gas with higher optical thickness in the center behaves as a convex lens. For resonant light, the index equals to 1 and no lensing effect occurs. When we image an atomic gas, an out-of-focus imaging system distorts the images differently for different detunings. As shown in Fig. 5.6(a), for the blue-detuned case, if the focal plane of the imaging system is before (location A) the object plane, there is excess light in the center captured by the camera, which results in a negative dip in the measured optical depth; if the focal plane of the imaging system is past (location B) the object plane, there are more light on the edge of the cloud captured by the camera, which results in negative edge in the measured optical depth. Similar but reverse lensing effects occur for the red-detuned case (see effects at locations C and D). The lensing effect provides an accurate way for us to find the position of the object plane.

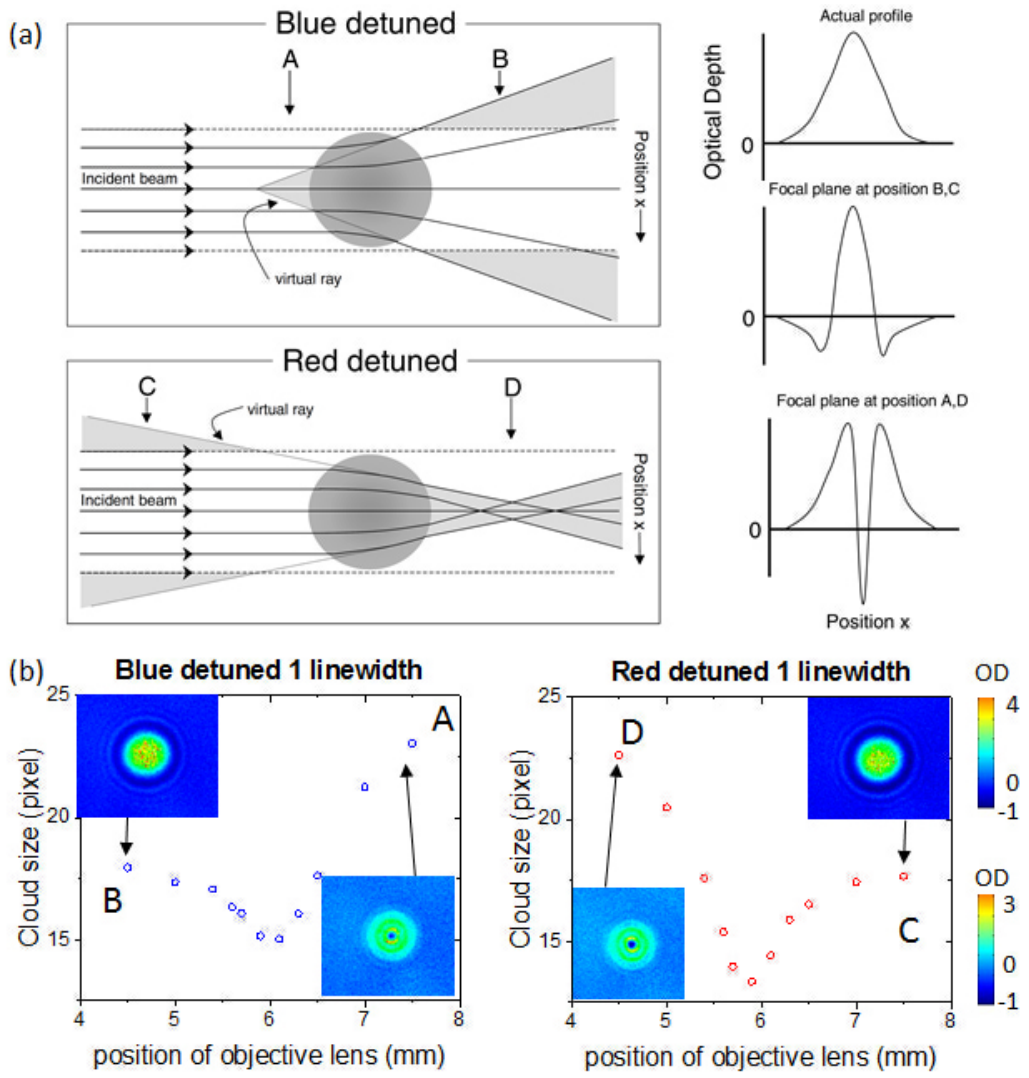

Figure 5.6: The lensing effect when focusing our imaging system. (a) Illustration of the lensing effect when a laser beam passes through a trapped atomic gas (reproduced from Matthews' thesis [91]). The optical index of the trapped atomic gas is less than 1 for the blue-detuned laser light and therefore the trapped atomic gas behaves as a concave lens. On the other hand, the optical index is bigger than 1 for the red-detuned light and the trapped atomic gas behaves as a convex lens. (b) Measured lensing effect in our system. The position of the objective lens is measured from an arbitrary fixed point: lower values are farther from the atoms. The cloud size is from a gaussian fit and increases on both sides because of the bad fittings caused by the saturated OD for B,C and the dip structure for A,D.

Fig. 5.6(b) shows the lensing effect observed when we were focused our imaging system. We imaged a dense Rb thermal gas (with the peak optical depth $pkOD = 130$) in trap while moving the objective lens to different locations. The cloud size in the images was obtained by

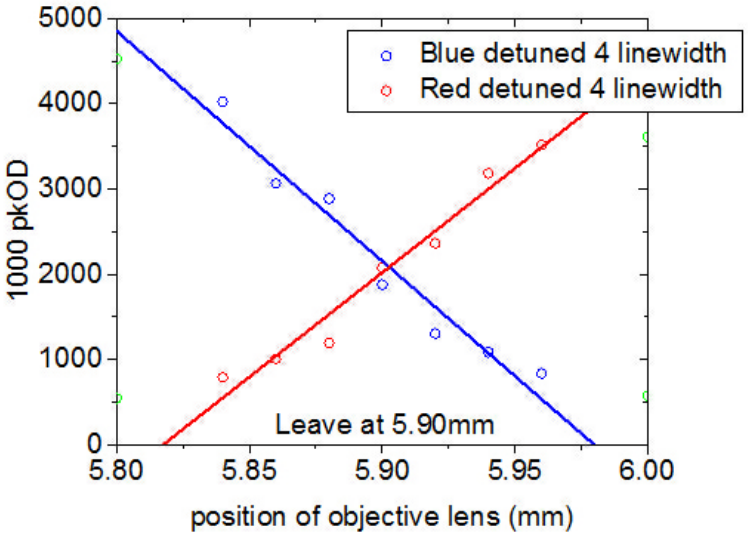

Figure 5.7: Using the lensing effect to focus our imaging system. The crossing point of blue-detuned and red-detuned lines gives the optimal position.

fitting to a gaussian distribution. From the optical depth images, the lensing effect appears exactly as we expect. The imaging system was focused by comparing the *pkOD* for blue-detuning and red-detuning, with the optimal position given by the crossing point (see Fig. 5.7).

5.2 Optimizing the trap roundness

To get a rapidly rotating gas, the trapping potential needs to be axially symmetric. That means the trapping frequencies along x and y need to be the same. An effective way to measure the trapping frequencies is to look at the atoms sloshing in the trap. We use a non-destructive imaging technique, called phase contrast imaging to monitor the slosh of a BEC to measure the trapping frequencies.

5.2.1 Phase contrast imaging

Phase contrast imaging is a non-destructive imaging technique. It is generally used in the ultracold atoms to image a BEC many times before destructing the BEC. We use it to monitor the slosh of a BEC to measure the trapping frequencies. Right after passing through a BEC, the

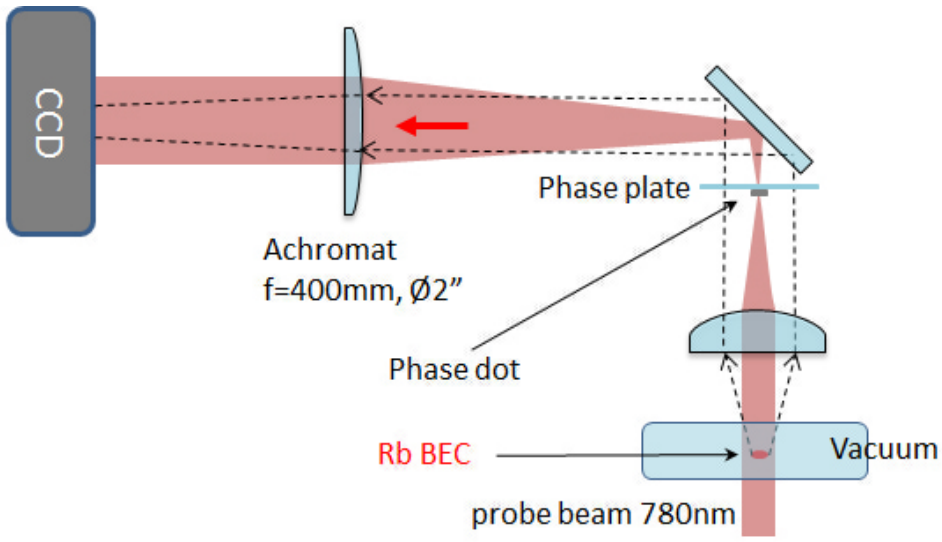

Figure 5.8: Phase contrast imaging setup. The dashed lines represent the scattered light by a BEC. A phase plate with a 510 nm thick and 45 μm diameter phase dot (black mark) is placed at the back focus of the objective lens. The phase dot causes a $\pi/2$ phase shift in probe light relative to the scattered light.

transverse electric field of the probe beam can be written as $E(x,t) = E_0 \cos(\omega t + \phi(x))$ with x being the spatial coordinate along the transverse direction and $\phi(x)$ being the x dependent phase shift caused by the BEC. For a small $\phi(x)$, the electric field can be written as [Matthews' thesis [91]]

$$E(x,t) = E_0 \cos(\omega t) + E_0 \sin(\omega t)\phi(x),$$

in which the first term comes from the unscattered light and the second term comes from the light scattered by the BEC. The probe light intensity, $I(x) \propto \overline{|E(x,t)|^2}$ (the bar means the time average), won't generate any phase signal. But if we shift the second term by a phase of $\pi/2$, we get $E(x,t) = E_0 \cos(\omega t) + E_0 \cos(\omega t)\phi(x)$ and the probe light intensity becomes

$$I(x) = I_0(1 + 2\phi(x)), \tag{5.4}$$

where the higher order term of $\phi(x)^2$ is omitted. (The technique for applying this $\pi/2$ phase shift is discussed in the next paragraph.) When imaging atoms in the experiment, we have three frames: a shadow frame that shows the probe beam after passing through the atoms (denoted by I_S), a light

frame that shows the probe beam (no atoms) ($I_{\rm L}$), and a dark frame that shows only background light (no probe beam) ($I_{\rm D}$). The final signal for phase contrast imaging is obtained using

$$S(x,y) = \left| \frac{I_{\rm S} - I_{\rm D}}{I_{\rm L} - I_{\rm D}} - 1 \right| = 2\left|\phi(x,y)\right|,$$

which is different from the usual absorption imaging where the optical depth is obtained using, $OD(x,y) = \ln\left(\frac{I_{\rm S}-I_{\rm D}}{I_{\rm L}-I_{\rm D}}\right)$. The signal ϕ is negative for a blue-detuned probe beam and positive for a red-detuned probe beam [Haljan's [92]]. The nondestructive property of the phase contrast imaging can be seen from the relationship, $\phi \propto 1/\delta$ and the photon scattering rate $\Gamma \propto 1/\delta^2$ with δ being the detuning. Therefore, at large detuning ($\delta \sim$ 1GHz) with a BEC, the phase shift ϕ can be detectable when Γ is negligible, which results in little atom loss in trap due to the scattering of probe photons. Additionally, for a large detuning $\delta \gg \gamma$, absorption is related to the phase shift by (see Eq. (4.11) of Matthews' thesis [91])

$$OD \propto \left|\frac{\gamma}{\delta}\phi\right|,$$

where γ is the natural line width. There is no detectable absorption at a large detuning. An example of our phase contrast imaging can be found in Fig. 5.12.

To get a $\pi/2$ phase shift only on the scattered light, a piece of glass with a 510 nm thick and 45 μm diameter phase dot is put at the back focus of the objective lens as illustrated in Fig. 5.8. (The phase dot was made by depositing MgF_2 on the glass by the JILA machining shop.) This phase plate gives a $\pi/2$ phase difference between the probe light, which is focused on the phase dot and then the glass, and the scattered light, most of which passes through the glass only. Thus the phase difference is

$$k_n d - k_0 d = k_0(n-1)d = \pi/2,$$

from which we get the thickness d of the phase dot. Here k_n is the wave vector of the light in the medium ($k_n = 2\pi n/\lambda$) and k_0 is the wave vector of the light in the vacuum ($k_0 = 2\pi/\lambda$). The index of MgF_2 is $n = 1.38$ and $\lambda = 780$ nm. At the position of the phase plate, the size of the phase dot need to be larger than the size of the focused probe beam and much smaller than the size of the light scattered by the BEC.

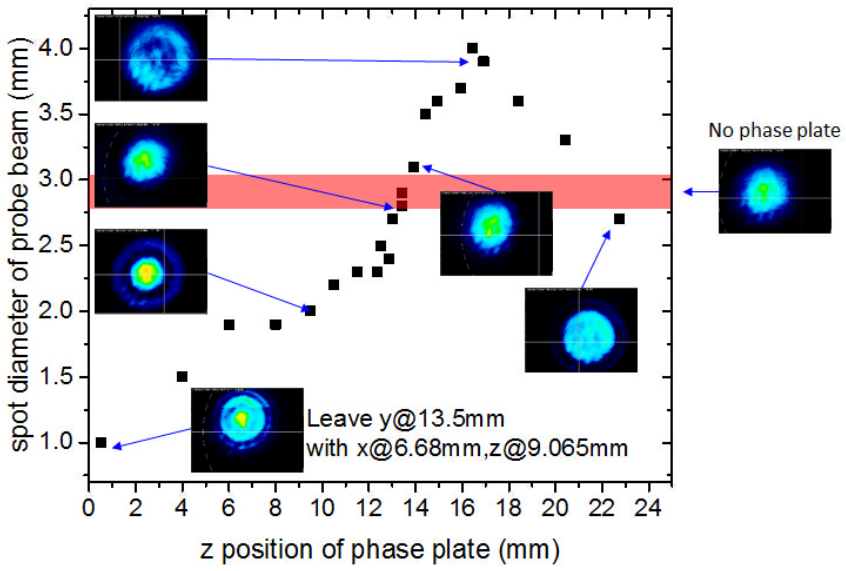

Figure 5.9: Coarse alignment of the tiny phase dot. Pictures show the diffraction pattern of the phase dot on the probe light without a BEC. At the optimal location (red regime), there should be no diffraction, which means the whole probe beam is hitting the phase dot. A larger value of z means a position closer to the objective lens.

For our case, the Thomas-Fermi radius of our BEC is about 16 μm (for 3×10^5 ^{87}Rb atoms in a harmonic trap with trapping frequencies $40 \times 40 \times 183$ Hz) and the $(1/e^2)$ diameter of the probe beam is 2 mm before passing the objective lens. Using the gaussian beam formulas, $w(z) = w_0\sqrt{1+(z/z_R)^2}$ and $z_R = \pi w_0^2/\lambda$, we estimate the $(1/e^2)$ diameter of the scattered beam is 1.4 mm and the $(1/e^2)$ diameter of the probe beam is 20 μm at the position of the phase plate. Therefore, a phase dot with diameter of 45μm is chosen to satisfy the condition, $20\mu\text{m} < 45\mu\text{m} \ll 1.4\text{mm}$. To align such a tiny spot, we do a coarse alignment without a BEC. We used a three-axis translation stage to control all $\{x, y, z\}$ positions of the phase plate. A beam profile camera (S-BC-XHR) was put ~ 10 cm after the focus point and before the "eyepiece" lens to monitor the diffraction pattern of the phase dot on the probe beam as shown in Fig. 5.9. First, we put the phase plate very close to the objective lens to align $\{x, y\}$ positions by looking at the diffraction. Here the probe beam has a large diameter, which makes the alignment easier. Next, we moved the phase plate along z towards the focus point step by step and the $\{x, y\}$ positions were corrected at every step. Finally,

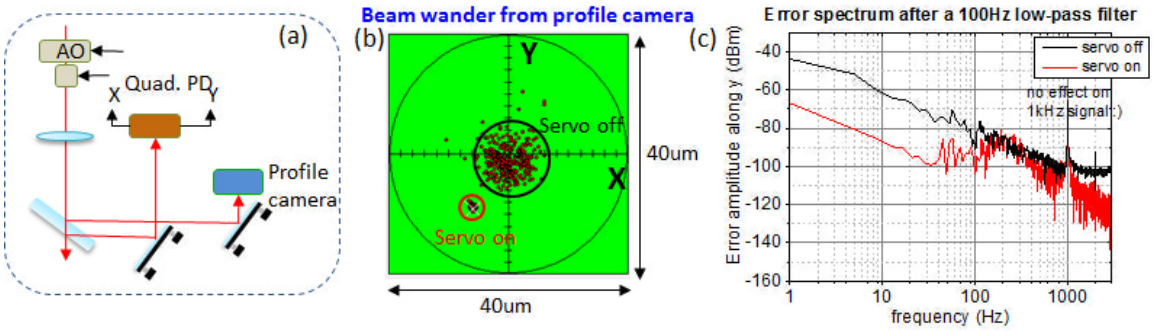

Figure 5.10: Stabilizing the time-averaged trapping potential. (a) Setup of the feedback system. The x and y positions of the trapping beam are monitored by a quadrant photodetector (SPOT-9DMI) and are stabilized by driving the AOMs using a feedback loop. A 100Hz low-pass filter is used in the feedback loop to avoid affecting the 1kHz painting trajectory. (b) Position stability with the servo system on and off measured by a beam profile camera. The center position of the time-averaged beam is recorded as a dot after every time step. (c) The error spectrum with the servo system on and off measured by a SRS FFT spectrum analyzer.

we found the best location without any diffraction, which means the whole probe beam is hitting the phase dot. After this, a fine alignment can be done by maximizing the phase signal of a BEC, which is straightforward.

5.2.2 Inducing slosh of a BEC

To measure the roundness of the trap, we measure the trapping frequencies by exciting a center-of-mass oscillation, or slosh, of a BEC in the x-y plane. One way of inducing slosh is to apply a magnetic-field gradient to kick the atom cloud. However, we tend to work with a relatively large bias magnetic field in the optical trap, which makes it difficult to induce significant slosh amplitude along both x and y using additional small magnetic-field coils. Instead, we can induce slosh by jumping the center position of the optical trapping potential. In fact, in our setup we have a feedback loop to reduce the low-frequency drift ($<$ 100Hz) of the center position of the time-averaged trapping potential (see Fig. 5.10 (a)). Fig. 5.10 (b) and (c) show that the position of the trapping potential can be well stabilized by the feedback loop. This also give us the freedom of jumping the positions of the optical trapping potential, simply by changing the control voltages

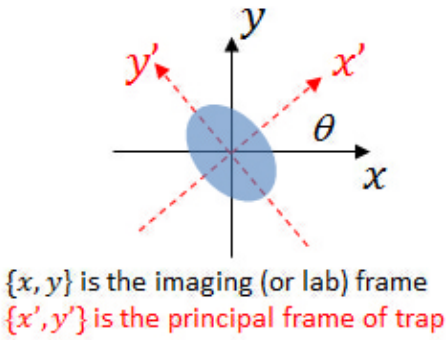

Figure 5.11: Lab frame and trap frame. x' is defined as the minor axis of the trapping potential and it corresponds to a higher trapping frequency f_+. y' is defined as the major axis of the trapping potential and it corresponds to a lower trapping frequency f_-.

that go into the servo electronics, to induce slosh of a BEC.

5.2.3 Rounding out the trap

To get a rotating gas, the trapping potential needs to be axially symmetric. That means the trapping frequencies along x and y need to be the same. In this section, I discuss how to adjust the painting parameters to make our trap as round as possible. Let's consider with an elliptical 2D trapping potential with principal axes denoted by $\{x', y'\}$ that have an angle of θ from the imaging frame $\{x, y\}$ (see Fig. 5.11). The center-of-mass motion of a BEC in this 2D trap can be treated as two independent 1D oscillations along the principal axes of the trapping potential. We can write the center trajectory as $x'_0(t) = A_{\text{min}} e^{-t/\tau} \cos(2\pi f_+ t)$ and $y'_0(t) = A_{\text{maj}} e^{-t/\tau} \sin(2\pi f_- t + \phi_0)$ with f_+ and f_- being the trapping frequencies along x' and y' respectively. Here the damping term is due to roughness of the time-averaged trapping potential. Usinng phase contrast imaging, we measure the BEC trajectory in the lab frame, or imaging frame, where the motion is connected with $\{x'_0(t), y'_0(t)\}$ through the frame transformation

$$\begin{pmatrix} x_0(t) \\ y_0(t) \end{pmatrix} = \begin{pmatrix} \cos\theta & -\sin\theta \\ \sin\theta & \cos\theta \end{pmatrix} \begin{pmatrix} x'_0(t) \\ y'_0(t) \end{pmatrix}. \tag{5.5}$$

To measure the trapping frequencies along both x' and y', a circular slosh trajectory is

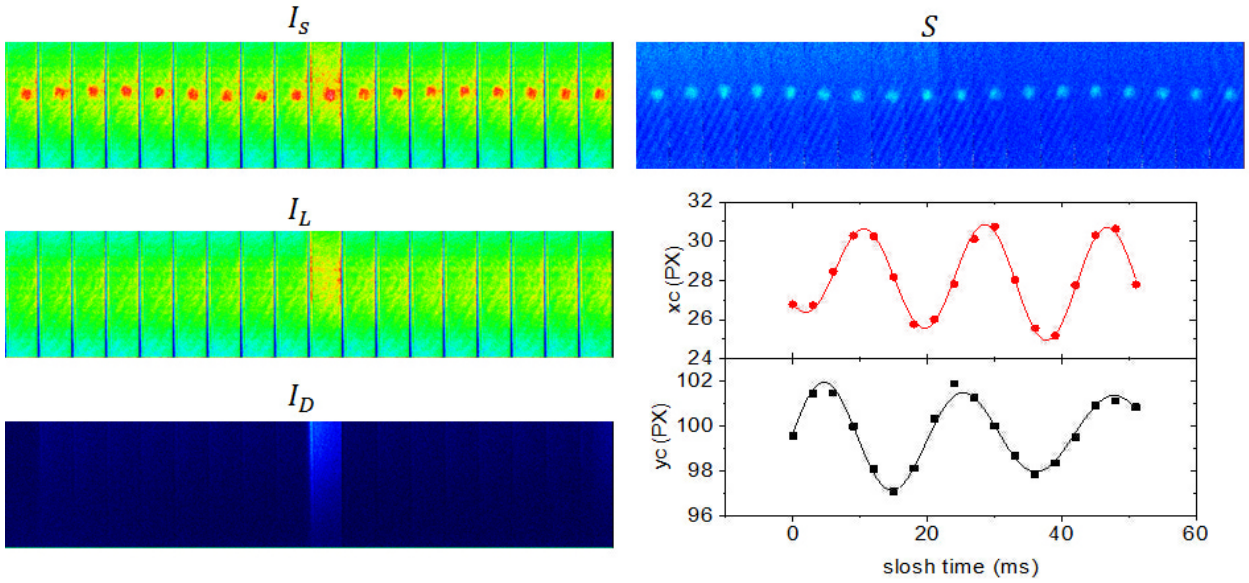

Figure 5.12: BEC slosh measurement for rounding out the trap. The probe beam is 600MHz red-detuned for phase contrast imaging. I_S, I_L and I_D are the shadow frame, light frame and dark frame, respectively. The final signal is obtained using $S = \left|\frac{I_S - I_D}{I_L - I_D} - 1\right|$. $\{x_0, y_0\}$ is the center position of the BEC cloud obtained by fitting the image(s) to a 2D gaussian. The lines through the data (points) show a fit to Eq. (5.5).

preferred. In the experiment, we first kicked the x position of the time-averaged trapping potential and a quarter trapping period later, the y position was kicked. (To kick the x or y position, we jump the center position of the trap and then immediately jump it back.) Limited by the camera CCD size (1024×1024 pixels), we can take 18 pictures for each readout of the CCD camera using a kinetics mode to shift the exposed pixels between pictures. As shown in Fig. 5.12, the trapping frequencies $\{f_+, f_-\}$ are obtained by fitting the slosh data to Eq. (5.5). To describe the roundness of the trapping potential, we define the ellipticity as $\varepsilon_{\rm trap} = (f_+^2 - f_-^2)/(f_+^2 + f_-^2)$ and the averaged radial trapping frequency as $f_\rho = (f_+ + f_-)/2$ [Coddington's thesis [93]]. A difference between f_+ and f_- causes a beat in the slosh with a beat frequency $f_b = f_+ - f_-$.

As discussed in Sec. 5.1.1, to get a time-averaged harmonic trapping potential, we use a painting trajectory described by

$$x_c(t) = A\rho_c(t)\cos(2\pi t/\mathcal{T}_1 + \varphi), \quad y_c(t) = B\rho_c(t)\sin(2\pi t/\mathcal{T}_1), \tag{5.6}$$

where $\rho_c(t)$ follows Eq. (5.3) with the period $\mathcal{T}$. Note that x_c is controlled by the vertical AOM and y_c by the horizontal AOM (see Fig. 5.1). In our experiment, we chose $1/\mathcal{T}_1 = 100$kHz, $1/\mathcal{T} = 1$kHz, and $b = 0.9$. Parameters $\{A, B, \varphi\}$ can be controlled independently in the experiment. Ideally, they should satisfy $A = B$ and $\varphi = 0$. In practice, due to the optical aberrations and imperfect alignment, the final painted trajectory can be different from the programmed function. This is why we need to measure the slosh of a BEC to optimize the experiment input parameters $\{A, B, \varphi\}$. In the experiment, φ is controlled by the DDS and $\{A, B\}$ could be changed by either the VGAs or the DDS (see Fig. 5.4). We chose to use the VGAs to round out the trap and the DDS was reserved for the stirring process discussed in Sec. 5.5.

From the slosh data, we can measure $\{f_+, f_-, \theta\}$ that describe the harmonic trapping potential. To connect such information to the painting trajectory in the lab frame, we can write an equipotential contour as

$$
\begin{aligned}
f_+^2 x'^2 + f_-^2 y'^2 &= const \\
\begin{pmatrix} x' & y' \end{pmatrix} \begin{pmatrix} f_+^2 & 0 \\ 0 & f_-^2 \end{pmatrix} \begin{pmatrix} x' \\ y' \end{pmatrix} &= const \\
\begin{pmatrix} x & y \end{pmatrix} \begin{pmatrix} \cos\theta & -\sin\theta \\ \sin\theta & \cos\theta \end{pmatrix} \begin{pmatrix} f_+^2 & 0 \\ 0 & f_-^2 \end{pmatrix} \begin{pmatrix} \cos\theta & \sin\theta \\ -\sin\theta & \cos\theta \end{pmatrix} \begin{pmatrix} x \\ y \end{pmatrix} &= const \\
\begin{pmatrix} x & y \end{pmatrix} \begin{pmatrix} f_+^2\cos^2\theta + f_-^2\sin^2\theta & (f_+^2 - f_-^2)\sin\theta\cos\theta \\ (f_+^2 - f_-^2)\sin\theta\cos\theta & f_+^2\sin^2\theta + f_-^2\cos^2\theta \end{pmatrix} \begin{pmatrix} x \\ y \end{pmatrix} &= const \\
\left(f_+^2\cos^2\theta + f_-^2\sin^2\theta\right)x^2 + \left(f_+^2\sin^2\theta + f_-^2\cos^2\theta\right)y^2 + [(f_+^2 - f_-^2)\sin 2\theta]xy &= const. \quad (5.7)
\end{aligned}
$$

On the other hand, due to the optical aberrations and imperfect alignment, the final painted trajectory can be different from the programmed function (see Eq. (5.6)). An effective painted trajectory in the lab frame can be generally expressed as $\tilde{x}_c(t) = \tilde{A}\rho_c(t)\cos(2\pi t/\mathcal{T}_1 + \tilde{\varphi})$ and $\tilde{y}_c(t) = \tilde{B}\rho_c(t)\sin(2\pi t/\mathcal{T}_1)$. To obtain values of $\{\tilde{A}, \tilde{B}, \tilde{\varphi}\}$ from the measured $\{f_+, f_-, \theta\}$, we write the effective painted trajectory into the following form

$$
\tilde{B}^2\tilde{x}_c^2 + \tilde{A}^2\tilde{y}_c^2 + \frac{2\tilde{A}\tilde{B}}{\sin\tilde{\varphi}}\tilde{x}_c \cdot \tilde{y}_c = const. \quad (5.8)
$$

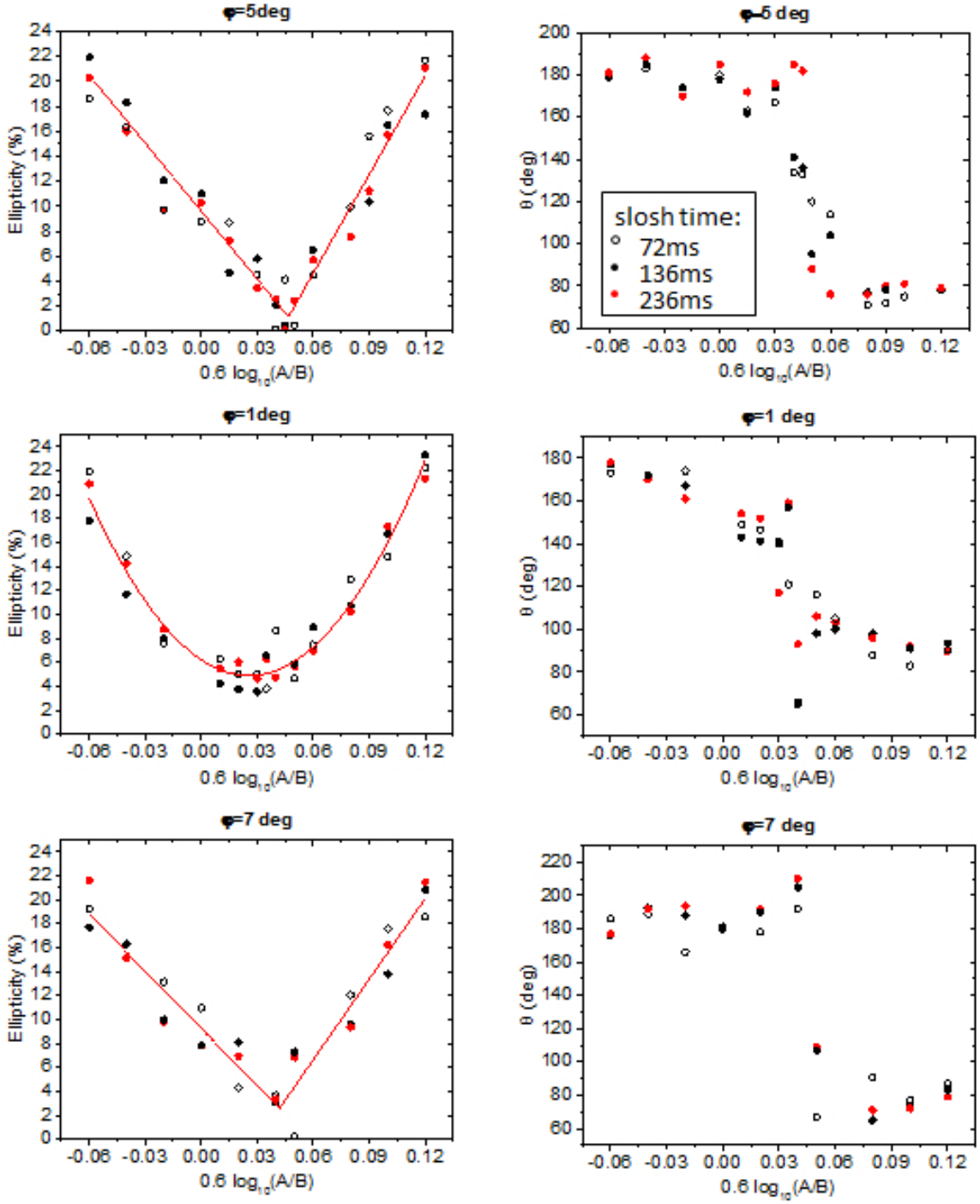

Figure 5.13: Ellipticity of the trapping potential versus the painting trajectory. Curves are guides to the eye. The x axes show the voltage going to the VGAs that we used for controlling A and B. At $\varphi = 5$ deg, we get the minimum ellipticity.

By comparing Eqs. (5.7) and (5.8), we get the following relationship

$$\begin{aligned} \tilde{A}/\tilde{B} &= \sqrt{\frac{f_+^2 \sin^2\theta + f_-^2 \cos^2\theta}{f_+^2 \cos^2\theta + f_-^2 \sin^2\theta}}, \\ \tilde{\varphi} \approx \sin\tilde{\varphi} &= \begin{cases} \frac{\sqrt{\left(f_+^2 - f_-^2\right)^2 \sin^2\theta\cos^2\theta + f_+^2 f_-^2}}{\left(f_+^2 - f_-^2\right)\sin\theta\cos\theta} & \text{if } \theta \neq 0, \pm\pi/2, \pm\pi, \cdots \\ 0 & \text{if } \theta = 0, \pm\pi/2, \pm\pi, \cdots \end{cases}, \end{aligned} \tag{5.9}$$

which is valid when $f_+ \neq f_-$. Eq. (5.9) is useful in the sense that it tells us how we need to change A, B and φ to reduce the ellipticity, namely, $\{A/B \to A/B \cdot (\tilde{B}/\tilde{A}), \varphi \to \varphi - \tilde{\varphi}\}$.

Figure 5.13 shows some typical data for rounding out the trap. We need to optimize the ellipticity in a 2D parameter space $\{A/B, \varphi\}$. Only when both A/B and φ are optimized, we find that we can get the ellipticity below 1%. This measured minimal ellipticity may be limited by the measurement time. When close to the optimal settings, the value of θ becomes very sensitive to the value of A/B and θ jumps by 90 deg as A/B crosses the optimal value.

5.3 Anharmonicity

In addition to imperfect roundness of the trapping potential, anharmonicity and roughness can also limit the rotating rate of our ultracold gases. In this section, I discuss the anharmonicity for our time-averaged trapping potential. To discuss an anharmonic oscillation, it is good to start with the Lagrangian [94]

$$L = \frac{1}{2}m\dot{x}^2 - \frac{1}{2}m\omega_0^2 x^2 - \frac{1}{3}m\alpha x^3 - \frac{1}{4}m\beta x^4,$$

that includes x^3 and x^4 anharmonic terms with correspondent weights α and β. The trapping potential is then

$$U(x) = \frac{1}{2}m\omega_0^2 x^2 + \frac{1}{3}m\alpha x^3 + \frac{1}{4}m\beta x^4.$$

The corresponding equation of motion is

$$\ddot{x} + \omega_0^2 x = -\alpha x^2 - \beta x^3.$$

The solution of the above equation has been given in Ref. [94] and is given as follows

$$x(t) = x^{(1)} + x^{(2)} + x^{(3)}, \quad \omega = \omega_0 + \omega^{(1)} + \omega^{(2)}, \tag{5.10}$$

with

$$\begin{aligned} x^{(1)} &= A\cos\omega t, & \omega^{(1)} &= 0 \\ x^{(2)} &= -\frac{\alpha A^2}{2\omega_0^2} + \frac{\alpha A^2}{6\omega_0^2}\cos 2\omega t, & \omega^{(2)} &= \left(\frac{3\beta}{8\omega_0} - \frac{5\alpha^2}{12\omega_0^3}\right)A^2 \\ x^{(3)} &= \frac{A^3}{16\omega_0^2}\left(\frac{\alpha^2}{3\omega_0^2} - \frac{1}{2}\beta\right)\cos 3\omega t. \end{aligned}$$

There are two features about this solution. The first is that the slosh frequency ω depends on the slosh amplitude A. The second is that the odd anharmonic term, x^3, can cause an offset shift of the slosh and this shift depends on the slosh amplitude.

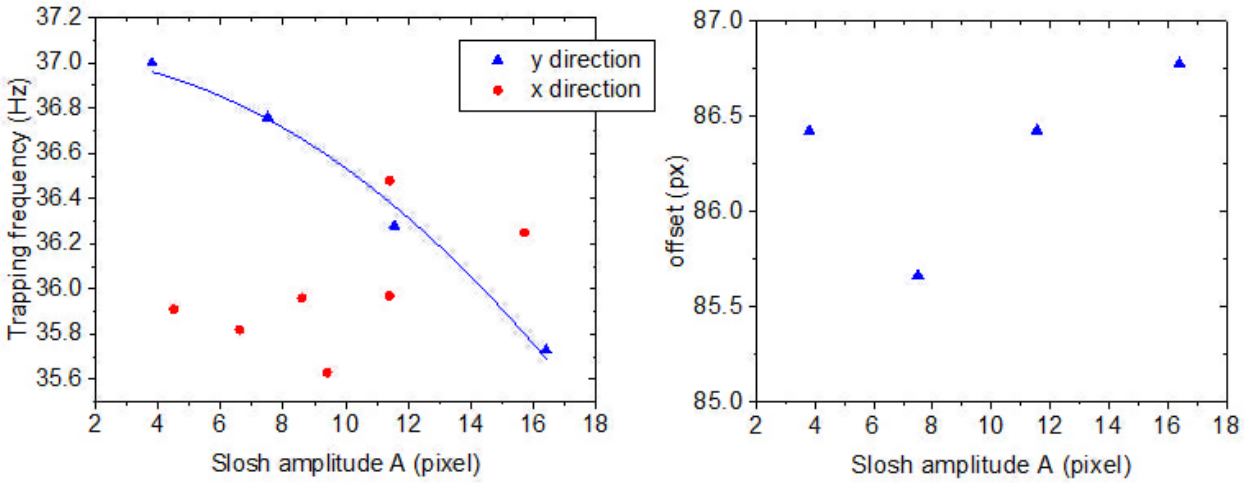

Figure 5.14: Effect of the anharmonic trapping potential on slosh. Red and blue points are measured separately using 1D slosh. Along y, we see a clear amplitude dependence of $\omega(A) = \omega_0 - 0.031(\mathrm{Hz/px^2})A^2$ (blue line), while the slosh offset is basically unchanged. This indicates a dominant x^4 term along y. The offset along x is not shown because of the relatively small anharmonicity. (1 px=1.38 μm).

Fig. 5.14 shows our measurement of anharmonicity of our time-averaged trapping potential. In order to tell which of the anharmonic terms, x^3 or x^4, is dominant, I consider the case where the dominant anharmonicity is from the x^3 term. In this case, by fitting our trapping frequency

data to the equation, $\omega(A) = \omega_0 - \frac{5\alpha^2}{12\omega_0^3}A^2$, we get the weight, $\alpha = \pm 973$ px^{-1}s^{-2}, and therefore the displacement, $|\Delta x(A)| = \left|\frac{\alpha A^2}{2\omega_0^2}\right| = 0.009A^2$, which does not match our slosh offset data in Fig. 5.14. This suggests that the x^4 term is the dominant anharmonic term. Fitting our trapping frequency data to the equation, $\omega(A) = \omega_0 + \frac{3\beta}{8\omega_0}A^2$, we get the weight, $\beta = -19.44$ px^{-2}s^{-2}, and the trapping frequency, $\omega_0 = 2\pi \times 37$Hz. It further gives $x^{(3)} = 11.2 \times 10^{-6}A^3 \cos 3\omega t$, which is so small compared to $x^{(1)} = A\cos\omega t$ that it won't have a significant effect on our slosh data. The fact that there is a bigger anharmonic effect on slosh along y than that along x suggests that the anharmonic source comes from the asymmetric part of the trapping potential, namely, the sheet beam (see next section).

5.4 Roughness

In this section, I discuss the roughness of our optical trapping potential. Roughness refers to high spatial frequency (short wavelength) defects in the trapping potential. We suspect that the sheet beam might have the dominant roughness. The setup of the sheet beam is shown in Fig. 5.15(a). We want the sheet beam to provide the vertical confinement. Hence, its beam profile was designed to have a small beam waist (30μm) along the vertical direction z and a large beam waist along y as shown in Fig.5.15(b). To reduce the roughness and to further flatten the horizontal confinement, we use an AOM to paint the sheet beam along y at 300 kHz; the resulting time-averaged laser intensity is shown in Fig. 5.15(c).

One way to probe the roughness of the sheet beam is to expand the Rb BEC in the sheet beam by turning off the vertical painted trapping beam while keeping the sheet beam on. After some time-of-flight (TOF), the density distribution of the expanded BEC is imaged using absorption imaging. Fig. 5.16(a) shows the BEC distribution after expanding in the sheet beam for different TOFs. The roughness of the trap results in parallel stripes seen at large expansion times (> 15 ms). The orientation of these stripes is coincident with the propagating direction of the sheet beam.

To emphasize the effect of the trap roughness, we lowered the chemical potential of the BEC to be closer to the quasi-2D regime, where the BEC density is more strongly affected by roughness

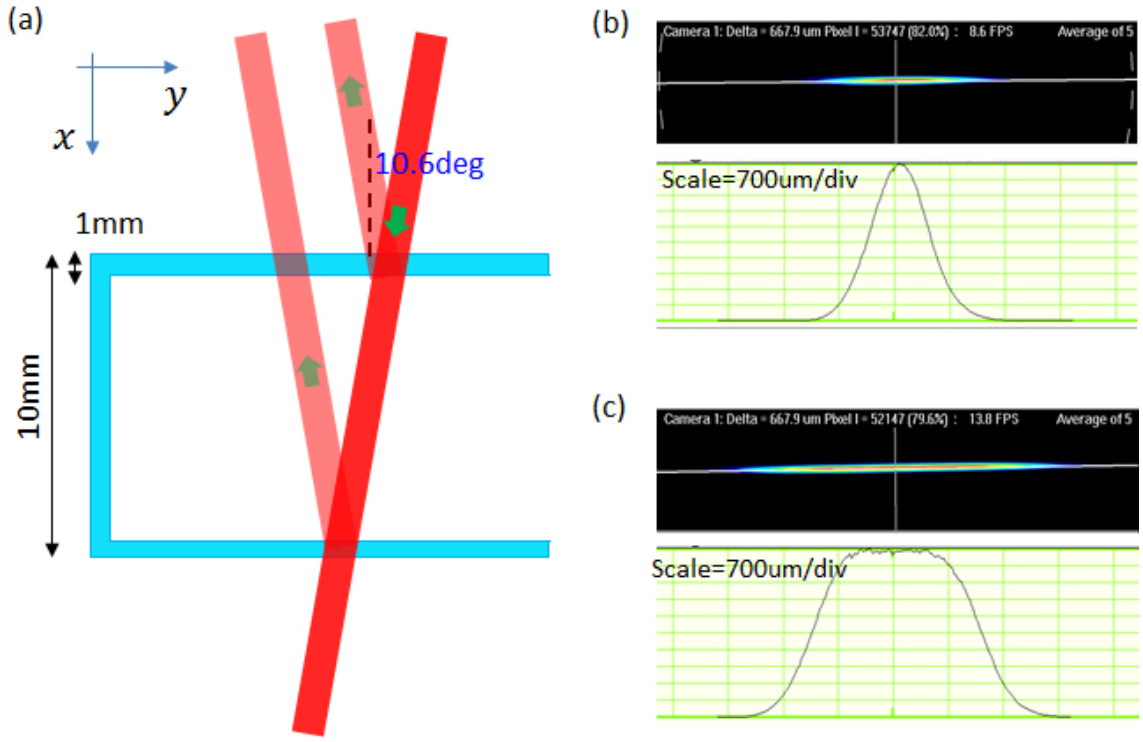

Figure 5.15: Sheet beam information. (a)Sheet beam configuration. The sheet beam enters the science cell (cyan regime) with an incident angle of 10.6 deg, which was chosen to avoid overlapping with the reflected beams. Roughness could be caused by imperfection in the glass wall of the cell. (b) Static sheet beam. The vertical $(1/e^2)$ beam waist is 30μm and the horizontal waist is 700μm. (c) "Painted" sheet beam. The central regime is flat as we expect.

in the trap potential. In the experiment, this was done by reducing the BEC number (from $\sim 10^5$ to $\sim 10^4$) as well as decreasing the radial trapping frequency (from $2\pi \times 40$ Hz to $\sim 2\pi \times 2$ Hz) by lowering the vertical beam power. Fig. 5.16(b-d) shows the detected BEC density distributions that reveal the trap roughness. In Fig. 5.16(b) and (c), the location of the stripes was monitored when moving the vertical trap beam along y and x respectively. It turns out that the stripes stay at the same location independent of the vertical beam position. In addition, the stripes exist even when the vertical beam power is weak. All these evidences suggest that the stripes are coming from the sheet beam. In Fig. 5.16(d), we see that the location of the stripes was unchanged when moving the sheet beam along y. This is consistent with the fact that our painting in y does not remove the roughness. A likely situation is that the cell glass has some fine structure that results

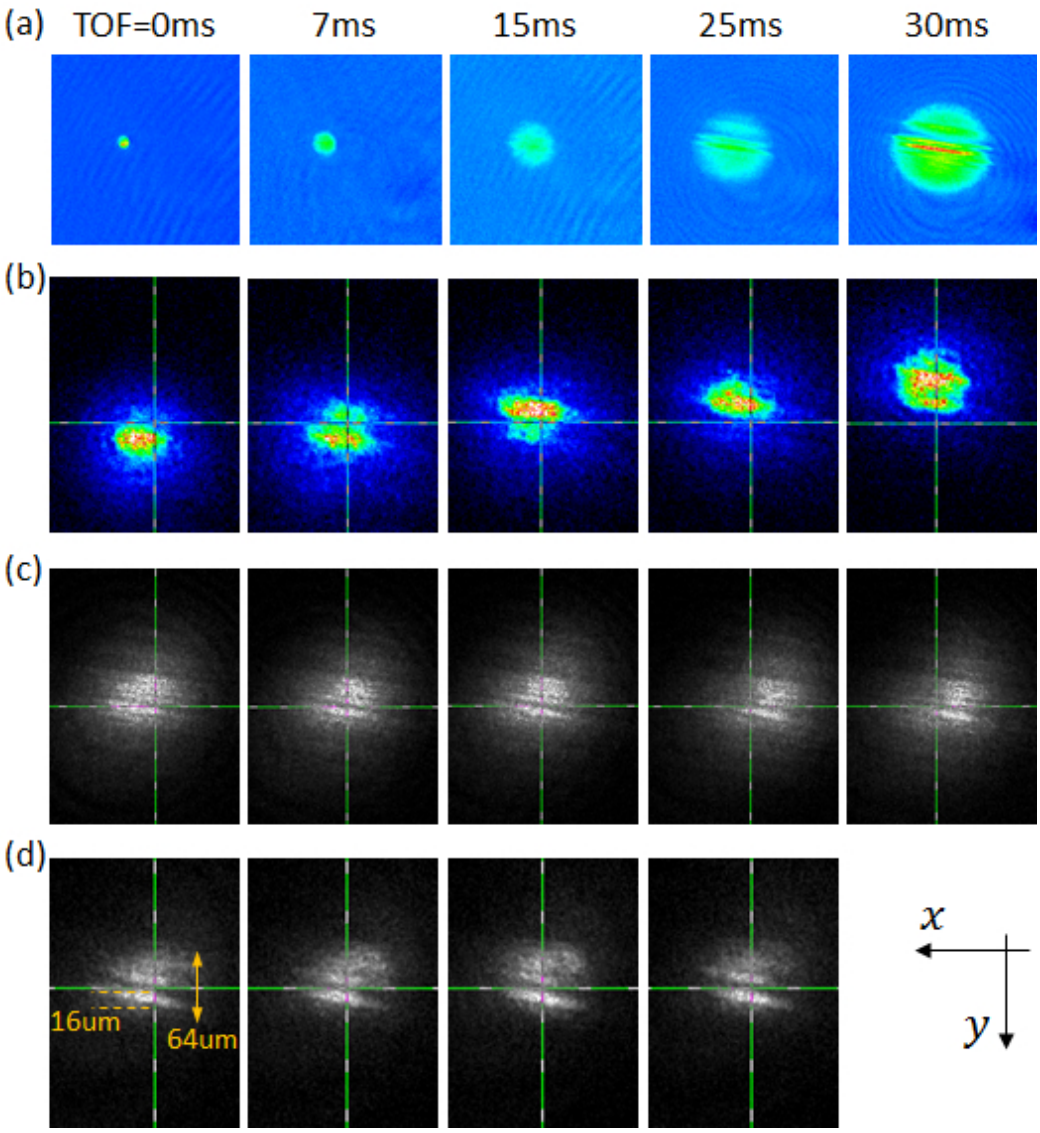

Figure 5.16: Detecting the roughness of the sheet beam using the density distribution of a BEC. (a) BEC density distribution after expanding in the sheet beam for different TOFs. (b) Monitoring the locations of stripes when moving the vertical beam along y. The green lines provide a reference for ease of comparing the location of structure in the density profile. (c) Monitoring the locations of stripes when moving the vertical beam along x. (d) Monitoring the locations of stripes when moving the sheet beam along y. The size of stripes was measured to be 16μm.

in shadows in the sheet beam. Because the cell wall is only ~ 5 mm from the atoms, motion of the sheet beam in y (with painting or by moving the center of the beam) is primarily translation (instead of a change in angle), which does not change the location of the shadow. We estimated

the roughness in Fig. 5.16(d) to be 15 nK by measuring the chemical potential of the BEC and estimated the trap depth to be 3 μK, which give a fractional roughness of the trapping beam of 0.5%. This roughness is suspected to limit the rotation rate ($\Omega/\omega_\perp = 0.7$) that we achieved so far (see Sec. 5.7), which is not enough for reaching the quantum Hall regime ($\Omega/\omega_\perp > 0.9$).

Based on the above analysis,we have designed a new sheet beam. The new beam has a similar beam profile but with a much larger range of painting, which gives a significant angle change of the beam at the cell that should wash out the roughness caused by the cell glass. Meanwhile, in the following sections, I present rotation results using the existing setup.

5.5 Rotating a Rb BEC

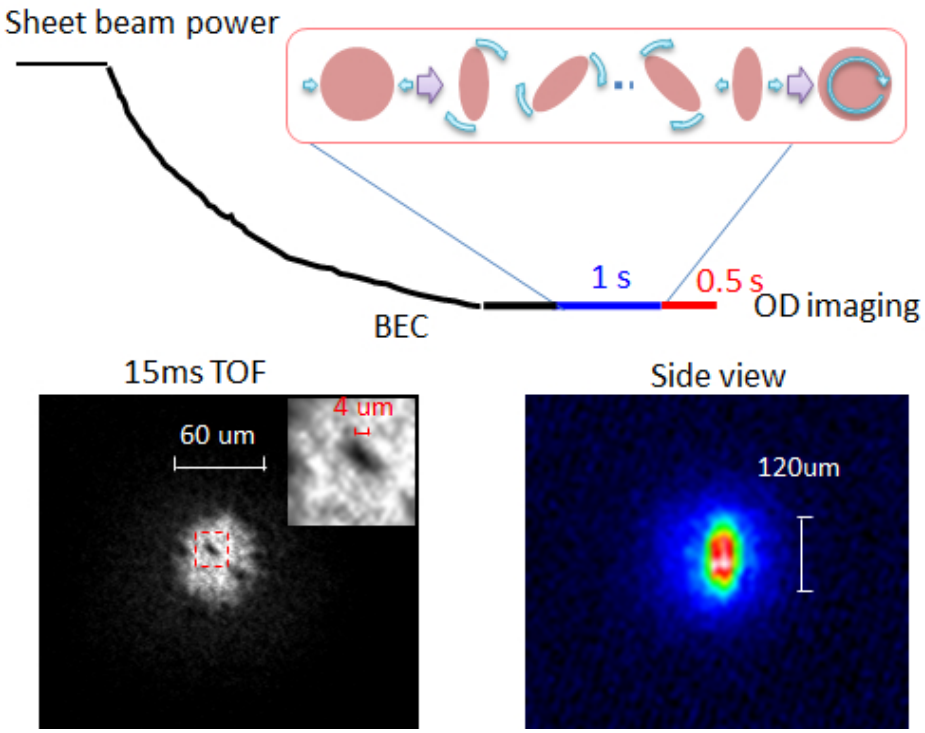

Figure 5.17: Rotating a Rb BEC. The sheet beam power was lowered to evaporate Rb atoms to get a BEC of about 10^5 atom; To stir the BEC, we changed the vertical time-averaged trapping potential to be elliptical and then rotated the elliptical trap for 1 s. After stirring, the trap geometry was restored to a round shape and the cloud was imaged after a 500ms thermalization time. The picture on the left comes from the top imaging system introduced in Sec. 5.1.2, while the picture on the right is from a side imaging system that has a magnification of 3 (not shown in Fig. 5.1).

After the above optimizations, we tried rotating a Rb BEC and looked for BEC vortices for the first time in my lab. An experimental timing diagram of the procedure is illustrated in Fig. 5.17. We started with a thermal Rb cloud around 2 μK. To get a BEC, the sheet beam power was lowered to evaporate Rb atoms and achieve a BEC of about 10^5 atoms. To rotate the BEC, we programmed the DDS to change the vertical time-averaged trapping potential to be elliptical and rotated the elliptical trap for 1 s. After this stirring, the trap geometry was restored back to a round shape and we waited 500 ms for thermalization before taking an absorption imaging. To be able to resolve the vortex structure, we expanded the BEC for 15ms before imaging. As shown in Fig. 5.17, vortices were detected, which is proof that we created a rotating BEC. The observed small structure is consistent with the diffraction limited resolution of 3.9 μm. This experiment demonstrates that our imaging system is capable of resolving vortex structure in a rotating BEC, which is crucial for a rotating BEC experiment. However, the rotation rate achieved by this stirring process is far from rapid rotation as indicated by the low vortex number. Next, we wanted to test out a spin-up evaporation technique to speed up the rotation.

5.6 Spin-up evaporation technique

A spin-up evaporation technique has been successfully demonstrated in a magnetic trap [75]. It consists of an evaporation process that can increase the average rotation rate per atom by evaporating away atoms not just with high energy but also with low angular momentum. We wanted to extend this technique to an optical trapping potential. The basic idea is based on the angular-momentum or rotation-rate distribution of atoms in a harmonic trap. For an atomic gas rotating around the z axis, assuming rigid-body rotation, the angular momentum, $L_z = m\rho^2\Omega$, indicates that the atoms with larger ρ have higher angular momentum as shown in Fig. 5.18. In the experiment, when we evaporate the gas by lowering down the sheet beam power, the atoms around the $-z$ edge (indicated by the dashed line) are removed due to gravity. Most of these removed atoms carry relatively low angular momentum. As a result, the average angular momentum per atom increases.

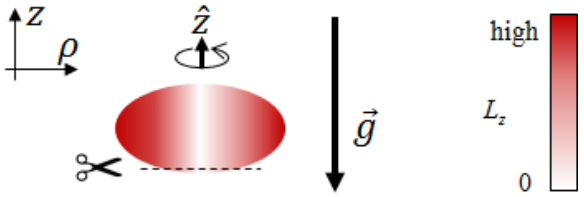

Figure 5.18: The idea of spin-up evaporation. When we perform evaporation by lowering the sheet beam power, atoms near the $-z$ edge (indicated by the dashed line) are removed due to gravity.

5.6.1 Monte-Carlo simulation

To further explore this strategy, we did a numerical simulation of spin-up evaporation in the optical trap. The simulation procedure is described in Fig. 5.19. At $t = 0$, we want to generate

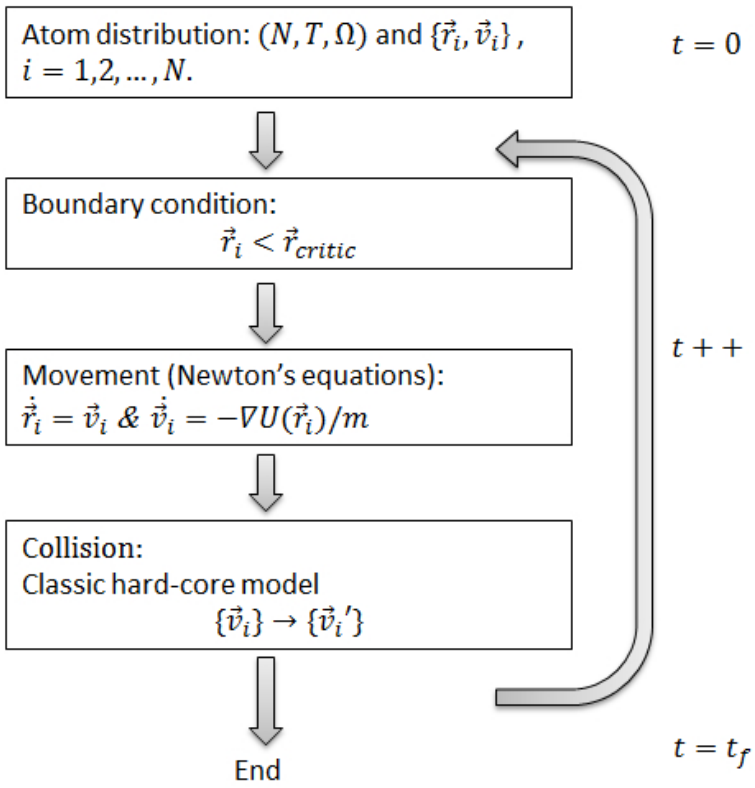

Figure 5.19: Procedures of the Monte-Carlo simulation.

$N = 9 \times 10^3$ atoms that were randomly distributed following a Maxwell-Boltzmann distribution in

a trapping potential $U(\vec{r})$ with an initial rotation rate $\Omega = 0.4\omega_\rho$ and temperature $T = 200$ nK. (ω_ρ is the radial trapping frequency.) To achieve this, we first generate N atoms without rotation in a trapping potential $U(\vec{r}) - \frac{1}{2}m\Omega^2\rho^2$ with the temperature T (see details of the random distribution algorithm in Append. A of Cumby's thesis [22]). The position and velocity, $\{\vec{r}_i, \vec{v}_i\}$, of each particle is recorded. Based on the fact that atoms moving in a potential $U(\vec{r}) - \frac{1}{2}m\Omega^2\rho^2$ in a rotating frame (with the rotation rate Ω) are identical to atoms that rotate at the rate Ω and feel a potential $U(\vec{r})$ in the lab frame, the initial rotation rate of Ω was imparted to the atoms by a transformation of coordinates

$$\begin{cases} x_i = x_i \\ y_i = y_i \end{cases}, \qquad \begin{cases} v_i^x = v_i^x - \Omega y_i \\ v_i^y = v_i^y + \Omega x_i \end{cases}, \tag{5.11}$$

where $\vec{r}_i = \{x_i, y_i, z_i\}$ and $\vec{v}_i = \{v_i^x, v_i^y, v_i^z\}$ are used. Thus, we prepared N atoms that were randomly distributed following a Maxwell-Boltzmann distribution in a trapping potential $U(\vec{r})$ with an initial rotation rate Ω and temperature T. In our simulation, the trapping potential $U(\vec{r})$ was described by

$$U(\vec{r}) = \frac{1}{2}m\omega_\rho^2(x^2+y^2) + \alpha\frac{2P}{\pi w_y(x) w_z(x)}\exp\left(-\frac{2y^2}{w_y(x)^2} - \frac{2z^2}{w_z(x)^2}\right) + mgz,$$

where the first term is a round harmonic trap along the radial direction, the second term describes the sheet beam with the beam power P, and the third term is due to gravity. The polarizability $\alpha = -1.9 \times 10^{-36}$ m^{2}s. $w_y(x) = w_y^0\sqrt{1+(x/x_{Ry})^2}$ with w_y^0 being the $1/e^2$ beam width along y and the Rayleigh range $x_{Ry} = \pi(w_y^0)^2/\lambda_t$. $w_z(x) = w_z^0\sqrt{1+(x/x_{Rz})^2}$ with w_z^0 being the $1/e^2$ beam width along z and the Rayleigh range $x_{Rz} = \pi(w_z^0)^2/\lambda_t$. ($\lambda_t = 1090$ nm). For this simulation, I set $w_z^0 = 7$ μm and $w_y^0 = 300$ μm.

The time evolution of the atoms during an evaporation process was simulated numerically for our optical trapping potential using the Monte-Carlo method described in [95, 96]. The boundary condition is determined by the border between the trapping and anti-trapping regimes (it is approximately a plane at the $-z$ edge). The collision includes only the elastic collision based on a hard core model [60]. Fig. 5.20(a) shows the numerically generated atoms (dots) in our optical

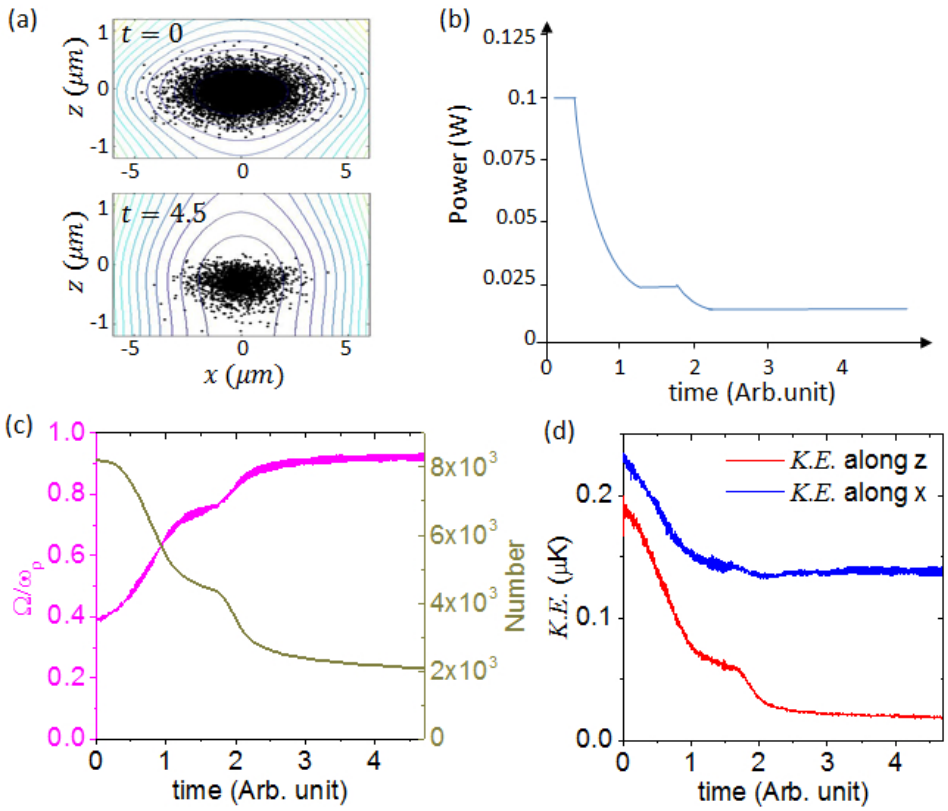

Figure 5.20: Monte-Carlo simulation of the spin-up evaporation. (a) Atom distribution in our optical trapping potential. (b) The sheet beam power is exponentially lowered to evaporate the atoms. (c) & (d) The simulation results. The rotation rate increases significantly through the spin-up evaporation. The kinetic energy is lowered as expected.

trapping potential $U(\vec{r})$ at $t = 0$. The evaporation was done by lowering the sheet beam power, which lowered the potential barrier on the $-z$ edge due to gravity (see the lower panel of 5.20(a)). The trajectory, $\{\vec{r}_i, \vec{v}_i\}$ of each atom was recorded after every time step. From the trajectory, we can calculate the kinetic energy ($K.E.$), angular momentum L_z, inertia I_z, and rotation rate by

$$N = \sum_i 1, \qquad K.E. = \sum_i \frac{1}{2} m r_i^2 / N,$$

$$L_z = m \sum_i (x_i v_i^y - y_i v_i^x), \qquad I_z = m \sum_i (x_i^2 + y_i^2),$$

$$\Omega = L_z / I_z.$$

Fig. 5.20(c) & (d) show our simulation results. The evaporation trajectory is illustrated in

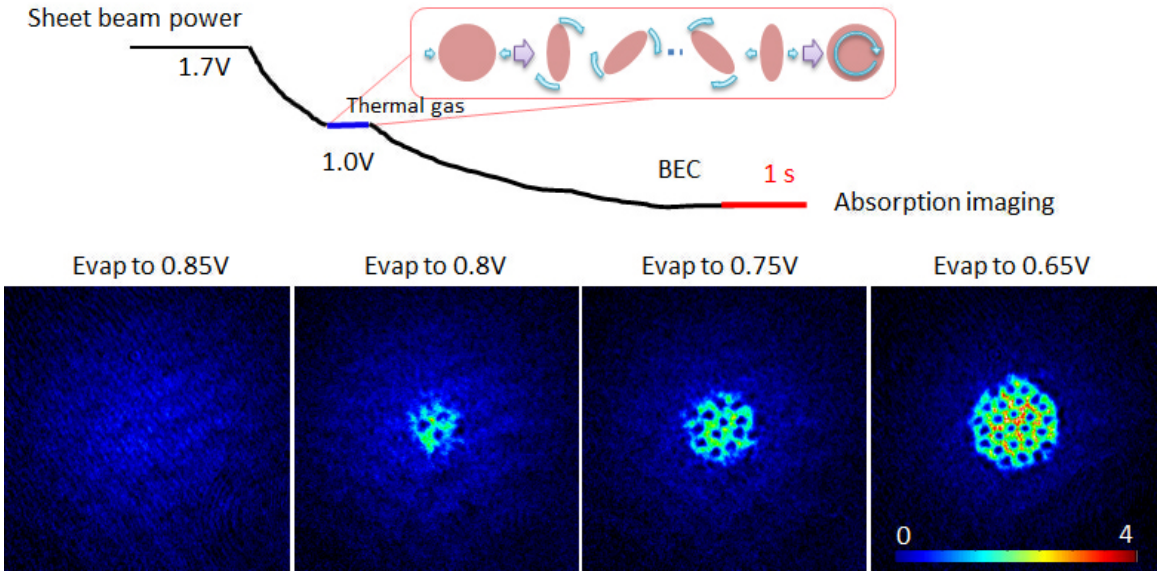

Figure 5.21: Experimental sequence of the spin-up evaporation. The stirring process was performed after we started evaporating but before a BEC formed. After that, we continued evaporating. The voltages shown above are proportional to the sheet beam power. When evaporating to 0.85V, the imaged atom density shows that all atoms were in the thermal or uncondensed state. Once we evaporated to 0.8V, a BEC formed with vortices due to rotation. As we evaporated further, the BEC got larger. Meantime, more vortices showed up, which indicated a faster rotation rate. The images were taken after a TOF=15ms expansion.

Fig. 5.20(b) and it can also be seen in the atom number decrease as a function of time and the corresponding decrease in kinetic energy. At the same time, the rotation rate increases significantly. Note that the kinetic energy along x is higher than that along z due to the rotation.

5.6.2 Experimental verification

In the experiment, spin-up evaporation can be realized simply by following the timing sequence shown in Fig. 5.17, but performing the stirring process earlier. As shown in Fig. 5.21, we performed the stirring process after we started evaporating but before a BEC formed. Then we continued evaporating until a BEC formed. As you can see from Fig. 5.21, vortices appeared as soon as a BEC formed. As we evaporated further, the BEC number grew and more vortices appeared, which indicates a faster rotation rate. This behavior demonstrates that the spin-up

evaporation works for our situation.

5.7 Rotation rate

Vortex lattice. In a harmonic trapping potential, vortices in a low-temperature BEC form a triangular lattice (or "Abrikosov" lattice). However, imperfection of the trapping potential can cause partial melting of the vortex lattice, dislocations, and grain boundaries [71]. An example of near-perfect vortex lattice can be found in [97]. In our situation, shown in Fig. 5.22(a-b), we see some dislocations in the vortex lattice, which we attribute to roughness of our trapping potential. If we evaporate further, the density of vortices does not increase. Instead the shape of the whole BEC deforms to be somewhat triangular, which indicates the excitation of surface modes; this can be seen in Fig. 5.22 (c-d).

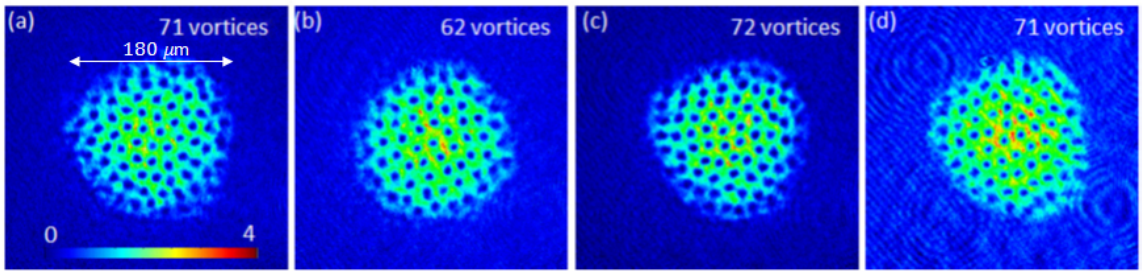

Figure 5.22: Vortex lattice of a rotating BEC. (a-b) Example images of the fastest rotating BEC we have achieved. The vortex lattice is not perfect due to the roughness of our trapping potential. (c-d) BEC vortex lattice for deeper evaporation. The vortex density didn't increase. Instead the shape of the whole BEC deformed to be triangular, which indicates the excitation of surface modes. The BEC was expanded in the sheet beam for 3 ms and then expanded in the free space for 15 ms before the absorption imaging.

Rotation rate. An effective way to measure the rotation rate is to use the aspect ratio of the atom cloud (the axial size over the radial size) imaged in-situ [75]

$$\Omega/\omega_\rho = \sqrt{1-(\lambda/\lambda_0)^2}, \tag{5.12}$$

where λ_0 and λ are the initial and final aspect ratios of the cloud respectively. Here, the centrifugal force increases the transverse cloud size compared to the axial size. However, because the BEC size

along z (Thomas-Fermi radius $R_{TF}^{z} \sim 3\ \mu$m) is below our imaging resolution, it is difficult for us to measure this aspect ratio accurately. Instead, we can estimate the rotation rate from the measured aspect ratio of an expanded cloud. For this we need a model of BEC expansion [98, 99]. From the expanded BEC cloud, we estimate the rotation rate of the BEC in Fig. 5.22(a-b) to be $\Omega/\omega_\rho \approx 0.7$. An alternative way to extract the rotation rate is to use the vortex density in-situ [15]

$$n_v = \mathcal{N}_v/\mathcal{A} = M\Omega/\pi\hbar$$

where $\mathcal{N}_v$ is the vortex number in the area $\mathcal{A}$ and M is the atomic mass of an atom. Since we count vortices on an expanded rotating BEC, to get the vortex density in-situ, we also need the model of BEC expansion [98, 99].

5.8 Future directions

In this thesis, I presented our work developing and optimizing our apparatus by rotating a ^{87}Rb BEC. In future experiments, we would like to rotate a different atomic species such as bosonic ^{39}K, which has a convenient Feshbach resonance for tuning the interaction strength, or fermionic ^{40}K. Since our trap is all-optical, the techniques we have demonstrated should be readily applicable to these other species.

Chapter 6

Conclusions and outlook

In this Thesis, I explored some interesting many-body physics in an ultracold gas mixture of ^{87}Rb and ^{40}K atoms.

The first one is a study of Bose polarons as discussed in Chap. 3. I report experimental evidence of Bose polarons by using radio-frequency spectroscopy to measure the excitation spectrum of fermionic ^{40}K impurities resonantly interacting with a BEC of ^{87}Rb atoms. We find that the measured energy of the impurites immersed in the BEC matches well with that calculated for Bose polarons for a range of interaction strengths. In particular, we confirm that the polaron state exists even across unitarity in the strongly interacting regime and approaches the weakly bound molecular state. Furthermore, for attractive interactions, we show that Rabi oscillations can be observed when exciting Bose polarons. This work is the first measurement of the Bose polaron in a three-dimensional trapped atom gas, which helps better understanding of the quantum many-body physics of Bose-Fermi mixtures.

The second topic is related to the quantum Hall effects as discussed in Chap. 4 and 5. The interesting and bizarre quantum Hall effects are reviewed and their connection with a rapidly rotating ultracold gas is discussed. To realize these quantum Hall states by using ultracold atoms, we design and construct a new apparatus for creating rotating ultracold atomic gases. Technical challenges are explored and experimental progress is discussed.

Besides studying quantum Hall physics, such a versatile apparatus is also promising to explore other interesting physics such as rotating a strongly interacting BEC and the effect of dimensionality

on the BEC/BKT transition.

Although rotating a BEC has been studied for more than a decade, as far as I know no one has studied a rotating BEC with tunable interactions. With tunable interactions via the Feshbach resonance, the ^{39}K is the best candidate for us to study BEC vortices with tunable interactions.

Another interesting project that we are probably able to study by our unique apparatus is the effect of dimensionality on the BEC/BKT transition. As you know, the BKT is a phase transition from a well-ordered BEC superfluid to a partially-ordered BKT superfluid when changing dimensionality from 3D to 2D. As demonstrated in Sec. 5.4, we are able to control the dimensionality from 3D to 2D through our unique apparatus. Thus it is possible for us to map out a phase diagram of the BEC/BKT transition.

Bibliography

[1] G. D. Mahan. Many-Particle Physics 3nd edn. Plenum, New York, 2000.

[2] G. E. Astrakharchik and L. P. Pitaevskii. Motion of a heavy impurity through a bose-einstein condensate. Phys. Rev. A, 70:013608, 2004.

[3] F.M. Cucchietti and E. Timmermans. Strong-coupling polarons in dilute gas bose-einstein condensates. Phys. Rev. Lett., 96:210401, 2006.

[4] R. M. Kalas and D. E. Blume. Interaction-induced localization of an impurity in a trapped bose-einstein condensate. Phys. Rev. A, 73:043608, 2006.

[5] Bao W. Bruderer, M. and D. Jaksch. Self-trapping of impurities in bose-einstein condensates: Strong attractive and repulsive coupling. EPL, 82:30004, 2008.

[6] B.-B. Huang and S.-L. Wan. Polaron in bose-einstein-condensation system. Chin. Phys. Lett., 26:080302, 2009.

[7] J. Tempere, W. Casteels, M. K. Oberthaler, S. Knoop, E. Timmermans, and J. T. Devreese. Feynman path-integral treatment of the bec-impurity polaron. Phys. Rev. B, 80:184504, 2009.

[8] A. G. Volosniev, H.-W. Hammer, and N. T. Zinner. Real-time dynamics of an impurity in an ideal bose gas in a trap. Phys. Rev. A, 92:023623, 2015.

[9] S. P. Rath and R. Schmidt. Field-theoretical study of the bose polaron. Phys. Rev. A, 88:053632, 2013.

[10] W. Li and S. Das Sarma. Variational study of polarons in bec. Phys. Rev. A, 90:013618, 2014.

[11] L. A. Peña Ardila and S. Giorgini. Impurity in a bose-einstein condensate: study of the attractive and repulsive branch using quantum monte-carlo methods. Phys. Rev. A, 92:033612, 2015.

[12] J. Levinsen, M. M. Parish, and G. M. Gruun. Impurity in a bose-einstein condensate and the efimov effect. Phys. Rev. Lett., 115:125302, 2015.

[13] M. Z. Hasan and C. L. Kane. Colloquium: Topological insulators. Rev. Mod. Phys., 82(4):3045–3067, 2010.

[14] H. L. Stormer, D. C. Tsui, and A. C. Gossard. The fractional quantum hall effect. Rev. Mod. Phys., 71(2):S298–S305, 1999.

[15] A. L. Fetter. Rotating trapped bose-einstein condensates. Rev. Mod. Phys., 81(2):647–691, 2009.

[16] A. Marte, T. Volz, J. Schuster, S. Dürr, G. Rempe, E. G. M. van Kempen, and B. J. Verhaar. Feshbach resonances in rubidium 87: precision measurement and analysis. Phys. Rev. Lett., 89(28):283202, 2002.

[17] F. Dalfovo, S. Giorgini, L. P. Pitaevskii, and S. Stringari. Theory of bose-einstein condensation in trapped gases. Rev. Mod. Phys., 71(3):463–512, 1999.

[18] D. Rychtařik. Two-dimensional Bose-Einstein condensate in an optical surface trap. PhD thesis, Universität Innsbruck, 2004.

[19] Brian DeMarco. Quantum behavior of an atomic Fermi gas. PhD thesis, University of Colorado at Boulder, 2001.

[20] Tyler D. Cumby, Ruth A. Shewmon, Ming-Guang Hu, John D. Perreault, and Deborah S. Jin. Feshbach-molecule formation in a Bose–Fermi mixture. Phys. Rev. A, 87:012703, Jan 2013.

[21] R. S. Bloom, M.-G. Hu, T. D. Cumby, and D. S. Jin. Tests of universal three-body physics in an ultracold bose–fermi mixture. Phys. Rev. Lett., 111:1, 2013.

[22] T. D. Cumby. Exploring few-body scattering resonances in a Bose-Fermi mixture: from Feshbach dimers to Efimov trimers. PhD thesis, University of Colorado at Boulder, 2012.

[23] Ruth Bloom. Few-body collisions in a quantum gas mixture of ^{40}K and ^{87}Rb atoms. PhD thesis, University of Colorado at Boulder, 2014.

[24] C. Chin, R. Grimm, P. Julienne, and E. Tiesinga. Feshbach resonances in ultracold gases. Rev. Mod. Phys., 82(2):1225–1286, 2010.

[25] I. Bloch, J. Dalibard, and W. Zwerger. Many-body physics with ultracold gases. Rev. Mod. Phys., 80(3):885–964, 2008.

[26] Cindy Regal. Experimental realization of BCS-BEC crossover physics with a Fermi gas of atoms. PhD thesis, University of Colorado, Boulder, 2006.

[27] A. Schirotzek, C.-H. Wu, A. Sommer, and M. W. Zwierlein. Observation of fermi polarons in a tunable fermi liquid of ultracold atoms. Phys. Rev. Lett., 102:230402, 2009.

[28] N. Navon, S. Nascimbène, F. Chevy, and C. Salomon. The equation of state of low-temperature fermi gas with tunable interactions. Science, 328:729–732, 2010.

[29] C. Kohstall, M. Zaccanti, M. Trenkwalder Jag, P. A., Massignan, G. M. Bruun, F. Schreck, and R. Grimm. Metastability and coherence of repulsive polarons in a strongly interacting fermi mixture. Nature, 485:615–618, 2012.

[30] M. Koschorreck, D. Pertot, E. Vogt, B. Fröhlich, M. Feld, and M. Köhl. Attractive and repulsive fermi polarons in two dimensions. Nature, 485:619–622, 2012.

[31] Y. Zhang, W. Ong, I. Arakelyan, and J. E. Thomas. Polaron-to-polaron transitions in the radio-frequency spectrum of a quasi-two-dimensional fermi gas. Phys. Rev. Lett., 108:235302, 2012.

[32] C. Klempt, T. Henninger, O. Topic, M. Scherer, L. Kattner, E. Tiemann, W. Ertmer, and J. J. Arlt. Radio-frequency association of heteronuclear Feshbach molecules. Phys. Rev. A, 78:061602, Dec 2008.

[33] L. Mudarikwa, K. Pahwa, and J. Goldwin. Sub-doppler modulation spectroscopy of potassium for laser stabilization. J. Phys. B: At. Mol. Opt. Phys., 45:065002, 2012.

[34] G. C. Bjorkland. Frequency-modulation spectroscopy: a new method for measuring weak absorptions and dispersions. Opt. Lett., 1980.

[35] J. L. Hall, L. Hollberg, T. Baer, and H. G. Robinson. Optical heterodyne saturation spectroscopy. Appl. Phys. Lett., 39:680–682, 1981.

[36] D. A. Steck. Rubidium 87 D Line Data. Oregon Center for Optics and Department of Physics, University of Oregon, 2009.

[37] T. G. Tiecke. Properties of Potassium. van der Waals-Zeeman institute, University of Amsterdam, The Netherlands, 2010.

[38] K. B. MacAdam, A. Steinbach, and C. E. Wieman. A narrow-bandtu nabled iode lasers ystemw ith gratingf eedback, and a saturated absorption spectrometer for cs and rb. Am. J. Phys., 60:1098–1111, 1992.

[39] D. J. McCarron, K. A. King, and S. L. Cornish. Modulation transfer spectroscopy in atomic rubidium. Meas. Sci. Technol., 19:105601, 2008.

[40] R. K. Raj, D. Bloch, J. J. Snyder, G. Camy, and M. Ducloy. High-frequency opoptical heterodyned saturtion spectroscopy via resonant degenerate four-wave mixing. Phys. Rev. Lett., 44(19):1251–1254, 1980.

[41] M. Ducloy and D. Bloch. Theory of degenerate four-wave mixing in resonant doppler-broadened media. ii. doppler-free heterodyne spectroscopy via collinear four-wave mixing in two- and three-level systems. J. Phys., 43:57–65, 1982.

[42] J. M. Goldwin. Quantum degeneracy and interactions in the ^{87}Rb-^{40}K Bose-Fermi mixture. PhD thesis, University of Colorado, Boulder, 2005.

[43] L. D. Landau and S. I. Pekar. Zh. Eksp. Teor. Fiz., 16:341, 1946.

[44] L. D. Landau and S. I. Pekar. Effective mass of a polaron. Zh. Eksp. Teor. Fiz., 18:419, 1948.

[45] H. Fröhlich. Electrons in lattice field. Advances In Physics, 3:325, 1954.

[46] R. P. Feynman. Slow electrons in a polar crystal. Phys. Rev., 97:660, 1955.

[47] M. Bruderer, A. Klein, S. R. Clark, and D. Jaksch. Polaron physics in optical lattice. Phys. Rev. A, 76:011605(R), 2007.

[48] F. Grusdt, Y. E. Shchadilova, A. N. Rubtsov, and E. Demler. Renormalization group approach to the fröhlich polaron model: application to impurity-bec problem. Sci. Rep., 5:12124, 2015.

[49] B. DeMarco and D. S. Jin. Onset of fermi degeneracy in a trapped atomic gas. Science, 285:1703–1706, 1999.

[50] E. G. M. van Kempen, S. J. J. M. F. Kokkelmans, D. J. Heinzen, and B. J. Verhaar. Interisotope determination of ultracold rubidium interactions from three high-precision experiments. Phys. Rev. Lett., 88:093201, 2002.

[51] J. J. Zirbel, K.-K. Ni, S. Ospelkaus, J. P. D. D'Incao, C. E. Wieman, J. Ye, and D. S. Jin. Collisional stability of fermionic feshbach molecules. Phys. Rev. Lett., 100:143201, 2008.

[52] J. P. D'Incao and B. D. Esry. Scattering length scaling laws for ultracold three-body collisions. Phys. Rev. Lett., 94:213201, 2005.

[53] Y. Wang, J. Wang, J. P. D'Incao, and C. H. Greene. Universal three-body parameter in heteronuclear atomic systems. Phys. Rev. Lett., 115:069901, 2015.

[54] R. Roth and H. Feldmeier. Mean-field instability of trapped dilute boson-fermion mixtures. Phys. Rev. A, 65:021603, 2002.

[55] C. Berthod, M. Köhl, and T. Giamarchi. Second-order response theory of radio-frequency spectroscopy for cold atoms. Phys. Rev. A, 92:013626, 2015.

[56] A. Shashi, F. Grusdt, D. A. Abanin, and E. Demler. Radio-frequency spectroscopy of polarons in ultracold bose gases. Phys. Rev. A, 89:053617, 2014.

[57] S. Tan. Large momentum part of a strongly correlated fermi gas. Ann. Phys. (NY), 323:2971, 2008.

[58] S. Tan. Energetics of a strongly correlated fermi gas. Ann. Phys. (NY), 323:2952, 2008.

[59] C. Chin and P. Julienne. Radio-frequency transitions on weakly bound ultracold molecules. Phys. Rev. A, 71:012713, 2005.

[60] L. D. Landau and E. M. Lifshitz. Quantum mechanics (non-relativistic theory) 3nd edn. Pergamon, New York, 1977.

[61] R. B. Laughlin. Anomalous quantum hall effect: an incompressible quantum fluid with fractionally charged excitations. Phys. Rev. Lett., 50:1395, 1983.

[62] T.-L. Ho and C. V. Ciobanu. Rapidly rotating fermi gases. Phys. Rev. Lett., 85:4648, 2005.

[63] X.-G. Wen. Quantum field theory of many-body systems. Oxford University, New York, 2004.

[64] A. H. Castro Neto, F. Guinea, N. M. R. Peres, K. S. Novoselov, and A. K. Geim. The electronic properties of graphene. Rev. Mod. Phys., 81(1):109–162, 2009.

[65] K. von Klitzing. Developments in the quantum hall effect. Phil. Trans. R. Soc. A, 363:2203–2219, 2005.

[66] E. Shopen and Y. Meir. Enhancement of quantum dot peak-spacing fluctuations in the fractional quantum hall regime. Europhys. Lett., 44:766–771, 1998.

[67] Y. Iye. Composite fermions and bosons: An invitation to electron masquerade in quantum hall. Proc. Natl. Acad. Sci., 96:8821–8822, 1999.

[68] N. R. Cooper, N. K. Wilkin, and J. M. F. Gunn. Quantum phases of vortices in rotating bose-einstein condensates. Phys. Rev. Lett., 87:120405, 2001.

[69] N. R. Cooper. Exact ground states of rotatinig bose gases close to a feshbach resonance. Phys. Rev. Lett., 92:220405, 2004.

[70] E. H. Rezayi, N. Read, and N. R. Cooper. Incompressible liquid state of rapidly rotating bosons at filling factor 3/2. Phys. Rev. Lett., 95:160404, 2005.

[71] J. R. Abo-Shaeer, C. Raman, J. M. Vogels, and W. Ketterle. Observation of vortex lattices in bose-einstein condensates. Science, 292:476, 2001.

[72] M. W. Zwierlein, J. R. Abo-Shaeer, A. Schirotzek, C. H. Schunck, and W. Ketterle. Vortices and superfluidity in a strongly interacting fermi gas. Nature, 435:1047, 2005.

[73] V. Bretin, S. Stock, Y. Seurin, and J. Dalibard. Fast rotation of a bose-einstein condensate. Phys. Rev. Lett., 92:050403, 2004.

[74] P. Rosenbusch, D. S. Petrov, S. Sinha, F. Chevy, V. Bretin, Y. Castin, G. Shlyapnikov, and J. Dalibard. Critical rotation of a harmonically trapped bose gas. Phys. Rev. Lett., 88:250403, 2002.

[75] P. C. Haljan, I. Coddington, P. Engels, and E. A. Cornell. Driving bose-einstein-condensate vorticity with a rotating normal cloud. Phys. Rev. Lett., 87:210403, 2001.

[76] V. Schweikhard, I. Coddington, P. Engels, V. P. Mogendorff, and E. A. Cornell. Rapidly rotating bose-einstein condensates in and near the lowest landau level. Phys. Rev. Lett., 92:040404, 2004.

[77] W. S. Bakr, J. I. Gillen, A. Peng, S. Fölling, and M. Greiner. A quantum gas microscope for detecting single atoms in a hubbard-regime optical lattice. Nature, 462:74–77, 2009.

[78] J. F. Sherson, C. Weitenberg, M. Endres, M. Cheneau, I. Bloch, and S. Kuhr. Single-atom-resolved fluorescence imaging of an atomic mott insulator. Nature, 467:68–72, 2010.

[79] M. Miranda, R. Inoue, Y. Okuyama, A. Nakamoto, and M. Kozuma. Site-resolved imaging of ytterbium atoms in a two-dimensional optical lattice. Phys. Rev. A, 91:063414, 2015.

[80] L. W. Cheuk, M. A. Nichols, M. Okan, T. Gersdorf, and V. V. Ramasesh. Quantum-gas microscope for fermionic atoms. Phys. Rev. Lett., 114:193001, 2015.

[81] E. Haller, J. Hudson, A. Kelly, D. A. Cotta, B. Peautecerf, G. D. Bruce, and S. Kuhr. Single-atom imaging of fermions in a quantum-gas microscope. Nat. Phys., 11:738–742, 2015.

[82] M. F. Parsons, F. Huber, A. Mazurenko, C. S. Chiu, W. Setiawan, K. Wooley-Brown, S. Blatt, and M. Greiner. Site-resolved imaging of fermionic ^{6}li in an optical lattice. Phys. Rev. Lett., 114:213002, 2015.

[83] R. Yamamoto, J. Kobayashi, T. Kuno, K. Kato, and Y. Takahashi. An ytterbiumm quantum gas microscope with narrow-line laser cooling. arXiv: 1509.03233, 2015.

[84] N. Gemelke, E. Sarajlic, and S. Chu. Rotating few-body atomic systems in the fractional quantum hall regime. arxiv: 1007.2677, 2010.

[85] Y.-J. Lin, R. L. Compton, K. Jiménez-García, J. V. Porto, and I. B. Spielman. Synthetic magnetic fields for ultracold neutral atoms. Nature, 462:628–632, 2009.

[86] B. K. Stuhl, H.-I. Lu, L. M. Aycock, D. Genkina, and I. B. Spielman. Visualizing edge states with an atomic bose gas in the quantum hall regime. Science, 349:1514–1518, 2015.

[87] M. Mancini, G. Pagano, G. Cappellini, L. Livi, M. Rider, J. Catani, C. Sias, P. Zoller, M. Inguscio, M. Dalmonte, and L. Fallani. Observation of chiral edge states with neutral fermions in synthetic hall ribbons. Science, 349:1510–1513, 2015.

[88] M. Aidelsburger, M. Atala, M. Lohse, J. T. Barreiro, B. Paredes, and I. Bloch. Realization of the hofstadter hamiltonian with ultracold atoms in optical lattices. Phys. Rev. Lett., 111:185301, 2013.

[89] H. Miyake, G. A. Siviloglou, C. J. Kennedy, W. C. Burton, and W. Ketterle. Realizing the harper hamiltonian with laser-assisted tunneling in optical lattices. Phys. Rev. Lett., 111:185302, 2013.

[90] B. E. A. Saleh and M. C. Teich. Fundamentals of photonics (2nd edn). John Wiley&Sons, New Jersy, 2007.

[91] Michael R. Matthews. Two-component Bose-Einstein condensation. PhD thesis, University of Colorado, Boulder, 1999.

[92] P. C. Haljan. Vortices in a Bose-Einstein condensate. PhD thesis, University of Colorado, Boulder, 2003.

[93] I. R. Coddington. Vortices in a highly rotating Bose condensate gas. PhD thesis, University of Colorado at Boulder, 2004.

[94] L. D. Landau and E. M. Lifshitz. Mechanics 3nd edn. Pergamon, New York, 1976.

[95] H. Wu and C. J. Foot. Direct simulation of evaporative cooling. J. Phys. B: At. Mol. Opt. Phys., 29:L321, 1996.

[96] J. Goldwin, S. Inouye, M. L. Olsen, and D. S. Jin. Cross-dimensional relaxation in bose-fermi mixtures. Phys. Rev. A, 71:043408, 2005.

[97] P. Engels, I. Coddington, P. C. Haljan, and E. A. Cornell. Nonequilibrium effects of anisotropic compression applied to vortex lattices in bose-einstein condensates. Phys. Rev. Lett., 89:100403, 2002.

[98] Y. Castin and R. Dum. Bose-einstein condensates in time dependent traps. Phys. Rev. Lett., 77:5315, 1996.

[99] V. M. Pérez-García, H. Michinel, J. I. Cirac, M. Lewenstein, and P. Zoller. Dynamics of bose-einstein condensates: Variational solutions of the gross-pitaevskii equations. Phys. Rev. A, 56:1424, 1997.

Appendix A

RF spectroscopy of non-interacting atoms

A RF photon has frequency ν_0 typically around 80 MHz and has a negligible momentum. The RF spectroscopy therefore induces momentum-conserving transitions. Let H_0 be the noninteracting Hamiltonian of K atoms and $H_{rf}(t)$ be the time-dependent interaction between RF radiation and K atoms. we have

$$\begin{aligned} H &= H_0 + H_{rf}, \\ H_0 &= \sum_{\mathbf{p}} \left[\epsilon_f(\mathbf{p}) f^\dagger_{1,\mathbf{p}} f_{1,\mathbf{p}} + (\epsilon_f(\mathbf{p}) + h\nu_0) f^\dagger_{0,\mathbf{p}} f_{0,\mathbf{p}} \right], \\ H_{rf}(t) &= \hbar \mathcal{E}(t) \sum_{\mathbf{k}} (f^\dagger_{1,\mathbf{k}} f_{0,\mathbf{k}} + H.c.), \end{aligned} \tag{A.1}$$

where $f_{\sigma,\mathbf{p}}$ (or $f^\dagger_{\sigma,\mathbf{p}}$) is the annihilation (or creation) operator of an impurity fermion in the hyperfine state σ with a momentum $\mathbf{p}$. For a gaussian RF pulse during $t \in [0, 4\Delta t]$, it is described by $\mathcal{E}(t) = \left(\frac{dE_0}{2}\right) \exp(-(t-2\Delta t)^2/\Delta t^2)(e^{-i2\pi\nu_0 t} + e^{i2\pi\nu_0 t})$, which corresponds to an electric field $E(t) = E_0 \exp(-(t-2\Delta t)^2/\Delta t^2)\cos(2\pi\nu_0 t)$. Here d is the induced electrical dipole moment of atoms. The fast-time-averaged RF power is $\bar{P}(t) = \frac{\epsilon_0 c}{2} E_0^2 \exp(-2(t-2\Delta t)^2/\Delta t^2)$.

Let the initial state $|I\rangle = |0, \mathbf{k} = 0\rangle$ and final state $|F\rangle = |1, \mathbf{k}\rangle$. The time-dependent Schrödinger equation for the RF spectroscopy is

$$i\hbar \partial_t |\psi_{\mathbf{k}=0}(t)\rangle = [H_0 + H_{rf}(t)] |\psi_{\mathbf{k}=0}(t)\rangle.$$

To solve the above equation, I write a single-body wavefunction with zero momentum as

$$|\psi_{\mathbf{k}=0}(t)\rangle = C_0(t) e^{-i(\epsilon_f(0)+h\nu_0)t/\hbar} |0, \mathbf{k}=0\rangle + C_1(t) e^{-i\epsilon_f(0)t/\hbar} |1, \mathbf{k}=0\rangle$$

with the initial condition of $C_0(0) = 1$ and $C_1(0) = 0$. Solving the above differential equation, we have $C_1(t) = -i \sin[\Omega_0 \Delta t(1 + \text{ Erf}((t - 2\Delta t)/\Delta t))]$. During the above derivation, the rotating wave approximation has been used. Here the Rabi frequency $\Omega_0 = dE_0$. For our RF spectroscopy, the gaussian pulse duration $4\Delta t$ is the same as t, which means $C_1(t) = -i \sin(\Omega_0 t/2)$. The fractional population of the spin-flipped atoms in the final state $|F(\mathbf{k})\rangle$ is thus

$$P_F = |\langle F(\mathbf{k})|\psi_{\mathbf{k}=0}(t)\rangle|^2 = \delta(\mathbf{k}) \sin^2\left(\frac{\Omega_0}{2}t\right), \tag{A.2}$$

which gives the Rabi oscillation with the oscillation frequency Ω_0. Here $\delta(\mathbf{k})$ is the Dirac delta function.

In the Schrödinger picture, Eq. (A.1) can be written into a time-independent form

$$\hat{\mathcal{H}}_{rf}(\Omega_0) = \hbar\frac{\Omega_0}{2}\sum_{\mathbf{k}}(f^\dagger_{1,\mathbf{k}} f_{0,\mathbf{k}} + H.c.), \tag{A.3}$$

with the corresponding time-dependent wavefunction at the momentum $\mathbf{k}$ being

$$|\psi_{\mathbf{k}}(t)\rangle = C_0(t)|0,\mathbf{k}\rangle + C_1(t)|1,\mathbf{k}\rangle.$$

The Schrödinger equation is thus, $i\hbar\partial_t|\psi_{\mathbf{k}}(t)\rangle = \hat{\mathcal{H}}_{rf}(\Omega_0)\psi_{\mathbf{k}}(t)\rangle$, which gives the solution of $C_1(t) = -i \sin(\Omega_0 t/2)$. The Radi frequency has a relation

$$\Omega_0^2 = \frac{4}{\hbar^2}\left|\langle 1,\mathbf{k}|\hat{\mathcal{H}}_{rf}(\Omega_0)|0,\mathbf{k}\rangle\right|^2, \tag{A.4}$$

which is useful when discussing the residue of a quasiparticle (see Sec. 3.4).

To get a lineshape for the gaussian pulse in the frequency domain, we need to do the Fourier transformation of $\mathcal{E}(t)$, which has

$$\tilde{\mathcal{E}}(2\pi\nu) = \int_{-\infty}^{\infty} dt\ e^{i2\pi\nu t}\mathcal{E}(t) = 2\hbar\Delta t\Omega_0 e^{i4\nu/\delta\nu}e^{-(\nu-\nu_0)^2/\delta\nu^2}, \tag{A.5}$$

with $1/e$ width $\delta\nu = 1/(\pi\Delta t)$. Therefore, the lineshape is $\mathcal{R}(\nu - \nu_0) \propto |\tilde{\mathcal{E}}(2\pi\nu)|^2 \propto \exp[-2(\nu - \nu_0)^2/\delta\nu^2]$. After the RF pulse, the number of spin flipped K atoms in $|1\rangle$ state at the central regime ($\rho < \rho_0$) can be modeled by

$$N_{K,1}(\nu, \rho \le \rho_0) = A\int_0^{\rho_0} \rho d\rho \int_{-\infty}^{\infty} dz\ n_{K,0}(\rho, z)\mathcal{R}(\nu - \nu_0) = N_{K,0}(\nu, \rho \le \rho_0)\mathcal{R}(\nu - \nu_0), \tag{A.6}$$

where A is a constant and $n_{K,0}(\rho, z)$ is the density distribution of the K atoms in $|0\rangle$ state.

Appendix B

Time-averaged trapping potentials

An uniform trap I choose the functional form of $\rho_c(t_s) = \rho_c^{\max}\sqrt{\mathrm{mod}(t_s,\mathcal{T})/\mathcal{T}}$ with $\mathcal{T}$ being the period. Let's consider the range of $t_s \in [0,\mathcal{T}]$. we have $\rho_c(t_s) = \rho_c^{\max}\sqrt{t_s/\mathcal{T}}$ and $t_s = \mathcal{T}\cdot[\rho_c(t_s)/\rho_c^{\max}]^2$. The Eq. (5.2) is thus

$$\begin{aligned}
U_{\mathrm{paint}}(\rho) &= \frac{U_0}{\mathcal{T}}e^{-2\rho^2/w_0^2}\int_0^{\mathcal{T}} dt_s e^{-2\rho_c^2(t_s)/w_0^2} J_0\left(i\frac{4\rho\cdot\rho_c(t_s)}{w_0^2}\right) \\
&= \frac{U_0}{\mathcal{T}}e^{-2\rho^2/w_0^2}\frac{2\mathcal{T}}{(\rho_c^{\max})^2}\int_0^{\rho_c^{\max}} \rho_c d\rho_c e^{-2\rho_c^2/w_0^2} J_0\left(i\frac{4\rho\cdot\rho_c}{w_0^2}\right) \\
&= \frac{U_0}{\mathcal{T}}e^{-2\rho^2/w_0^2}\frac{2\mathcal{T}}{(\rho_c^{\max})^2}\sum_{k=0}^{\infty}\int_0^{\rho_c^{\max}} d\rho_c e^{-2\rho_c^2/w_0^2}\rho_c^{2k+1}\left(\frac{2\rho}{w_0^2}\right)^{2k}/(k!)^2 \\
&= \frac{U_0}{\mathcal{T}}e^{-2\rho^2/w_0^2}\frac{2\mathcal{T}}{(\rho_c^{\max})^2}\sum_{k=0}^{\infty}\left(\frac{2\rho}{w_0^2}\right)^{2k}/(k!)^2\int_0^{\infty} d\rho_c e^{-2\rho_c^2/w_0^2}\rho_c^{2k+1} \\
&= \frac{U_0}{\mathcal{T}}e^{-2\rho^2/w_0^2}\frac{2\mathcal{T}}{(\rho_c^{\max})^2}\sum_{k=0}^{\infty}\left(\frac{2\rho}{w_0^2}\right)^{2k}(w_0^2/2)^{k+1}/2/k! \\
&= \frac{U_0}{\mathcal{T}}e^{-2\rho^2/w_0^2}\frac{2\mathcal{T}}{(\rho_c^{\max})^2}\sum_{k=0}^{\infty}\left(\frac{2\rho^2}{w_0^2}\right)^{k}(w_0^2/4)/k! \\
&= \frac{1}{2}U_0\left(\frac{w_0}{\rho_c^{\max}}\right)^2
\end{aligned}$$

during which I have used the formula $J_0(x) = \sum_{k=0}^{\infty}(-1)^k(x^2/4)^k/(k!)^2$ and $\int_0^{\infty} x^{2k+1}e^{-x^2/a^2}dx = \frac{k!}{2}a^{2k+2}$. The approximation of $\int_0^{\rho_c^{\max}} d\rho_c e^{-2\rho_c^2/w_0^2}\left\{\rho_c^{2k+1}\left(\frac{2\rho}{w_0^2}\right)^{2k}/(k!)^2\right\} \to \int_0^{\infty} d\rho_c e^{-2\rho_c^2/w_0^2}\{\cdots\}$ holds to be true when $\rho_c^{\max} \geq 3w_0$ (verified by a numerical calculation).

A harmonic trap I choose a more complex functional form of

$$\rho_c(t_s) = \rho_c^{\max}\cdot\sqrt{\frac{b+1-\sqrt{(b+1)^2-4b\cdot\mathrm{mod}(t_s,\mathcal{T})/\mathcal{T}}}{2b}},$$

with the unitless parameter $0 \leq b \leq 1$. This function satisfies $\rho_c(t_s = 0) = 0$ and $\rho_c(t_s = \mathcal{T}) = \rho_c^{\max}$. The above equation is equivalent to

$$t_s = \mathcal{T} \cdot \left[(b+1) \cdot \left(\frac{\rho_c}{\rho_c^{\max}} \right)^2 - b \cdot \left(\frac{\rho_c}{\rho_c^{\max}} \right)^4 \right].$$

For the convenience of discussions, let me rewrite the above equation as $t_s = A\rho_c^2 - B\rho_c^4$ with $A = \mathcal{T} \cdot (b+1)/(\rho_c^{\max})^2$ and $B = \mathcal{T} \cdot b/(\rho_c^{\max})^4$. The Eq. (5.2) is thus

$$\begin{aligned}
& U_{\text{paint}}(\rho) \\
= \; & \frac{U_0}{\mathcal{T}} e^{-2\rho^2/w_0^2} \int_0^{\mathcal{T}} dt_s e^{-2\rho_c^2(t_s)/w_0^2} J_0\left(i \frac{4\rho \cdot \rho_c(t_s)}{w_0^2} \right) \\
= \; & \frac{U_0}{\mathcal{T}} e^{-2\rho^2/w_0^2} \left[2A \int_0^{\rho_c^{\max}} \rho_c d\rho_c e^{-2\rho_c^2/w_0^2} J_0\left(i \frac{4\rho \cdot \rho_c}{w_0^2} \right) - 4B \int_0^{\rho_c^{\max}} \rho_c^3 d\rho_c e^{-2\rho_c^2/w_0^2} J_0\left(i \frac{4\rho \cdot \rho_c}{w_0^2} \right) \right] \\
= \; & \frac{U_0}{\mathcal{T}} e^{-2\rho^2/w_0^2} \sum_{k=0}^{\infty} \left(2A \int_0^{\rho_c^{\max}} d\rho_c e^{-2\rho_c^2/w_0^2} \rho_c^{2k+1} - 4B \int_0^{\rho_c^{\max}} d\rho_c e^{-2\rho_c^2/w_0^2} \rho_c^{2k+3} \right) \left(\frac{2\rho}{w_0^2} \right)^{2k} /(k!)^2 \\
= \; & \frac{U_0}{\mathcal{T}} e^{-2\rho^2/w_0^2} \sum_{k=0}^{\infty} \left(2A \int_0^{\infty} d\rho_c e^{-2\rho_c^2/w_0^2} \rho_c^{2k+1} - 4B \int_0^{\infty} d\rho_c e^{-2\rho_c^2/w_0^2} \rho_c^{2k+3} \right) \left(\frac{2\rho}{w_0^2} \right)^{2k} /(k!)^2 \\
= \; & \frac{U_0}{\mathcal{T}} e^{-2\rho^2/w_0^2} \sum_{k=0}^{\infty} \left[2A \left(\frac{w_0^2}{2} \right)^{k+1} \frac{k!}{2} - 4B \left(\frac{w_0^2}{2} \right)^{k+2} \frac{(k+1)!}{2} \right] \left(\frac{2\rho}{w_0^2} \right)^{2k} /(k!)^2 \\
= \; & \frac{U_0}{\mathcal{T}} \frac{w_0^2}{2} (A - Bw_0^2 - 2B\rho^2)
\end{aligned}$$

during which I have used the formula $J_0(x) = \sum_{k=0}^{\infty} (-1)^k (x^2/4)^k/(k!)^2$ and $\int_0^{\infty} x^{2k+1} e^{-x^2/a^2} dx = \frac{k!}{2} a^{2k+2}$. The approximation of $\int_0^{\rho_c^{\max}} d\rho_c e^{-2\rho_c^2/w_0^2} \left\{ \rho_c^{2k+1} \left(\frac{2\rho}{w_0^2} \right)^{2k} /(k!)^2 \right\} \rightarrow \int_0^{\infty} d\rho_c e^{-2\rho_c^2/w_0^2} \{ \cdots \}$ holds to be true when $\rho_c^{\max} \geq 3w_0$ (verified by a numerical calculation).